UNIVERSITÀ
DEGLI STUDI
DI PADOVA

Head Office: Università degli Studi di Padova

Department of Physics and Astronomy “Galileo Galilei”

Ph.D. COURSE IN: Physics
SERIES: 30°

Beam Dynamics Characterization of the IFMIF/EVEDA RFQ Input Beam

Thesis written with the financial contribution of INFN (Istituto Nazionale di Fisica Nucleare)

Coordinator: Prof. Gianguido Dall’Agata
Supervisor: Dott. Andrea Pisent

Ph.D. student : Luca Bellan

Beam Dynamics Characterization of the IFMIF/EVEDA RFQ Input Beam

Luca Bellan

Supervisor: Dr. A. Pisent

Department of Physics and Astronomy
University of Padova

December 2017

Acknowledgements

I would like to express my special appreciation to Michele Comunian for supporting me in this thesis work, for his priceless lessons and for the hard commissioning time spent in Rokkasho. Thank you so much.

My greatest appreciation also goes to Enrico Fagotti, for his countless support and brilliant suggestions. I would further like to thank Marco Cavenago: he was always available for discussions and suggestions.

I owe my deepest gratitude to my neighbors, Antonio Palmieri and Francesco Grespan for their precious comments and fruitful discussions.

Furthermore, I would like to thank Nicolas Chauvin, Benoit Bolzon for the useful discussions and commissioning time spent Rokkasho and to Frédéric Gérardin, for the fruitful comparison of the results and important help with the WARP code.

A special thanks goes to my family. Words cannot express how grateful I am for their continuous support.

Last but not least, I would like to gratefully acknowledge the support of the INFN-LNL team, the LIPAc team and members for their effort in setting up the world-leading IFMIF/EVEDA facility.

Abstract

The high intensity accelerators are one of the world-wide leading edge research in the beam dynamics studies. The upgrades of the existing accelerator LINAC4, FERMILAB, FAIR and the new applications on the neutron technologies such as ESS, IFMIF, MUNES, both for science research, medical treatment and material testing require an increase knowledge in the high intensity beams treatment. One of the most difficult part to be treated and which represent the first obstacle in increasing the beam intensity in the accelerators, is the injector part: the large number of charge particles at low energy forms a strongly interacting system, subjected to the Coulombian interaction. The situation further complicates due to the presence of different species which produces a plasma-like behavior of the beam. On the behalf of the INFN-LNL team, I participated to the commissioning of the high intensity injector (source and low energy transfer line) of the IFMIF/EVEDA project. Via experiments and simulation model developments I contributed to the study of the beam behavior in this specific framework. In particular I upgrade the emittance measurement routine in order to manage correctly the artifacts; I develop and benchmark with measurements self-consistent simulation models of the LEBT and extraction transfer line, which includes the secondary electron from residual gas and from metal due to collisions; I design a modification of medium and high energy line in order to test the CW steady state of the longest radio frequency quadrupole in the world, an in-kind contribution of INFN. All the development routines and experience will give important contributions for the next high intensity facilities. The first chapter presents the motivation of the IFMIF project and the main characteristics required by the accelerator. The main challenges of such accelerator are also listed. The second chapter introduces the main concepts of the beam dynamics of space-charge which will be used in the thesis. The third chapter presents the IFMIF/EVEDA project, with a description of the main elements; particular focus is made onto the source, the low energy beam transfer line and on the radio frequency quadrupole. Scaling law derivation for the extracted beam with contaminants is shown. The commissioning phases are introduced, each with its specific challenges. The fourth chapter presents the modification of the emittance analysis routine which can manage the ghost infested signal of the IFMIF/EVEDA emittancemeter. The fifth and the sixth chapters contains the simulation models developed to estimate the space-charge

beam behavior under neutralization regime: the model with constant neutralization and the one with the full secondary plasma evolution are presented and benchmarked with the measurements. In the fifth chapter the measurements refers to $60-55$ mA proton beam at 50 keV, while for the sixth chapter the beam considered is composed of $140-135$ mA deuteron beam at 100 keV. In these chapters, the variation of the radio frequency quadrupole beam input characteristics with respect to the electromagnetic plasma confinement of the low energy transfer line is studied. The original contribution in these simulations is given by the emitted secondary electron from metal, which as some effects on the space charge compensation process, on the emittance value. Deep study of the multispecies distributions and behavior was performed. The four chapter defines, for the experimental proton point considered, the solenoid variations where searching the maximum radio frequency quadrupole transmission. The output beam behavior of this one is studied in commissioning perspective. In the sixth chapter, after testing the radio frequency quadrupole transmission with the secondary plasma model (also said dynamic neutralization model) with a realistic beam distribution, the simulations of the extraction system are presented. The benchmark with the measurements are also performed. The seventh chapter presents the design of the modification of the medium and high energy transfer sections of the accelerator in order to allow the test of the CW of the radio frequency quadrupole, bypassing the superconductive cavities. Extensive simulations of the system robustness to the errors are explored. The last chapter reports the conclusions.

Table of contents

List of figures

List of tables

Nomenclature

Acronyms / Abbreviations

BS	Beam Stop
D.C.	Duty Cycle
ECR	Electron Cyclotrone Resonance
EMU	Emittancemeter Measurement Unit
FC	Faraday Cup
HEBT	High Energy Beam Trasnfer
HPBD	High Power Beam Dump
HWR	Half Wave Resonator
IFMIF	International Fusion Material Irradiation Facility
LEBT	Low Energy Beam Transfer
LIPAc	Linear IFMIF Prototype Accelerator
LPBD	Low Power Beam Dump
MEBT	Medium Energy Beam Transfer
RFQ	Radio Frequency Quadrupole
s.c.c.	space charge compensation
SRF	Superconducting Radio Frequency

Chapter 1

Introduction

1.1 Neutron spectra from the future fusion reactors

The fusion technology is one of the main challenges of the modern era, with the aim to produce large density and carbon free power sources.

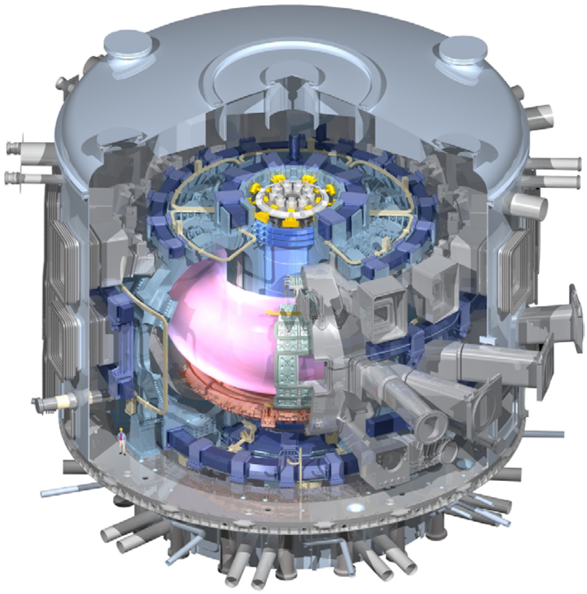

Fig. 1.1 Sketch ITER tokamak fusion reactor. The pink is a representative picture of the plasma confined into a magnetic confinement field. [1]

The idea is to reproduce the nuclear fusion mechanism of the stars: the confinement needed in the stars is given by the gravity force which opposes to the reaction pressure. In that way, it is possible to create an equilibrium between the two forces. However, this kind of confinement would require a large mass (comparable to the Sun) in order to overcome the Coulomb barrier and to keep the fuel/reaction confined.

There are several way to overcome this problem. One of them consists in the usage of the magnetic force in order to supply the confinement. Examples of this solution are the facility of DEMO [1] and ITER [1], which will use a tokamak type reactor. The tokamak can be described as a toroidal metallic vessel in which the plasma is confined via a magnetic systems, as it can be seen in Fig. 1.1. The reaction which will be used in order to supply power is the deuterium-tritium fusion, described by Eq. 1.1:

$${}^2_1\mathrm{H} + {}^3_1\mathrm{H} \rightarrow {}^4_2\mathrm{He} + {}^1_0\mathrm{n} \tag{1.1}$$

The 14.1 MeV generated by the reaction are given to the neutrons while 3.5 MeV to the ${}^4_2$He. The neutron spectra is shown in Fig. 1.2: there is a large neutron flux with energy above 12 MeV compared to a fission reactors.

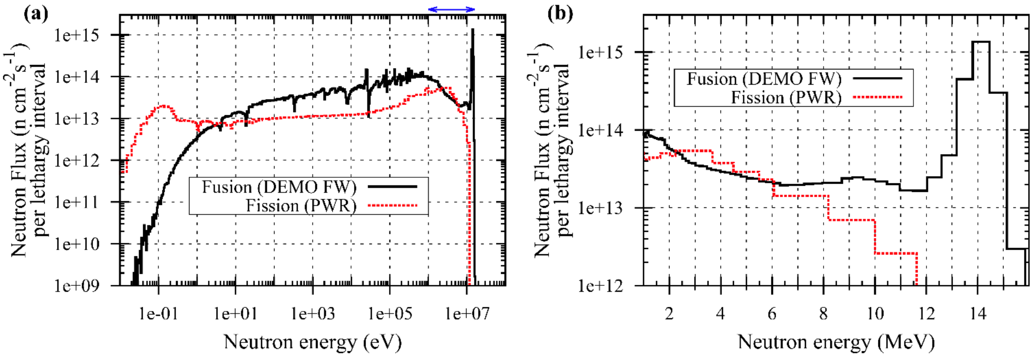

Fig. 1.2 Comparison between the neutron-energy spectra in fission and fusion reactor (DEMO is taken as example). In (a), the full energy spectra is shown, while in (b) the range above 1 MeV is shown. It is possible to notice the significant amount of neutron flux above 12 MeV respect to the fission reactor, with a wide peak around E=14 MeV, in agreement with reaction described in 1.1 [2]

The neutrons escape the plasma confinement and are absorbed by the wall of vessel. The intensity of the expected neutron flux is about 100 times the current fission power reactors, being at the same time the main carriers of the energy produced by the reaction and the main source of the material degradation.

At working regime of a future fusion plant, the amount of displacements per atom foreseen will be 15 dpa/y (displacement per atom/ year)[3]. Such large radiation field poses serious challenges for the maintenance of the compounds which composes the reactor core. Therefore, similar irradiation source is required in order to test the reactor materials under this large irradiation flux.

1.2 Accelerator solution

1.2.1 Required characteristics

In order to test the material of the future fusion reaction it is important to reproduce a similar neutron spectra: the material microstructure degradation is related to the energy and to the flux of the colliding neutrons.
Therefore, two main characteristics need to be fulfilled by the candidate neutron source:

1. It shall have a neutron spectra peaked at 14.1 MeV
2. It shall produce a similar neutron flux, of the order of $J_{\mathrm{n}} = 10^{18}\ \mathrm{m}^{-2}\ \mathrm{s}^{-1}$

The first requirements excludes the fission reactor as candidate; as a matter of fact, their neutron flux depleted rapidly after 12 MeV, as it can be seen in the Fig.1.2.
On the contrary, an accelerator based neutron source can fit the requirements because it is possible to control both the energy of emitted neutrons and their flux. However none of the long existed facilities is compliant with the spectra characteristics. In fact, the existing spallation neutron sources produce a wide range of neutrons (not peaked at 14 MeV) up to order of hundreds of MeV, leading to different damage of the materials. Also the ion implantation facilities are not suited for such purpose, due to a reduced irradiation volume.
Therefore, a specific accelerator needs to be built in order to produce the requested neutron spectra.

1.2.2 The IFMIF project

The International Fusion Materials Irradiation Facility, (IFMIF), is a projected materials test facility in which the candidate materials for a fusion reactor can be fully qualified. The reaction chosen in order to get an equivalent neutron spectra peaked at 14 MeV is based on the deuterium-litium $\mathrm{Li}(\mathrm{d}, X\mathrm{n})$ stripping reaction.
This kind of source shows an energy distribution around a peak flux that can be adapted to 14 MeV: the design value of the projectile is 40 MeV, which ensures a board peak flux between 14-15 MeV, after the beam collides on the Liquid target.
Another characteristic remains to be fulfilled from 1.2.1: the neutron flux intensity. In order to reach equivalent J_{n}, the number of deuteron collisions onto the target should be $1.56\times\ 10^{18}\ \mathrm{s}^{-1}$, which corresponds to 250 mA delivered by the accelerator in continuous. Considering the energy and the current of the beam, the total power delivered on target is 5 MW, which will make this accelerator one of the most powerful in the world. Several consequences derive from this point: such a large current will make critical the Columbian

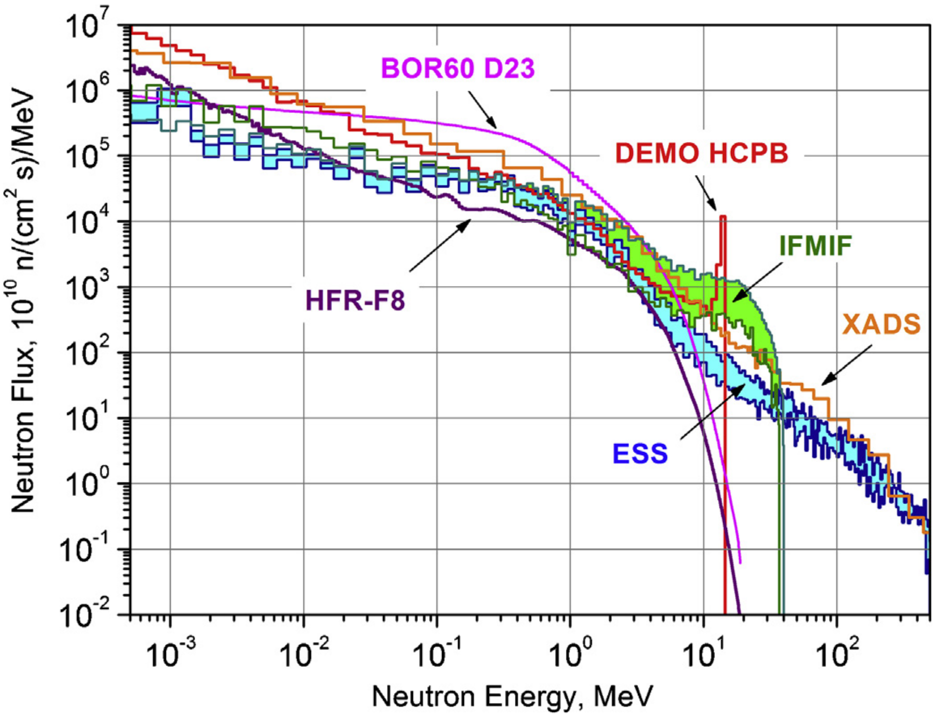

Fig. 1.3 Comparison between the different neutron source accelerator facilities and the DEMO neutron spectra.[4]

effects in the low energy chains of the accelerator as it will be explained later. Moreover, the large density power deposition due to possible beam control failures makes the control of the beam behavior critical inside the accelerator: a correct beam dynamics characterization in all part of the accelerator minimizes such risk.
The IFMIF accelerator will be composed of two twins linac's. This kind of machines proved to be able to manage such high intensity beams [5]. They will send the 2×125 mA D beam at 40 MeV on a liquid screen target as shown in Fig. 1.4. The single linac is composed of several parts, which are categorized by the energy of the beam:

- the ion source: D^+ beam will be produced continuously by the ion source. The deuterons will be emitted at 100 keV.
- the LEBT (Low Energy Beam Transfer): it is the line that connects the ion source with the first stage of acceleration.
- the RFQ (Radio Frequency Quadrupole): it will accelerate and bunch the particles coming from the source. The input beam will be accelerated from 100 keV to 5 MeV.
- the MEBT (Medium Energy Beam Transfer): the output of the RFQ will be managed by this line and sent to the final acceleration step.

- the SRF (Superconducting Radio Frequency) cavities: the last step of acceleration, which will accelerate the beam up to its final energy (i.e. 40 MeV), via HWR (Half Wave Resonators) super conductive cavities.
- the HEBT (High Energy Beam Transfer): the beam at its maximum energy will be sent to the Liquid target, through a magnetic separator (in order to eliminate the residual contaminants). This line will be equipped by magnetic lens which will provide a uniform beam footprint of 200×50 mm^2 on the liquid litium target.

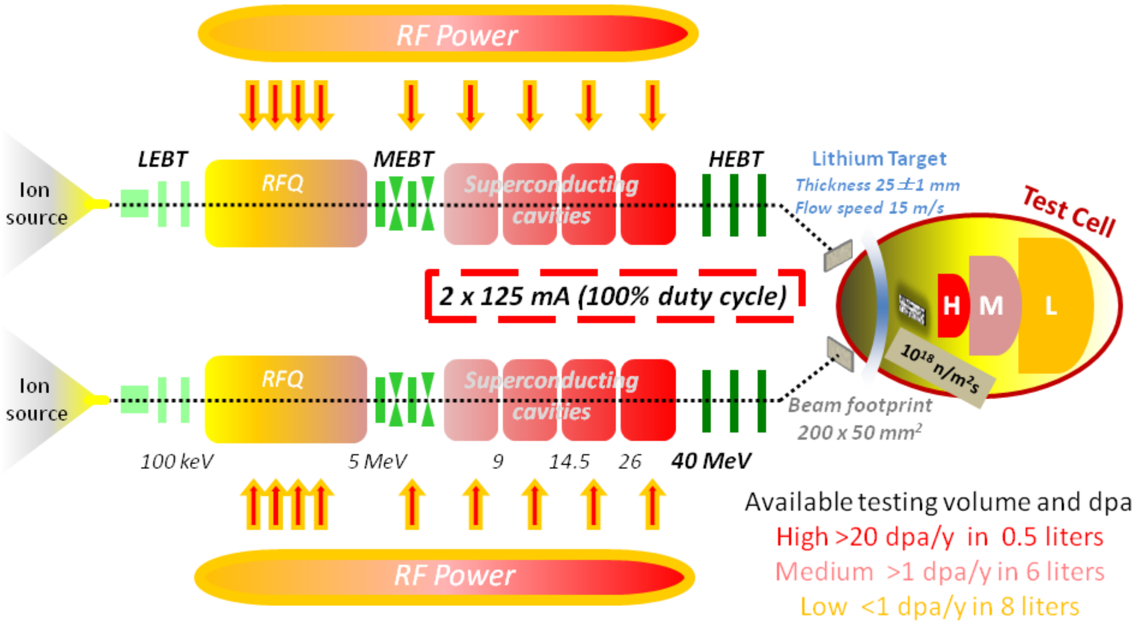

Fig. 1.4 Sketch of the IFMIF facility, which is composed by two twins Linac accelerators described above. The main parts of the machine are shown as well as the machine which will be powered by the RF.

Chapter 2

Beam dynamics models

2.1 Rms quantities and multiparticle beam formalism

2.1.1 Emittance of a beam

The beam occupies a 6D volume in the 6D phase space (x, y, z, p_x, p_y, p_z). If the Liouville theorem applies to the system, the hyper-volume is maintained during the system evolution. If the system is subject to linear forces, the shape is also maintained.

Suppose that the shape of this volume is an hyper-ellipsoid. Projections of this hyper-ellipsoid onto transverse and longitudinal planes (x, p_x), (y, p_y) and (z, p_z) are called phase space projections and design an elliptical area. In transverse and longitudinal planes the obtained ellipse can be described by Courant-Snyder parameters (also called Twiss parameters) via this equation (example shown for x component):

$$\gamma_x x^2 + 2\alpha_x x x' + \beta_x x'^2 = \varepsilon_x \tag{2.1}$$

where α_x, β_x, γ_x are the Twiss/Courant-Snyder parameters and define the orientation and the extent of the ellipse. The emittance ε_x multiply by π is the 2D area of the ellipse in the phase space.

If the motion of single particle is governed by linear forces, the ε_x results an invariant of the motion, called Courant-Snyder invariant. For a defined emittance and considering the longitudinal coordinate s which indicates the position of the beam center along the accelerator, it is possible to calculate the beam "extent" in space (envelope) and divergence at any point s by the following equation.

$$a(s) = \sqrt{\varepsilon_x \beta_x(s)} \qquad a'(s) = \sqrt{\varepsilon_x \left(\frac{1+\alpha^2(s)}{\beta_x(s)}\right)} \tag{2.2}$$

β_x is called betatron function and depends on the focusing strength $K(s)$ of the applied fields. It is possible to show that the single particle dynamics is related to the envelope beam motion via the Courant-Snyder parameters. Considering a lattice with periodic focusing strength $K(s) = K(s+L)$ (L is the spatial period) the single particle of the beam is governed by Hill equation:

$$x'' + K(s)x(s) = 0 \tag{2.3}$$

The solution of the Hills equation represents a particle tracing out in the phase space:

$$x(s) = \sqrt{\varepsilon_x \beta_x(s)} cos(\sigma_0 - \phi) \tag{2.4}$$

where σ_0 is the phase advance. The phase advance is related to number (multiplied by 2π) of the phase space oscillations that a particle makes in L; it is defined as it follows:

$$\sigma_0 = \int_s^{s+L} \frac{ds}{\beta_x(s)} \tag{2.5}$$

Finally, β_x is governed by the below differential equation which depends only on the focusing strength K:

$$\frac{1}{2}\beta_x \beta_x'' - \frac{1}{2}\beta_x^2 + \frac{1}{2}\beta_x^2 K(s) = 1 \tag{2.6}$$

Taking Eq. 2.4 and its derivative, eliminating the phase variable, it is possible to obtain again the Courant-Snyder invariant expressed in Eq. 2.1. Substituting into Eq. 2.6 the first equality of Eq. 2.2 and derivating the a terms, it is possible to obtain the envelope equation:

$$a''(s) + K(s)a(s) - \frac{\varepsilon^2}{a^3(s)} = 0 \tag{2.7}$$

If the beam is cylindrically symmetric, $a = r$

2.1.2 Rms definition of emittance

It is useful to introduce a statistics formalism which can be applied to the experimental data or tracking simulations, in order to extract informations for the beam dynamics treatise considered above. Considering the ensemble of particles, it is possible to associate the spread of the distribution of 2D phase space to a single value, based on the root-mean square formula [6].

$$\varepsilon_{\mathrm{rms,x}} = \sqrt{\langle x^2 \rangle \langle x'^2 \rangle - \langle xx' \rangle^2} \tag{2.8}$$

where the $\langle x \rangle$ indicates the average over the phase space of the quantity x. $\varepsilon_{rms,x}$ is called rms emittance: the related equation is the same as 2.1, but with the subscript rms. In this case, the Twiss rms parameters can be calculated at each point s starting from $\varepsilon_{rms,x}$ and each particle phase space coordinates (x_i, x'_i):

$$\alpha_{rms,x} = -\frac{\langle xx' \rangle}{\varepsilon_{rms,x}}, \qquad \beta_{rms,x} = \frac{\langle x^2 \rangle}{\varepsilon_{rms,x}}, \qquad \gamma_{rms,x} = \frac{\langle x'^2 \rangle}{\varepsilon_{rms,x}}, \tag{2.9}$$

The rms quantities allow to calculate the $x_{rms} = \sqrt{\varepsilon_{rms,x}\beta_{rms,x}(s)}$ and the $x'_{rms}(s)$ in similar manner to Eq. 2.2, but considering the rms quantities. Multiplying the rms emittance by an appropriate factor, it is possible to include more or less particles of the beam population, depending on the choice (see Fig. 2.1).

From now on the subscript *rms* will be dropped from the Twiss parameters in order to simplify the formalism. The $\varepsilon_{rms,x}$ is invariant under the same condition of ε_x: if the self/applied forces are not linear, or for a certain s interval the equation of motion are coupled between planes x, y, z (such as within the solenoid fields) the rms emittance is not conserved. From this thesis work point of view, the rms emittance growth is the main observable in order to detect the effect of the self/applied field non-linearities.

Under the non-linearities, the shape in the phase space moves away from the elliptical contour, developing tales, curvatures, halos. As an example, if a group of particles of the distribution changes the phase advance respect to the central part of the distribution, the ellipsoid starts to stretch out not uniformly. It is straightforward to notice that the rms formulation of the ellipse does not fit anymore to the distribution: forcing to apply this formalism to such deformed

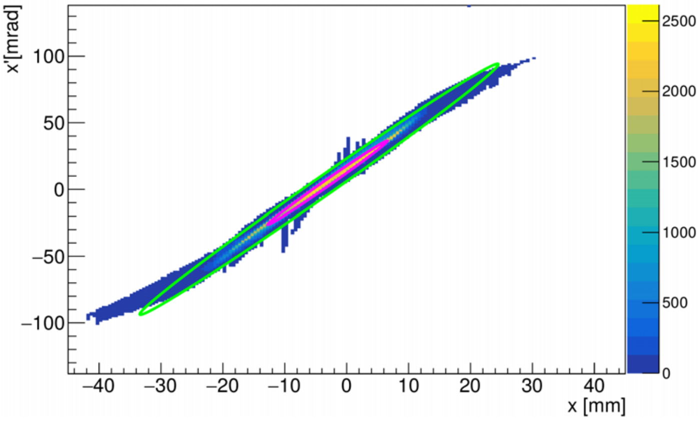

Fig. 2.1 Measured beam emittance, rms (violet) and 9rms (green) ellipses. The beam considered is a 55 mA H^+ at 50 keV.

phase space will result in larger emittance area, because the fit tries to extend in order to cover the tales of the distorted distribution.

2.1.3 Other useful Rms quantities

Instabilities and non-linear fields could destroy beam emittance or even disrupt beam. For example consider the particles at the boundary of the beam (far from the core) which oscillates at applied field frequency, given for example from a periodic focusing system), whereas those within core oscillate at frequency which depends on the space charge.

The particles between the core and the boundary oscillates at intermediate frequency: this makes possible the occurrence of resonances in periodic focusing channel, such as the RFQ. In this last case, the situation is complicated by the intrinsic non-linearity of the RFQ bucket. Example of such instabilities are the envelope/quadrupole breathing mode and centroid (driven by image charges on the beam pipe for high current beam at relatively low energy) instabilities, described in [7].

The PIC simulations are useful tools to study the halo formation (besides the analytic models) and space charge effects. One parameter which can be used in order to calculate the halo from a known distribution is defined by Wangler and Crandall [8].

$$H = \frac{\sqrt{3I_4}}{2I_2} - 2 \tag{2.10}$$

where I_4 and I_2 are based on the second and fourth order moments of the phase space distribution. $I_2 = \varepsilon^2_{rms,x}$, while I_4 takes the expression as follow:

$$I_4 = \left\langle x^4 \right\rangle \left\langle x^4 \right\rangle + 3 \left\langle x^2 x'^2 \right\rangle^2 - 4 \left\langle x x'^3 \right\rangle \left\langle x^3 x' \right\rangle \tag{2.11}$$

For all the beam with elliptical symmetry in phase space it is possible to define the values of H depending on the phase space distribution. As a reference, $H = 0$ for K-V distribution, 0.25 for 4-D Waterbag and 1 for Gaussian distribution. Halo occurs when $H > 1$ in multiparticle simulation.

2.1.4 Mismatch

If the injected beam ellipse is not matched to the focusing system, there will be additional oscillations of the rms beam projections. Generally, beam matching means that the beam-density contours coincide with the ellipses corresponding to particle trajectories. Consider a beam with a phase space which can be well described with phase space ellipse traveling through a periodic focusing lattice. For every s axial coordinate the matched beam Twiss parameters exist α_m, β_m. If the beam Courant-Snyder parameters are α_x, β_x, it is possible to define mismatch parameter [9] such as:

$$M = \left[1 + \frac{\Delta + \sqrt{\Delta(\Delta + 4)}}{2} \right] - 1 \tag{2.12}$$

Where $\Delta = \Delta\alpha_m^2 - \Delta\beta_m \Delta\gamma_m$ and $\Delta\alpha_m = \alpha_x - \alpha_m$. The mismatch factor has the property that the maximum beam size for the mismatched beam is larger than the one for a matched beam by a factor $1 + M$. Thus, a mismatched beam with $M = 0.1$ would have a 10% larger maximum projection. This may lead to losses and/or excitation of space charge instability of the beam along the focusing channels, with consequent emittance degradation.

2.2 Plasma parameters and beam space-charge

When the beam current is high enough that the self fields cannot be neglected in comparison to applied fields, the mathematical treatise of the beam dynamics gets more difficult. The self-fields are function of the charge and current distributions of the beam. At the same time, the charge and currents distributions are affected by the applied/self fields in such a way that a loop is created.

The force between the particles in the beam can be divided between "smooth" and "collisional". The collisional forces is given by the interaction of the single particle with its immediate neighbors: this force depends on the coordinate of each particles. On the contrary, the "smooth" part allows to describe the mutual interaction between particles as smoothed average force: in this case the force on the particle depends on the general coordinates which apply on the charge or current distribution. If the collisional force can be neglected, the self-field potential can be calculated via the Poisson equation:

$$\nabla^2\Phi = -\frac{\rho}{\varepsilon_0} \tag{2.13}$$

where Φ is the self-field potential, ρ is the charge distribution density and ε_0 is the vacuum dielectric constant. For a cylindrical beam with uniform density (radius 1 cm) and infinite length, the solutions of the Poisson equation for different beam currents are shown in Fig. 2.2. The beam is propagating in a grounded drift ($V = 0$, radius 7 cm). ρ depends on $\beta = 0.0103$ (relativistic ratio), I beam current, r_p pipe radius and a:

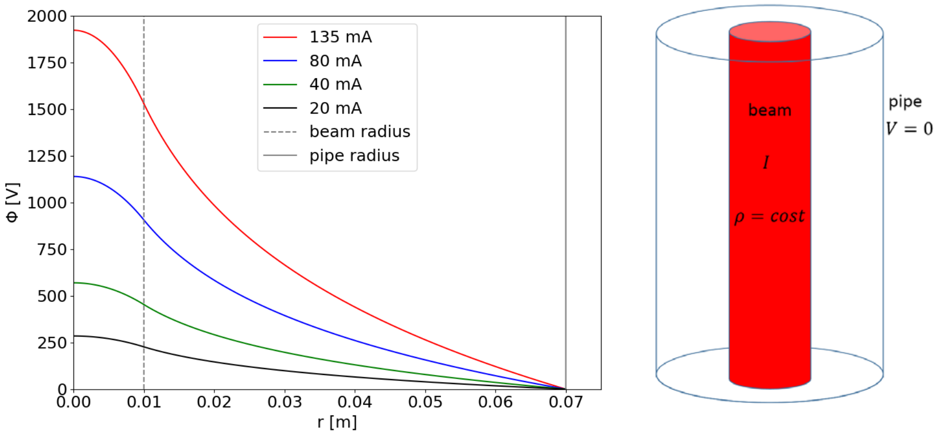

(a)

(b)

Fig. 2.2 Solution of Poisson equation for uniform density infinite length cylinder. (a) Φ is shown vs radial coordinate. The beam and the pipe radius are shown. (b) Sketch of uniform infinite length cylinder propagating in a drift grounded,

As far as the current increases, so does the maximum of potential. Thus, the potential maximum Φ_{peak} indicates the "strength" of the space-charge interaction between the beam particles. Later on, the self-field potential given by single species will be called Φ_{un}, while the over-all potential given by the ensemble of ions and electrons will be indicated as Φ.

It is possible to determinate which part of the mutual force is predominant looking at the Debye Length λ_D, and, in particular, looking at the number of particle enclosed in sphere of radius λ_D (plasma parameter). If a test charge is placed into a neutral plasma having temperature T and equal positive ion and electron densities n, the excess electric potential set up by the charge is effectively screened off in a distance λ_D by charge redistribution of the plasma. This effect is known as Debye shielding. The Debye length in an non relativistic plasma is defined by the ratio between the rms-thermal velocity $v_{th} = (k_B T/m)^{1/2}$ and the plasma frequency ω_p. The plasma frequency can be associated with the beam intensity I:

$$\omega_p = \left(\frac{q^2 n}{\varepsilon_0 m}\right)^{1/2} = \left(\frac{qI}{\pi\varepsilon_0 mc\beta a^2}\right) \tag{2.14}$$

where a is the beam radius, m is the particle mass, c is the light velocity, q is the particle charge, I is the current, ε_0 is the dielectric vacuum constant. Substituting the above quantities in the ratio it is possible to get:

$$\lambda_\mathrm{D} = \frac{v_{th}}{\omega_p} = \left(\frac{\varepsilon_0 k_B T}{q^2 n}\right) \tag{2.15}$$

where k_B is the boltzamnn constant. when the plasma is composed of different species which are not in thermal equilibrium (such can be the case of ions and electron in a LEBT transfer line) the Debye length becomes [10]:

$$\lambda_\mathrm{D} = \sqrt{\frac{\varepsilon_0 k_b/e^2}{\frac{n_e}{Te} + \sum_i \frac{z_i^2 n_i}{T_i}}} \tag{2.16}$$

e is the electric charge, T_e and T_i are the electron and ion temperatures, n_e and n_i are the electron and ion densities respectively. The volume of the sphere of sphere of radius λ_D is called plasma parameter: depending on the number of particles enclosed into the sphere, it is possible to classify the different plasmas:

$$\Lambda = \frac{4\pi}{3} n\lambda_\mathrm{D}^3 \sim \left(\frac{k_B T}{q\Phi_{ip}}\right)^{1/2} \tag{2.17}$$

where Φ_{ip} is the average potential energy due to its nearest neighbor distance. Comparing the Debye length with the beam radius:

- if $\lambda_{\mathrm{D}} >> a$ the screening will be ineffective and single particle behavior will dominate. In low current beams, the particle density is low and therefore the Debye length diverges.
- if $\lambda_{\mathrm{D}} << a$ the collective forces plays important role, due to the fact that the Debye screening plays an important role.

If the second case is verified, it is important to evaluate the contribution from the "collisional" and "smooth" part of the force. In order to do so, the Debye length can be compared with the interparticle distance: in other words, the plasma parameter. If $\Lambda >> 1$, "smooth" functions can be used in order to described the system: the charge density and the fields of the system can be described as a continuous function which does not depend on the single particle position (x_i, y_i, z_i) but on the system coordinates (x, y, z). This is possible due to the fact that the particle density in phase space can be described differently form the not smoothing varying function (in 1D) $N(x, v) = \sum_i \delta(x - x_i)\delta(v - v_i)$. In fact, it is possible to demonstrate [7] that if the collisional component of the forces acting on the system is negligible, N can be averaged over some box in phase space obtaining the function f:

$$f(x, v) = \frac{1}{\Delta x \Delta v} \iint_{\Delta V} N(x, v) dx dv = \langle N(x, v) \rangle \tag{2.18}$$

which is a "smooth" varying function. If $\Lambda << 1$, then the mutual forces becomes dominated by the collisional part and $N = f + \delta f$, where $\langle \delta f \rangle \neq 0$. In the IFMIF/EVEDA LEBT, the plasma parameters are shown in Fig. 2.3. The electron energies mainly varies from hundreds to tens of eV depending on the region of the LEBT and on the residual potential of the beam. The densities are of the order $10^{15} - 10^{16}$ m^{-3}.

The plasma parameter for the IFMIF/EVEDA LEBT is on the order of 10^5- 10^6: therefore it is possible to describe the theoretical model via smooth functions on the charge and field distribution.

2.3 Envelope equation with space-charge

Before writing the envelope equation for not negligible space charge field, it is convenient to define the concept of generalized perveance. The plasma frequency, as well as the Debye length depends on the radius of the beam distribution a. As far as a decreases, the plasma frequency increases such as 1/a. As an example, in the beam waist region in the IFMIF/EVEDA LEBT, the dimension of the beam can decrease down to 3 mm. For a deuteron beam of 135 mA, $\omega_p = 91.7$ MHz.

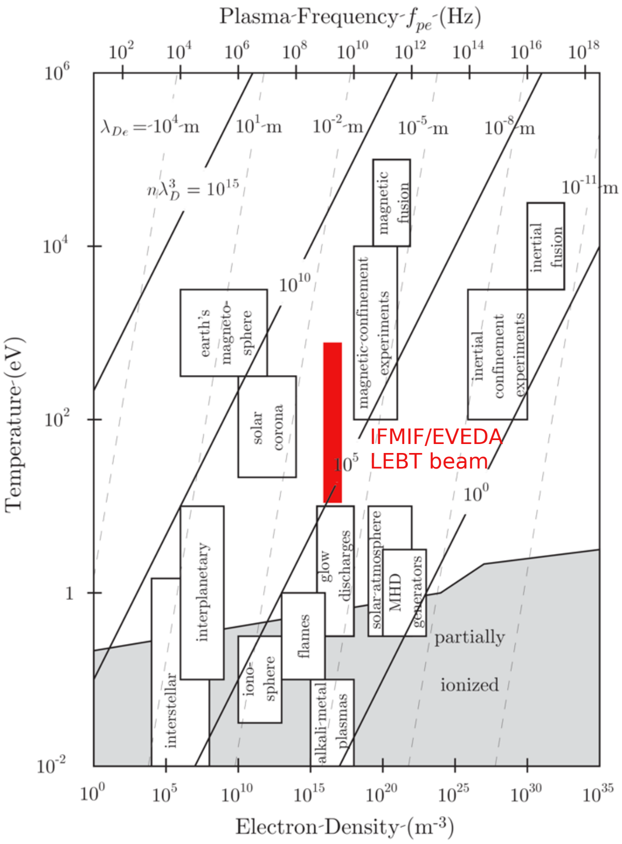

Fig. 2.3 T_e vs n_e plot. The IFMIF/EVEDA reference area is displayed [10], for the electron population at the steady state.

In the middle of the LEBT, the dimensions of the beam can increase up to 23 mm of equivalent distribution rms radius, leading to plasma frequency of 19.0 MHz. It is therefore convenient to introduce an independent variable (respect to the beam radius) which takes into account the "strength" of the collective effects respect to the beam energy. This variable derived from the plasma frequency is called by generalized perveance Q. Considering an elliptical symmetry beam:

$$Q = \frac{qI}{2\pi\varepsilon_0 m\gamma^3\beta^3c^3} = \frac{\omega_p^2 r^2}{2\gamma^3\beta^2c^2} \tag{2.19}$$

where $\gamma = 1/(1-\beta^2)^(1/2)$.
The perveance term indicates the ratio between the potential energy respect to the kinetic energy of the beam. Considering a uniform density axial symmetric beam in a focusing lattice with focusing strength $K(s)$ the envelope equation for the matched beam obeys to the following equation:

$$a''(s) + K(s)a(s) - \frac{Q}{a(s)} - \frac{\varepsilon^2}{a^3(s)} = 0 \tag{2.20}$$

where ε is the emittance of the beam. The beam is defined emittance dominated when, considering the point where the beam radius is equal to a, the ratio between the two defocusing terms $Qa^2/\varepsilon^2 \to 0$; on the contrary, when $Qa^2/\varepsilon^2 \to \infty$ the beam is space-charge dominated. In reality, the emittance is not constant due to the nonlinear forces generated by the space-charge field. In order to follow the evolution of this parameter, it si possible to express the moments of the KV distributions [6] directly from the beam distribution. The moments needs to be calculated at each step from the "real" distribution:

$$a = 2\left\langle x^2\right\rangle^{1/2} \qquad \varepsilon^2 = 4[\left\langle x^2\right\rangle\left\langle x'^2\right\rangle] - \left\langle xx'\right\rangle^2] \tag{2.21}$$

The Eq. 2.21 is exact for the KV distribution, while it is a good approximation for the other distributions [11]. It is clear from the envelope equation that proton beam with 50 keV and deuterons beam with 100 keV with equal emittance and same applied focusing term (K) must have half proton beam current respect to deuteron (i.e. same perveance than deuterons) in order to obey the same dynamics. This fact influenced the commissioning plan because it supplies a powerful tool to test the BD of RFQ and the other parts of the machine with a lower power beam (a factor of 4 less than deuteron case, half energy and half current).
In the magnetostatic like IFMIF/EVEDA LEBT, the electrons generated due to several phenomena are accumulated by the positive charge of the main beam, compensating the space-charge potential. Therefore, $Q = Q(s)$ term varies with the axial coordinate.

Q and ε have not-constant behaviors of the defocussing terms lead to a very complicate description from the beam dynamics point of view. An example of the trends of the thermal (ε^2/a^3) and space-charge (Q/a) terms are shown in Fig. 2.4, for the case of H$^+$ 55 mA and 50 keV beam. The emittance growth (given by the coupling from the solenoid nonlinearities and space charges) and the neutralization level of more than 95% between the solenoids imply that the beam becomes more emittance dominated along the LEBT . The sensitivity to the percent of the level of neutralization is very high, as can be seen in 2.4

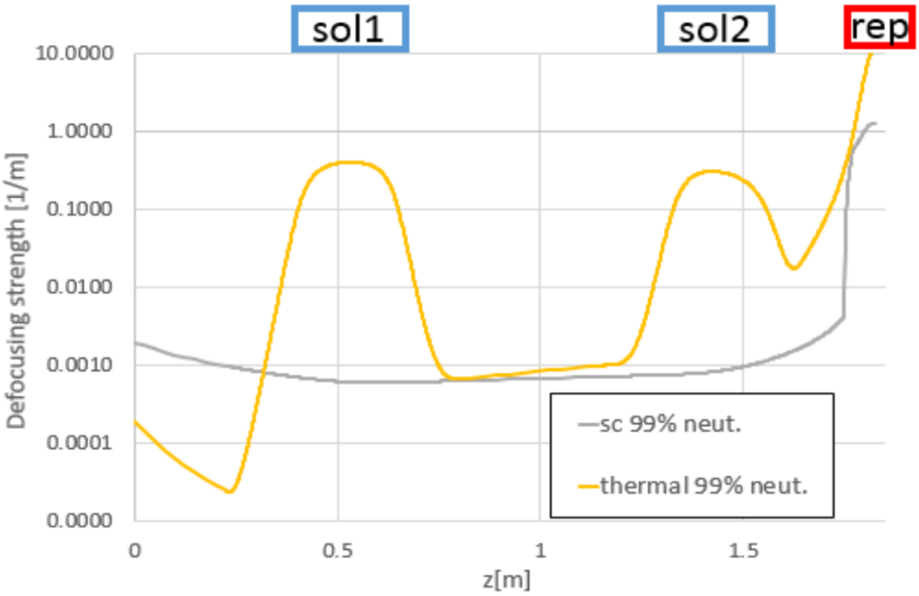

Fig. 2.4 Trend of the thermal term and space charge term respect to the LEBT axial coordinate in space charge neutralization regime.

As far as the beam approaches to the end of the LEBT (at 2 m) the beam radius decreases, the thermal term diverges as $1/a^3$, while the space-charge term diverges as $1/a$. The two bumps in the thermal term are due to the solenoids effect: in the field area the emittance is not an invariant of the motion as anticipated before.

2.3.1 Depressed phase advance

If the space charge forces are not negligible, it is convenient to distinguish between the the phase advances in the absence of space-charge (already defined in Eq. 2.5), called undepressed and the depressed phase advance (when the space charge effects are not negligible). Calculating $\beta = a_0^2/\varepsilon$, Eq. 2.5 becomes:

$$\sigma_0 = \varepsilon \int_{s_i}^{s_i+L} \frac{ds}{a_0^2} \tag{2.22}$$

The depressed phase advance, based on a from Eq. 2.20 is given by:

$$\sigma = \varepsilon \int_{s_i}^{s_i+L} \frac{ds}{a^2} \tag{2.23}$$

The ratio σ/σ_0 indicates the strength of space-charge respect to the applied focusing. If the ratio is lower than 0.5, the regime is space-charge dominated, otherwise, the beam dynamics is kinetic (emittance) dominated.

2.3.2 Space charge neutralization

The theory treated up to here takes into account a single species beam. In reality, in the low energy high intensity transfer line the beam transport is affected also by other species: in particular, the space charge compensation phenomena (or space charge neutralization) can occur with the generation and superposition to the primary beam by opposite charge particles. Therefore, an important part of the beam dynamics characterization of this kind of transfer line concerns the estimation of the so called secondary plasma effect.

Two s.c.c. models are considered in this thesis: the constant/static and dynamic model. In a constant model of neutralization, the perveance is simply reduced of a factor η which is called the space charge compensation ratio:

$$Q = Q_0(1 - \eta(s)) \tag{2.24}$$

where Q_0 is the un-neutralized beam preveance, and η is the s.c.c. term. The value can be determined by external measurement, such as from the four grid analyzer (see Chapter 3), via the ratio between the compensated respect to the uncompensated beam potential (i.e. $\Delta\Phi/\Delta\Phi_{un} = \Phi_{peak}/\Phi_{un,peak}$)

In dynamic model of neutralization, the s.c.c. is calculated directly from the electron charge distribution which is superimposed to the ion distribution. Therefore, for this model both the ions and electrons dynamics need to be calculated. In such case $\eta = \eta(r,z)$.

In a magnetostatic LEBT (such as IFMIF/EVEDA) electrons are supplied mainly by two sources: the reaction between the beam ions and the residual gas, or the collisions with the pipe.
As far as the s.c.c., which belongs from the interaction between the beam and the residual gas, it depends on the following factors: the gas density n_{gas}, the cross section σ_i (which contains the dependance on the target atomic properties) and the velocity of the ions v. The cross sections trend were described in [12] via semi-empirical formulas, where the parameters are fitted with experimental data. It is possible to calculate the time needed by the electrons to compensate the space-charge field [6] of uniform beam density drifting in a field free region of space filled with constant gas pressure background:

$$\tau_N = \frac{1}{n_{gas}\sigma_i\beta c} \tag{2.25}$$

were n_{gas} is the scatter centers of the gas, σ_i is the ionization cross section. If the gas is constituted by several species uniformly mixed, Eq. 2.25 can be expanded as follows:

$$\tau_N = \frac{1}{\sum\limits_{i=1}^{N} \beta_i c n_{g,i}\sigma_i} \tag{2.26}$$

Similarly, also the new electrons undergo ionization process with the residual gas. The cross section ranges from $10^{-20} - 10^{-21} m^2$
Concerning the electron ejected from the metal boundaries due to ion collision, the processes depends on the energy exchange between the ion traveling in the metal and electrons in the metal. The emission can be related to the kinetic energy of the projectiles (K.E. kinetic energy emission) or to the sum of potential to produce a respective ion (potential emission). In case of deuterons and protons at 100 and 50 keV respectively, the velocity is in the range of kinetic emission. The secondary electron emission γ depends then on the electronic stopping power $S_e(E_0)$ [13]:

$$\gamma(E_0) = \frac{1}{2} PL \frac{S_e(E_0)}{J} \tag{2.27}$$

where J is the mean energy that the projectile must spend in order to create an electron pair, P is the average escaping probability and L is the mean attenuation length. For the considered energy and materials, the SEY's are not negligible ($\gamma > 1$).

The cross section implemented in the code for both the process will be presented in Chapter 6.

2.4 Beam Dynamics softwares

Three beam dynamics softwares were used for this thesis work, each covering a part of the accelerator: Tracewin[14] was used for describing the LEBT in the constant neutralization approximation and the RFQ with TOUTATIS [15] code, AXCEl-INP [16] was used to determine the extracted beam from extraction column properties and the curvature of the plasma meniscus. In WARP [17] it was model the entire LEBT starting from the partial part of the extraction system. In the last part of the work the entire extraction system was simulated, starting from the plasma meniscus.

2.4.1 Tracewin

The Tracewin code is a Particle in Cell Code: at each step a mesh is superimposed on the bunch, which allows a smoothing of the fields to reduce the effects of artificially large forces that would otherwise be caused by binary encounters between macro-particles. The number of particles in each cell is counted, and the smoothed space-charge force acting on each particle is obtained by summing the fields from the charges in each cell. Finally, the forces are applied to deliver a momentum impulse to each particle. The particle pusher integrates the equation of motion in space via the Leap Frog Method. The choice to integrate in space considerably speed up the calculation time, but only the steady state is represented and only one particle species interaction per time can be followed. The code calculates the self-filed potential from the Poisson equation within the beam boundaries. After the beam boundaries, the electric field trend of a Gaussian charge distribution with the sigma of the beam and infinite boundaries is assumed. The code can gather the information on the applied field from the used input field map or the analytic models. For simulating the RFQ, TOUTATIS is implemented in the code. TOUTATIS is a PIC code that uses the finite element method accelerated by multigrid technique to solve the Poisson equation. The multigrid methods is based on the usage of several multigrids (coarser and finer) in order to estimate the residual (which is the solution of the itertive Poisson equations). Both Tracewin and Toutatis implement adaptive mesh refinement in order to keep the beam/mesh ratio fixed.

2.4.2 WARP

WARP is an extensively developed open-source particle-in-cell t-code designed to simulate charged particle beams with high space-charge intensity. There are many possible field solvers that can be used in order to solve the Poisson equation. In this thesis the multigrid Poisson solver with mesh refinement was chosen in order to simulate the LEBT system.
The particle pusher is integrated in time with the Leap Frog Method, but also the hybrid dirft Lorentz pusher can be used in order to correctly estimate the charged particle gyroradius. At each time step the PIC cycle performs the following loop:

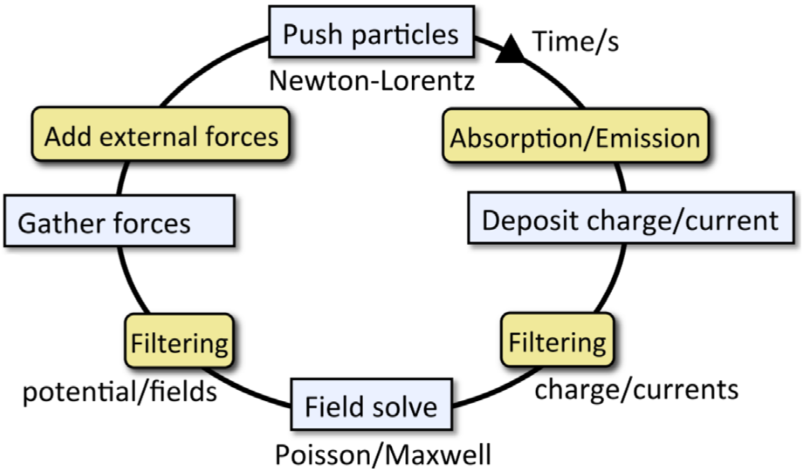

Fig. 2.5 WARP PIC cycle [18]

WARP code is capable of transporting multispecies beam (such as electrons and deuteron) as well as to perform, at each step, Montecarlo simulation for ionization process and secondary particle emission. The *t* integration takes more time respect to a s-code to be performed, but allows to study the transient time. The runs were parallelized with the MPI: in particular, the simulation volume was divided in 20 longitudinal domains. Each domain was covered by a physical core of the machine.

2.4.3 AXCEL

AXCEL-INP is an axial symmetric Vlasov-solver, which uses the finite difference method in order to solve the equation. That implies to solve the Poisson equation and to determine the particle distribution function which influences the Poisson equation itself.
The first iteration calculates the potential from the self fields solving the Laplace equation. In the second step, the particles are tracked. The new potential map, computed with the Poisson solver which takes into account the charge particle distribution projected on the grid from the

tracking rays, is generated. New iterations of the second step are done up to the steady state is reached, ensuring the self consistency.
The AXCEL-INP software assumes a plasma in thermal equilibrium and no collisions or ionization are implemented. Due to the large perveance of the beam (5.0×10^{-3}), in order to obtain reasonable estimation at 19.6 mm from the plasma electrode, a constant neutralization was set to 97% after the -100 V equipotential lines on axis. No plasma heating is considered; within the plasma sheet, the electrons have a Maxwell-Boltzmann distribution which depends on the plasma potential Φ_p and the electron temperature T_e. The electron density follows:

$$n_e(\Phi) = n_{e,0} e^{\frac{\Phi - \Phi_p}{k_B T_e}} \tag{2.28}$$

The code adds this electron distribution to the computed ion distribution when solving the Poisson equation for in the region before the plasma sheet.

Chapter 3

IFMIF/EVEDA, the test facility

3.1 The engineering test facility

In order to minimize the risks of project failures due to the demanding performances, as explained in the Chapter 1, it is important to test the accelerators parts which will face the main technological and physical challenges.

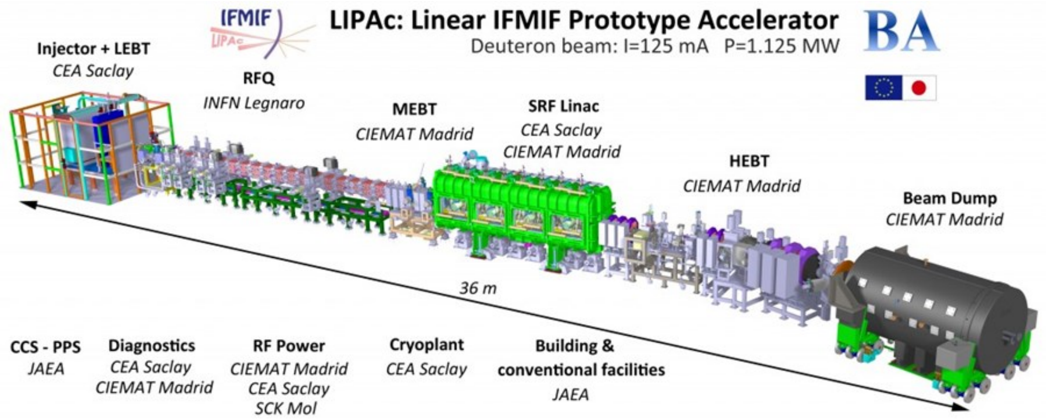

Fig. 3.1 Sketch of the LIPAc accelerator with the contributors for each part of the machine

This project phase is called IFMIF/EVEDA (Engineering Validation Engineering Design Activity)) and it is jointly developed by Europe and Japan. The purpose is to install and to commission in Rokkasho, Japan, an accelerator prototype called the Linear IFMIF Prototype Accelerator (LIPAc). The European countries are responsible to built the accelerators parts, while the infrastructure is provided to the Japan.

The LIPAc is composed of the key parts of the IFMIF accelerator. In such a way, it will obtain a CW beam of 125 mA at 9 MeV, which will collide onto a high power beam dump specifically designed for such purpose. The target performances are 1.125 MW power onto the beam dump, which will make this machine one of the most powerful of its kind [19].

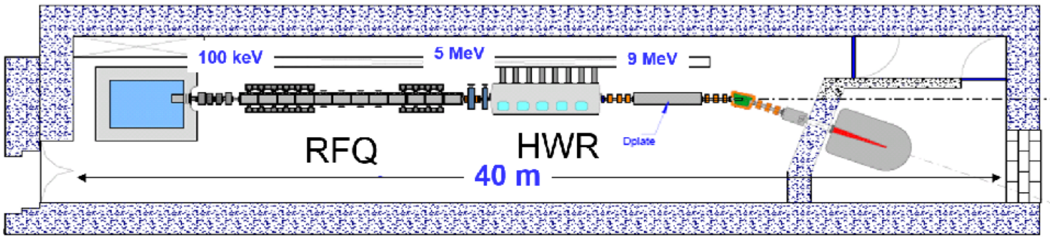

Fig. 3.2 Sketch of the LIPAc accelerator with its different parts and energies

The accelerator components and the in-kind contributions are the following:

- the ion source: the ECR (Electron Cyclotron Resonance) ion source is designed and built by CEA Saclay [20]. It consists of a 2.45 GHz RF power source with a 2 coil magnetic structure. The nominal CW beam extracted consists in 140 mA D^+ at 100 kV. For commissioning purposes, the source can extract also tens of mA of H^+ at 50 kV.

- the LEBT : is also built by of CEA Saclay [21], this final part of the injector of 2.05 m length (from plasma electrode to the end) is equipped with two solenoids of 310 mm length which are able to provide 0.76 T axial field. These two lenses need be tuned in order to match the output beam characteristics from the source exit to the RFQ input. Chopper system and a diagnostic boxes are installed in order to allow commissioning and beam control.

- the RFQ [22, 23]: is designed and built by INFN-LNL, INFN-Padova, INFN-Torino and INFN-Bologna. It consists of a CW 9.8 m long 4-vane RFQ, which will accelerate 130 mA CW D^+ up to 5 MeV. During the commissioning it will accelerate also H^+ up to 2.5 MeV with 70 mA current, which has the same beam dynamics of the nominal beam.

- the MEBT: the MEBT is an in-kind contribution of the CIEMAT [24]. It is roughly 2 m long and it is composed by one triplet (three quadrupole lens in a FODOF configuration), one doublet (two quadruples in a FODO configuration) for transverse focusing and two five-gap IH resonator bunchers for longitudinal focusing into the SRF cavities.

- the SRF Linac: (in-kind contribution of CEA [25]) accelerates deuteron from 5 MeV to 9 MeV via 8 superconducting HWRs cavities, alternated by 8 superconducting solenoids. These last elements ensure the transverse focusing. All of these devices are contained in a 6 m long cryostat cooled down by liquid helium.

- the HEBT and the power beam dump: the HEBT transports the 9 MeV D^+ beam onto the beam dump (HPBD High Power Beam Dump), via two triplets and one doublet. A 20° magnetic dipole is used in order to separate the not nominal energy particles.

3.2 The injector

The injector will inject an appropriate beam into the RFQ. It can be divided in two parts: the source and the LEBT.

Fig. 3.3 Photo of the LIPAc injector installed at Rokkasho

3.2.1 The source

The source generates charged particle beam in the following way: the magnetron generates around 1 kW RF power at 2.45 GHz, which travels through the wave guide up to the matching transformer. The matching transformer matches the impedance to the plasma chamber. In the plasma chamber, the free electrons are moving in a spiral orbit following the Eq.3.1:

$$\omega_g = \frac{eB}{m_e} \tag{3.1}$$

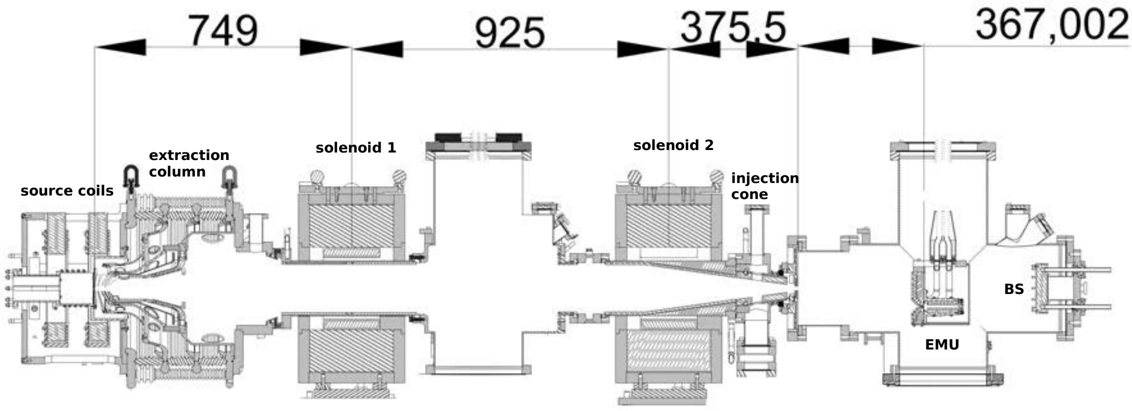

Fig. 3.4 Sketch of the LIPAc injector. The values are in mm

where B is the magnitude of the static magnetic field, e is the electron charge and m_e is the electron mass. The magnetic field is generally supplied via electromagnetic solenoids.
When the RF power with a frequency (ω_{RF}) is applied, the electrons coincidentally in phase with the electric field get accelerated, whereas the others get decelerated. The maximum energy gain occurs when the Eq. 3.2 is satisfied:

$$B_{\mathrm{ecr}} = \frac{\omega_{\mathrm{RF}} m_e}{e} \tag{3.2}$$

Every time an electron passes the resonant region, defined by B_{ecr}, it gains energy from the electric field, heating up. In the IFMIF case, for the RF frequency of $\omega_{\mathrm{RF}} = 2.45$ GHz, the magnetic field resutl $B_{\mathrm{ecr}} = 0.0875$ T. The hot electron ionizes the neutral atom, generating another electron. For the IFMIF-EVEDA source, the magnetic field in the plasma chamber is given by two electromagnetic coils, placed around it (see Fig. 3.5).
Then, the positive ion is extracted through the extraction hole, due to certain potential applied within the electrodes. The application of the extraction voltage leads to the formation of a narrow plasma meniscus (defined by $n_e = 0$ or $\nabla\Phi = 0$), shown in Fig. 3.6.
It depends on the ion density, the plasma potential, the external potential and the electron temperature. The equilibrium is reached when dynamic potential is set up between the applied fields and the plasma.

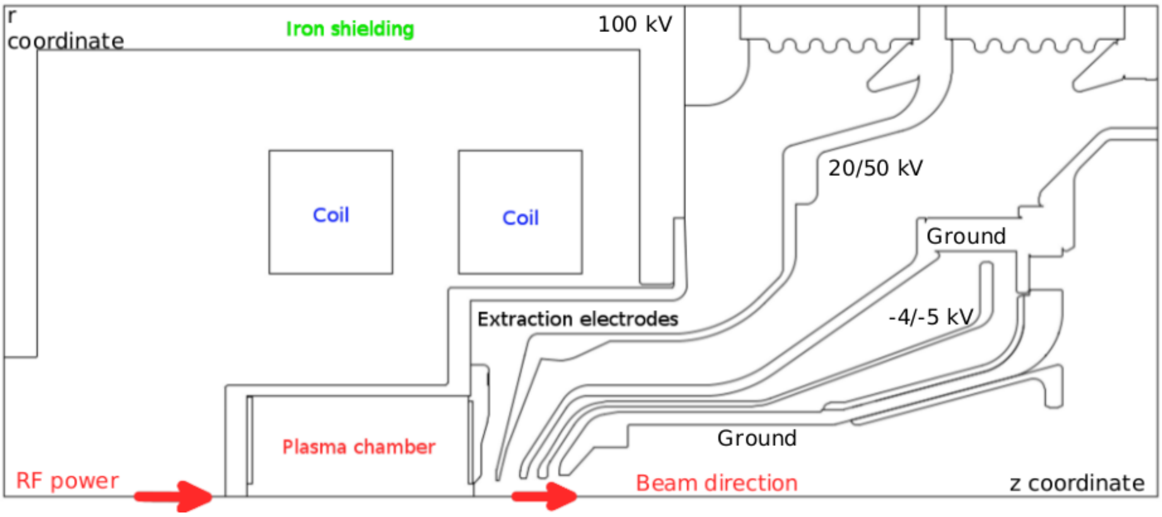

Fig. 3.5 Sketch of the center region of the source complex in cylindrical coordinates. The main parts are shown: the two source coils, the plasma chamber, the RF and extracted beam direction, the iron shielding and the extraction electron region.

The curvature and the shape of this meniscus (see Fig. 3.6) is an important phenomena to take into account for the beam optics. It is possible to evaluate its shape (convex or not) via the Child-Langmuir law.

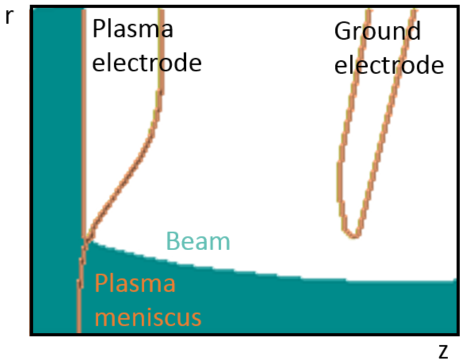

Fig. 3.6 Example of plasma meniscus in a diode system. The extraction is shown as well as the beam and the shape of the plasma meniscus. The plot presented considers the first two electrode of the extraction system.

The Child-Langmuir law

Consider a 1D problem where a single species particle of charge q and mass m_0 is at rest at the $z = 0$ coordinate. Consider two parallel plates with a distance d and potential difference of V_0 between them (diode system 3.7). If the particle at the end of the extraction is not relativistic ($qV_0 << m_0c^2$) it is possible to calculate analytically the maximum current density that can be supplied by this system (described in Eq. 3.3).

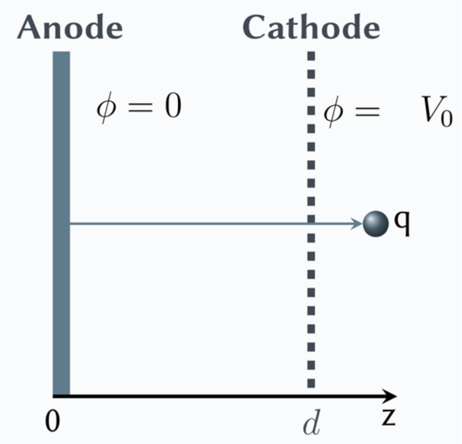

Fig. 3.7 Sketch of the diode system from which the 1D Child-Langmuir model applies.

The limitation on the extractable current comes from the longitudinal repulsion of the charged particles. The model is limited to the fixed plane emitter (the region from which the particle of mass m_0 emerges). In an ECR ion source the emitter coincides with the plasma meniscus, which can vary depending on the species densities, temperatures and plasma voltages. In general, it may be not flat, as shown in Fig. 3.6. Eq. 3.3 calculates the maximum current density obtainable from the diode system:

$$J = \frac{4}{9}\varepsilon_0 \left(2\frac{q}{m}\right)^{1/2} \frac{V_0^{3/2}}{d^2} \tag{3.3}$$

where J is the current density. It is worth to compare the Child-Langmuir with the experimental value of the current extracted. If the ratio between the current density extracted and value obtained with the Child-Langumir law is $J_{ext}/J_{CL} < 1$, a concave plasma meniscus should be expected. Otherwise a convex plasma meniscus will be set. When the $J_{ext} = J_{CL}$ the plasma meniscus is expected to be plane.

Eq. 3.3 suggest a way to scale the current density (thus the extraction optics properties) between two different species. In IFMIF/EVEDA case, it may be requested to scale between deuteron and proton: to have half current density for a half mass beam $m/2$ and the same charge q, for the same extraction geometry (i.e. the same d), the quantities must be related in this way:

$$\frac{J_{\mathrm{D}}}{2} = J_{\mathrm{H}} \qquad \Longrightarrow V_{0,\mathrm{H}} = \frac{V_{0,\mathrm{D}}}{2} \tag{3.4}$$

However, in a real source, like for the IFMIF/EVEDA case of proton beam generation, the main problem encountered for the direct scaling is the approximation of single species beam included in the model, which follows a trend of $(q/m)^{1/2}$.
As a matter of fact, the different contaminant presence may not be negligible and therefore must be included in the treatise.

Extension to multispecies for the Child-Langumir law

For a multispecies extraction it is important to expand the validity of Eq. 3.3. For a unidimensional system of parallel plates as shown in Fig. 3.7, with N number of species with mass m_i, charge q_i and ρ_i the following equations need to be solved:

$$\begin{cases} \frac{d^2\Phi}{dz^2} = \frac{\rho}{\varepsilon_0} \\ \rho = \sum\limits_{i=1}^{N} \rho_i \\ J_{tot} = \sum\limits_{i=1}^{N} \rho_i v_i \end{cases}$$

If, at the end of the diode, for any i it is verified that $q_i V_0 << m_i c^2$ (not-relativistic approximation), it is possible to explicitly calculate the velocity for any i. Substituting Eq. 3.3 into the Poisson equation of the above system:

$$\begin{cases} v_i = \sqrt{\frac{2q_i\Phi}{m_i}} \\ \frac{d^2\Phi}{dz^2} = \frac{1}{\varepsilon_0}\left[\sum\limits_{i=1}^{N} \frac{J_i}{v_i}\right] \end{cases}$$

If the chosen species to be accelerated is $i = 1$, it is possible to re-write the equation explicating the factor $\sqrt{m_1/2q_i\Phi}$:

$$\frac{d^2\Phi}{dz^2} = \frac{1}{\varepsilon_0}\sqrt{\frac{m_1}{2q_1\Phi}}\left[\sum_{i=1}^{N} J_i \sqrt{\frac{m_i}{q_i}\frac{q_1}{m_1}}\right] \tag{3.5}$$

Calling the $J_{eq} = \sum\limits_{i=1}^{N} J_i \sqrt{\frac{m_i}{q_i}\frac{q_1}{m_1}}$, which depends on the species fractions and on the charges, the familiar form of the differential equation is retrieved, but with J_{eq} instead of the single current density J:

$$\frac{d^2\Phi}{dz^2} = \frac{1}{\varepsilon_0}\sqrt{\frac{m_1}{2q_1\Phi}}J_{eq} \tag{3.6}$$

Eq. 3.6 can be solved, and taking into account the initial condition $\Phi(0) = 0$ and $\Phi'(0) = 0$, it is possible to write the scalar potential as a function of z:

$$\Phi(z) = \left(\frac{3}{2\varepsilon_0}\right)^{4/3} \left(J_{eq}\right)^{2/3} \left(\frac{m_1}{2q_1}\right) z^{4/3} \tag{3.7}$$

If we apply the boundary condition $\Phi(d) = V_0$, the standard form of the Child-Langumir equation is obtained, but with J_{eq} defined as Eq. 3.6.

$$J_{eq} = \frac{4}{9}\varepsilon_0 \left(\frac{2q_1}{m_1}\right)^{1/2} \frac{V_0^{3/2}}{d^2} \tag{3.8}$$

Comparing Eq. 3.8 with Eq. 3.3: for any choice of $V_0^{3/2}/d^2$ the current density of m_1 species sustainable in case of single species fraction is always larger than in the case of multispecies extraction. The net effect results in changed optics between the two cases. J is the sum of all the current densities of the different species defined in the system above. Defining ξ_i the current density fraction of the single species respect to J, it is possible to write:

$$J_i = \xi_i J \tag{3.9}$$

Therefore Eq. 3.8 becomes:

$$J\sum_{i=1}^{N} \xi_i \left(\frac{m_i}{q_i}\frac{q_1}{m_1}\right)^{1/2} = \frac{4}{9}\varepsilon_0 \left(\frac{2q_1}{m_1}\right)^{1/2} \frac{V_0^{3/2}}{d^2} \tag{3.10}$$

For the IFMIF/EVEDA case, the ion charge $q_i = 1\ \forall i = 1,..N$; in this case, the scaling for the multispecies depends on the mass ratio:

$$J\sum_{i=1}^{N} \xi_i \left(\frac{m_i}{m_1}\right)^{1/2} = \frac{4}{9}\varepsilon_0 \left(\frac{2e}{m_1}\right)^{1/2} \frac{V_0^{3/2}}{d^2} \tag{3.11}$$

If proton beam is extracted, the molecular ions H_2^+ and H_3^+ are expected as contaminants. Taking the normalized current density J/J_{max}, where J_{max} is the maximum current density obtainable with a single species extraction for a maximum potential V_{max}, a fixed gap distance and a normalized gap potential V/V_{max} it is possible to see the effect on the extracted current on the plot in Fig. 3.8.

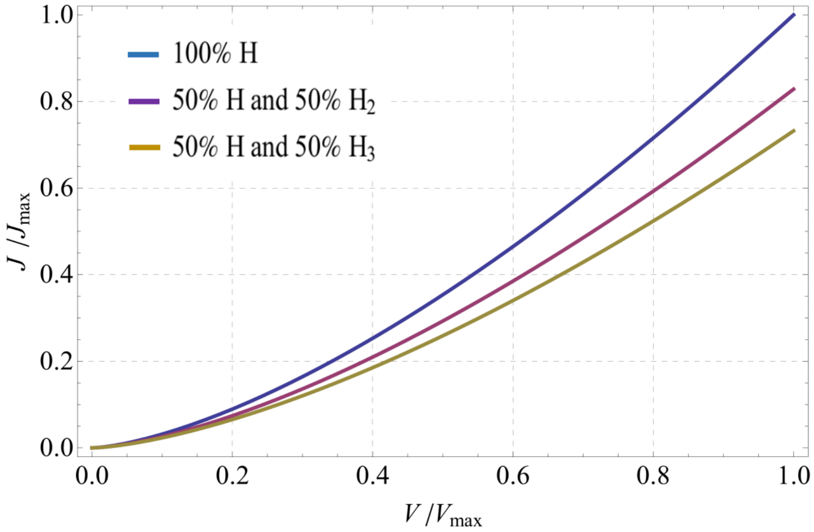

Fig. 3.8 Normalized current densities J/J_{max} with different contaminant species for a fixed ratio of 50%, respect the normalized gap voltage V/V_{max}. The maximum current density correspond to the smaller mass species singly extracted extraction.

As the contaminant mass becomes larger, the sustainable current decreases, in agreement with the increased Coulomb repulsion term in the source, which depends on the m/q ratio. In conclusion, Eq.3.11 shows that in order to maximize the extraction performance it is important to minimize the contamination. As an example, in order to scale a deuteron beam density current of 140 mA/cm^2 with a deuteron fraction of 93%, for a H fraction of 60% the current density needs to be reduced from 70 mA/cm^2 (simple scaling) down to 65% mA/cm^2

The extraction system

The extraction system is the source part where the ions are extracted and accelerated from the plasma. In IFMIF/EVEDA case, the extraction is composed of an accelerator column made by a system of five electrostatic lens, as shown by Fig. 3.9:

- The plasma electrode (P.E.) is the first electrode of the system and it is placed at the nominal voltage (i.e. 100 kV for d, and 50 kV for p). Within the PE, the plasma meniscus is generated, whose shape depends on the plasma parameters.
- The intermediate electrode can have a varying voltage, in order to tune the plasma meniscus generated in the P.E. This is possible due to the fact that it sets the voltage difference in the first gap and in the second gap.

- The first ground closes the extraction gaps system and protects the following electrodes form uncontrolled beam.
- The repeller electrode has a negative potential. The main effect is to repel the electrons coming from the LEBT, in order to avoid them to enter in the plasma chamber with tens of keV of kinetic energy. As a second effect, it defines a geometric boundary where the neutralization starts to apply. This have an huge effect on the final extraction output beam.
- The 5^{th} and last electrode is placed at ground potential (2° G).

The main difference with respect the diode system is the presence of the intermediate electrode, which creates two gaps instead of one. Changing the potential in the intermediate electrode helps to tune and modify the plasma meniscus, but with the price of creating two gaps. A focusing/defocusing kick between the two gaps is then generated. It depends on the electric fields before and after the intermediate electrode hole, as described in [6]. Its effects is not negligible in the extraction optics.

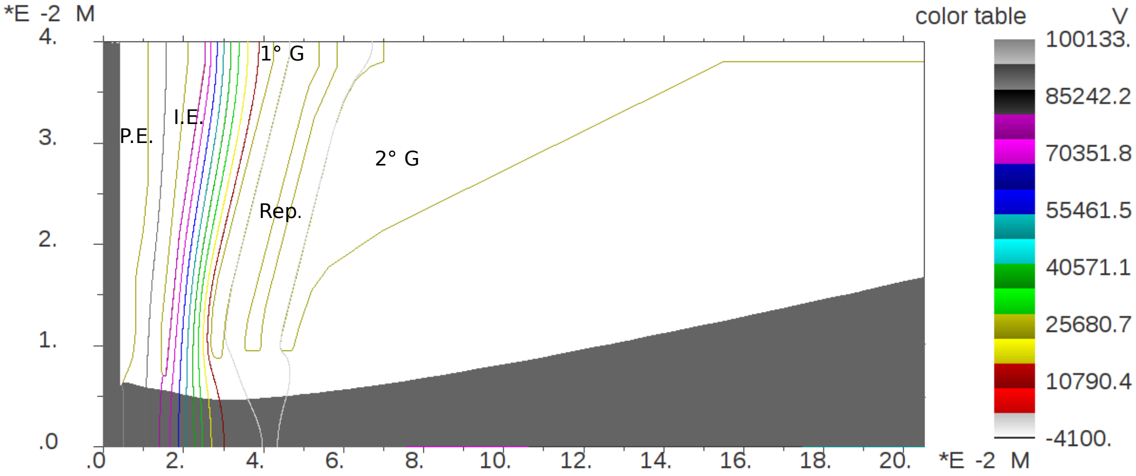

Fig. 3.9 RZ plot of the extraction system with a typical extracted beam of 156 mA with a 20 kV potential different between the P.E. and the intermediate electrode: the equipotential lines and the beam trajectories are shown

In order to evaluate its effect, combined with the plasma meniscus shape, it is important to simulate the system with an appropriate software. Nevertheless, the scaling optics can be used in order to predict the beam behavior, via the formula expressed in Eq. 3.11, and was verified via simulations. In order to do so, for this kind of extraction, the five electrode system is reduced to the plasma and intermediate electrode; the extended Child-Langmuir and all the other considerations about the plasma meniscus apply to the this reduced system.

The charged particles in the extraction system is also affected by the fringe field of the magnetic field generated by the source coils. The effect of decreasing magnetic field results in a rotation of the beam, which leads to an emittance increase given by Eq. 3.12:

$$\varepsilon_{\mathrm{rms,n}} = \frac{r^2 B_0}{8c}\frac{q}{m} \tag{3.12}$$

where r is the plasma extraction hole, q is the charge and B_0 is the axial magnetic field. Considering $r = 6$ mm, $B_0 = 0.0880$ T and a deuteron beam the result is $\varepsilon_{\mathrm{rms,n}} = 0.05$ mm mrad, which is not negligible considering that the requirements of the emittance at the end of the LEBT is $\varepsilon_{\mathrm{rms,n}} \leq 0.3$ mm mrad. This effect is a direct consequence of Busch theorem [6]: the azimuthal momentum is a constant of the motion in an axis-symmetric magnetic field, such as the source coils. At the plasma electrode position, the ion beam has a low temperature (order of 0.1 eV/k_B). Therefore, the kinetic component of the azimuthal momentum is almost 0.

$$p_\theta = mr^2\dot{\theta} + \frac{1}{2}qB_z r^2 \simeq \frac{1}{2}qBr^2 \tag{3.13}$$

the azimuthal momentum at the position where $B_z \simeq 0$ (generally coincidents with the end of acceleration), becomes, due to the Bush theorem:

$$p_\theta = mr^2\dot{\theta} = \frac{1}{2}qB_z r^2 \tag{3.14}$$

Thus, the gain of azimuthal momentum at the end of the acceleration section (where the B_z is supposed to be negligible) is directly dependent on the magnetic field on axis and on the square of radius. In order to obtain the magnetic field data to be studied and simulated, it was necessary to simulate the magnetic field of the source coils with finite element method due to the presence of the iron shield which surrounds the plasma chamber; its role consists indeed of avoiding the fringe field propagation in the extraction system. The effect of the iron shielding onto the extraction part is shown in Fig. 3.10:

The shield substantially reduces the magnetic field on the extraction region, changing the beam transport and the other charged species behavior, such as the free electrons.

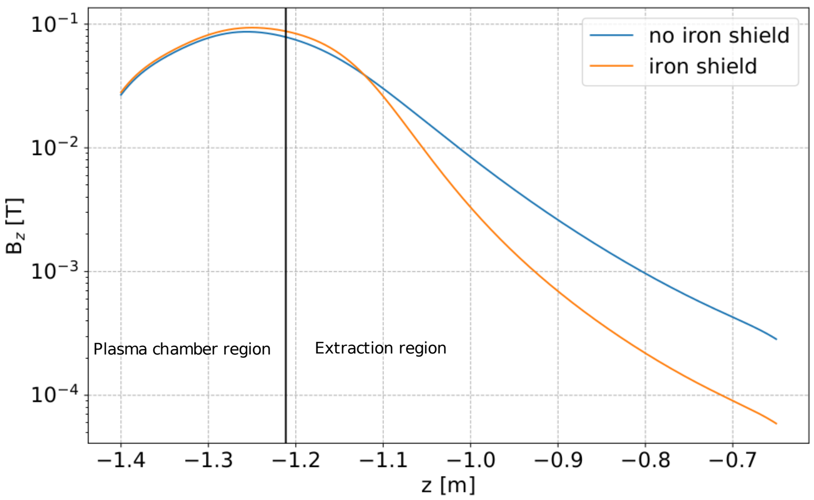

Fig. 3.10 Trend of the axial magnetic component respect to the axis distance: two trends are shown:one with the magnetic shielding opened (blue line) and the other one with the complete magnetic field. It is possible to notice the larger field in the extraction region.

3.2.2 The LEBT

The LEBT is composed of two solenoids, one diagnositc box and an injection cone. For commissioning purpose another diagnostic box is available for studying the beam behavior during commissioning operations. The diagnostic boxes are equipped with beam diagnostics (which will be discuss later) and a chopper for pulse beam operation.

In the injection cone an electron repeller is installed, whose purpose is to built up a Coulomb barrier in order to deplete the electron presence at the RFQ entrance.

As far as the vacuum is concerned, two turbo pumps are installed at the exit of the extraction column and between the two solenoids.

A smaller pump is placed at the injection cone, in order to aspirate the outgassing caused by the contaminant or by the chopped beam collisions. A spare pump is used in case the third diagnostic box is installed.

In order to improve the space charge compensation, the LEBT foresees the possibility to inject an external gas (such as Kr) in the first diagnostic chamber, located in the middle of the two solenoids.

Solenoids

The LEBT focusing system is composed of two solenoids of 310 mm length (iron shield included) and 120 mm radius bore (beam axis windings). The B_z field profile for example values of solenoids for D beam is shown in Fig. 3.11

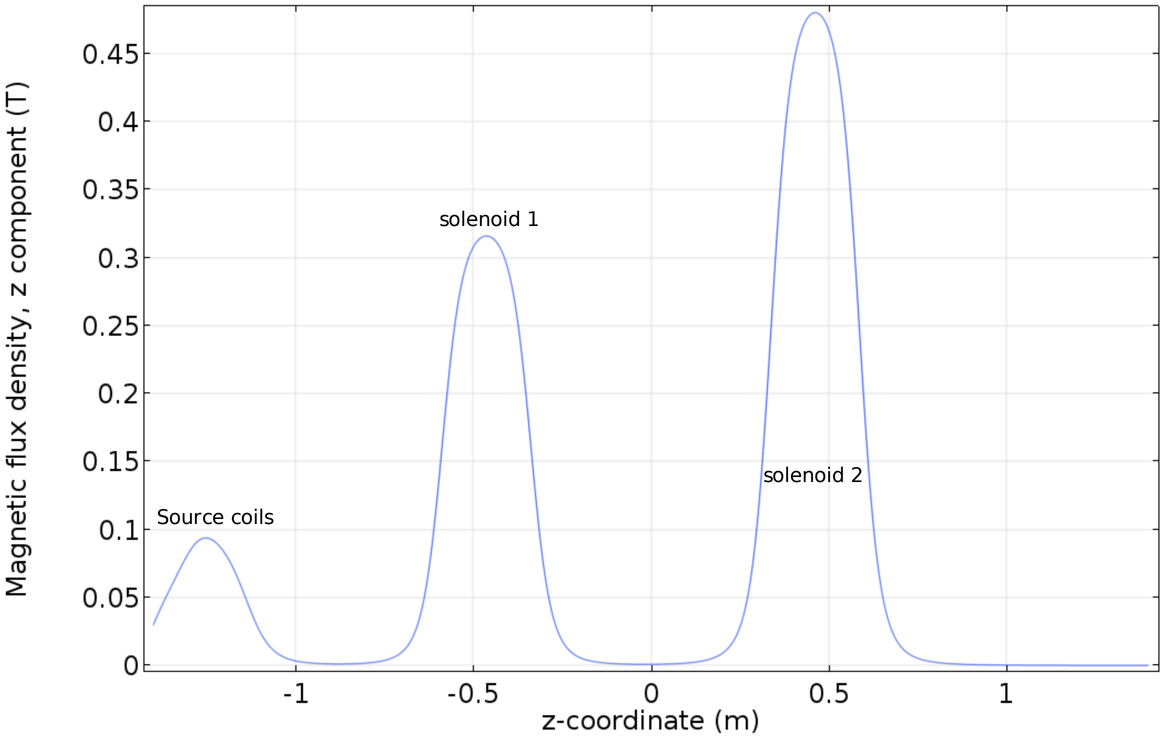

Fig. 3.11 Trend of B_z along axis for the LEBT and injector. Example values for D beam are shown

The focusing strength of the solenoid with respect to a certain species can be evaluated with the following equation (in paraxial approximation):

$$\frac{1}{f} = \left(\frac{q}{2mc\beta\gamma}\right)\int_{z_1}^{z_2} B^2 dz \tag{3.15}$$

for $B_z = 0.31$ T the result is $f_d = 0.828$ m in case of deuterons, while $f_e = 2.2 \times 10^{-6}$ m for electrons with 1 keV energy. Due to the sensitivity of the electrons to lower values of magnetic fields, the entire LEBT map was imported into the simulations which involve the secondary electrons.

The solenoids incorporate two xy steerers, in order to correct the beam orbit at the RFQ injection.

3.3 Beam instrumentation of the LEBT

This section reports the main beam instrumentation used in the LEBT during the commissioning operation.

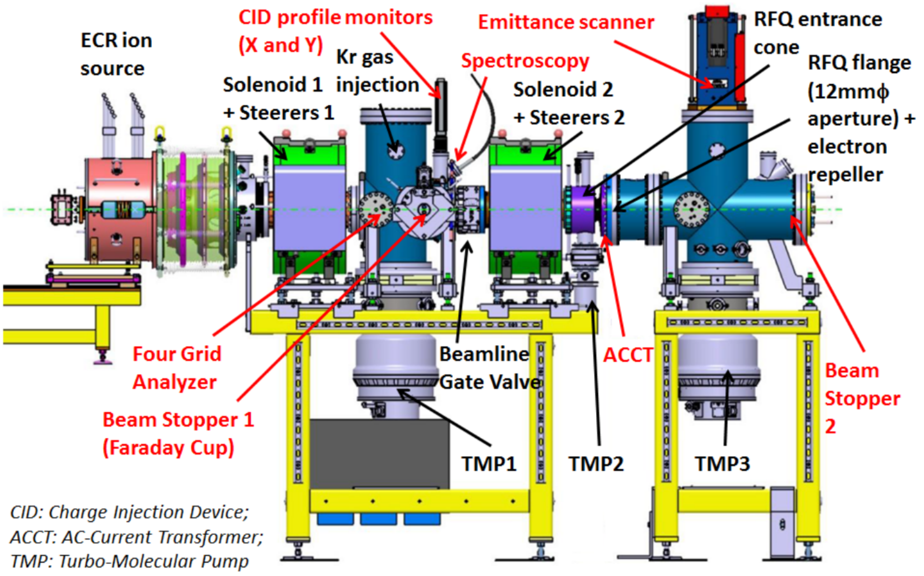

Fig. 3.12 Sketch of the LEBT complex and injector with the diagnostics, the focusing elements and the second diagnostic box.

3.3.1 Allison scanner

One of the most important diagnostic is the Allison scanner emittancemeter (EMU). Its working principle is based on the following: a beamlet is selected from the main beam by the entrance slits of the Allison scanner at some coordinate x; then, the beamlet propagates between two metallic parallel plates. At each plate a certain potential is applied. Thus, the beam is deflected depending on the initial x' and the V applied on the plates, following the formula:

$$x' = \frac{VD}{2gV_b} \tag{3.16}$$

where V is the applied voltage between the plates, g is the gap between the plates, D is the effective electric length, and eV_b is the kinetic energy of the beam particle. If the trajectories are deflected enough to enter into the exit slits, the current is collected by a Faraday Cup.

Therefore, at each position x several x' are scanned varying the potential, and for each doublet an intensity I_i is associated.
The result is 2D surface made by triads of (x_i, x'_i, I_i), from which it is possible to estimate the phase space (see Fig. 2.1 for an example of measured phase space). The analysis of such data will be discussed in the next Chapter.

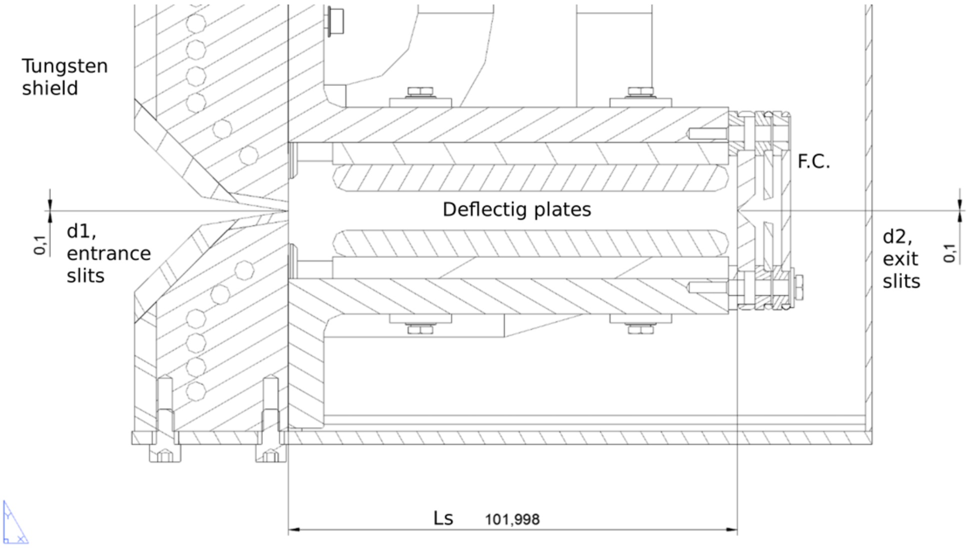

Fig. 3.13 Sketch of the IFMIF/EVEDA EMU. The entrance and exit slit apertures are written (d_1 and d_2). All the values are in mm

3.3.2 Allison scanner measurement error estimate

The error on the emittance measurements made by the Allison scanner can be divided:

- analysis errors
- hardware errors

The total contribution on the error follows Eq. 3.17:

$$\sigma_{err} = \sqrt{\sigma_{an}^2 + \sigma_{hw}^2} \tag{3.17}$$

The analysis errors σ_{an} depend on the post analysis process of the output. In particular, it relies on the routine which interferes the emittance from the background. Their contribution will be discussed in Chapter 4.
Four possible error sources were identified. The discussion of the most significants are reported.

Thermal effects to power deposition

As anticipated by the previous chapters, the power deposition of such large current ion beams may have not negligible effect even at low energy. As far as the emittancemeter is concerned, the beam power which ranges from 13.5 to 3.5 kW at 100% *D.C.* can deform the entrance slits, leading to emittance over-estimation.

In order to estimate this effect, several thermo-mechanical simulations were done with different D.C. and beam input sizes. The software used is COMSOL. The beam impacting onto the emittancemeter is a Gaussian-spatially distributed D^+ beam of 130 mA and 100 keV. The σ of the distribution was estimated from a self-consistent beam dynamics simulation done with WARP. The geometry of the emittancemeter and the surface power deposition is shown in Fig. 3.14. A cylindrical aperture drift was added in order to allow the heat transfer via irradiation when the temperature on the slits reaches over 500° C.

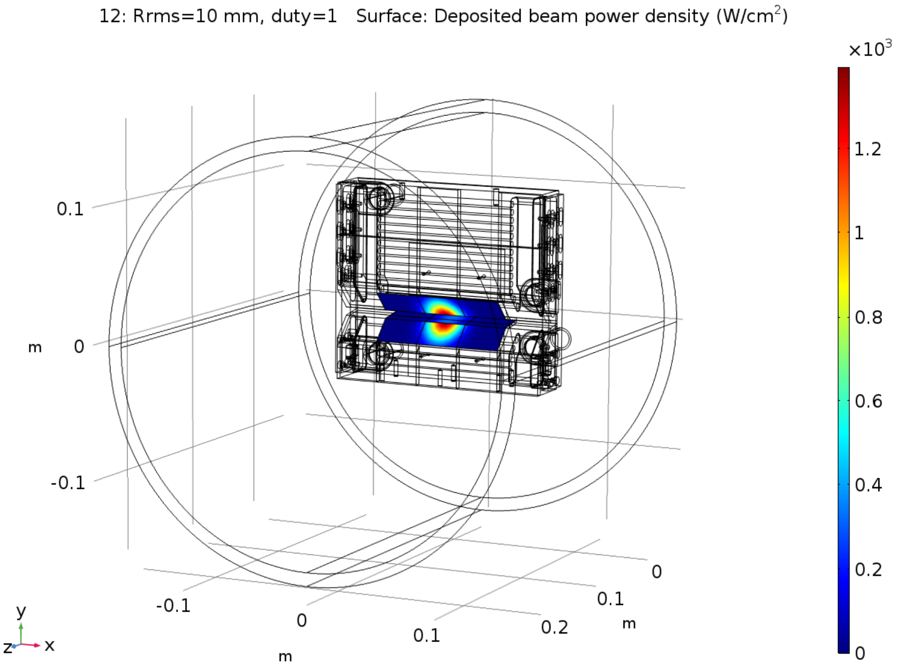

Fig. 3.14 EMU thermal power deposition: surface power density distribution is shown for the case of Gaussian distributed ($\sigma = 10$ mm) d^+ at 100 keV and 130 mA current.

The results of the displacement for various D.C. and beam sizes are shown in Fig.3.15. Above 10% D.C. the slits starts to deform, invalidating the measurement: when the beam intensity is maximum, the central part of the fissure shrinks, thus the current at the F.C. is indeed lower than what should be. As far as the beam intensity is maximum in the center of the distribution, the measured phase-space of that zone receives a lower intensity.

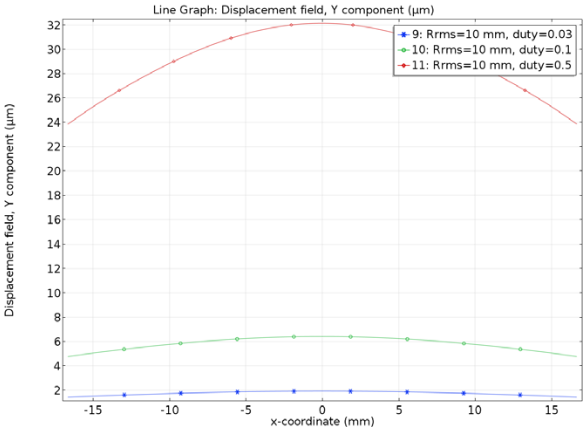

Fig. 3.15 Displacement field of the EMU entrance slits due to power deposition for 3% 10% and 50% D.C. beam of 130 mA.

The ratio between the tales and the center of the beam is drastically modified, with an increase of statistical weight of the external part of the beam. Therefore, the emittance estimation, which is based on the intensity of each zone of phase space, results larger than the reality. This effect is not negligible above 10% (Fig. 3.15). All the measurements and commissioning working points studied in this thesis are below that level.

Finite slit size induced error

The slits width affects the measurement accuracy: increasing the width lowers the emittance measurement resolution, depending on the beam divergence and dimensions (thus on the Twiss parameters). The resulting emittance growth, in case of a Gaussian spatial distributed beam, can be estimated with [26]:

$$\frac{\delta\varepsilon}{\varepsilon}=\left(1-\frac{1}{\varepsilon_m}\left(\beta_m\frac{d_1^2+d_2^2}{12L_s^2}+\frac{1+\alpha_m^2}{\beta_m}\frac{d_1^2}{12}-\alpha_m\frac{d_1^2}{6L_s}\right)+\frac{1}{\varepsilon_m^2}\frac{d_1^2d_2^2}{144L_s^2}\right)^{1/2}-1 \tag{3.18}$$

where $\varepsilon_m, \alpha_m, \beta_m$ are the measured Twiss parameters of the beam, while d_1 and d_2 are the entrance and exit slits, $d_1 = d_2$ which are 0.1 mm. The results can vary from -1.7% to 2% depending on the beam parameters.

Space charge effects

When the residual beam has passed through the slits, it propagates along the emittancemeter gap. Eventually, it may increase its width due to the space charge field. Therefore, the beam at the exit slits can be larger than expected; as a results, the current read at the Faraday Cup may be lower. Thus, it is important to determine if the beam transverse dimension growth at the exit slits, caused by space charge, is negligible or not respect to those one induced by the intrinsic divergence of the beam.

In order to estimate this effect, a flat constant density zero emittance beam is considered. If the beam is Gaussian distributed in space, the deflection of the ions at the beam-boundary can be calculated via [26]:

$$\Delta x = \frac{1}{2}\frac{eE_s}{m_i}\left(\frac{L_s}{\beta \mathrm{c}}\right)^2 \tag{3.19}$$

where L_s is the slit to slit distance, E_s is the self-electric field at surface. The relative increase Δx respect to the aperture slits can give an estimate of the contribution of the space charge. The equation becomes [26]:

$$\frac{2\Delta x}{d1} = \frac{eI_b}{(\beta c)^3 m_i}\frac{1}{4\pi\varepsilon_0}\left(\frac{L_s}{\sigma}\right)^2 \tag{3.20}$$

where I_b is the residual beam current after the front slits and σ is the Gaussian distribution sigma at the emittancemeter. Substituting the variables with the IFMIF/EVEDA deuteron beam of 135 mA beam at 100 keV, $I_b = 1$ mA and $\sigma = 1$ cm from a Tracewin simulation, the grow ratio respect to the aperture slit is 0.13%. Therefore, the space charge induced displacement is small respect the beam x occupancy at the exit slits (i.e. 0.3 mm) and its contribution is negligible.

Random measurement errors

The overall reproducibility of the emittance measurements (when enough stable beam extraction were ensured) was normally within 8% for the rms parameters for the majority of the cases. For few cases the largest differences ranged from 10% for the emittance, to around 15% for Twiss parameters β_x and α_x.

These contributions are the major contributors to the errors from the hardware side. It was decided then to assign an error of 7% to the emittance data, while 10% to the Twiss parameters, in order to be conservative.

3.3.3 Faraday cup

Two Faraday cup are installed in the LEBT system. Their working principle is based on collecting the charges from a charged beam onto an insulated metallic cup, and measuring the current using a calibrated resistor.

$$\Phi_c = \frac{I}{q} \tag{3.21}$$

where Φ_c is the charged particle flux (number of ions per second), I is the measured current and q is the charge. When the beam collides with the cup, it may create secondary electron. This electron can escape the Faraday cup region, leaving in the metal another positive vacancy. The current is therefore artificially increased by the ion and the vacancy. In order to avoid this problem, a negatively biased suppressor ring is placed at the entrance of the cup, in order to send back into the metal the emitted electron. The vacancy is then neutralized and no current overestimation is to be expected.

In IFMIF/EVEDA LEBT, the first FC is placed between the two solenoids and it is biased with a negative potential, to suppress secondary electrons that give an artificial increase of the read current. The second one is the beam stop, situated at the end of the second diagnostic box.

During commissioning, the beam stop shows an underestimation of the beam current due to the secondary electrons emitted from the surroundings. Therefore, in the last two commisioning campaigns, dipole magnets were installed in order to deflected the out-coming electrons.

For phase B, the low power beam dump (LPBD) at the end of the MEBT will be transformed into a Faraday Cup, electrically insulating the structure and adding a repeller electrode at the exit of the LPBD. The 5 MeV D beam will collide onto the surface of the low power beam dump, generating secondary electrons. In order to check the potential needed on the repeller, WARP[17] simulation with POSINST module was used; the results shows that a voltage of -5 kV is enough to stop the out-coming electrons.

Measurement errors

The experimental error on the measured current is composed of two contributions:

- noise: given by the read-back system and the beam instabilities. The current oscillates of about ±1 mA

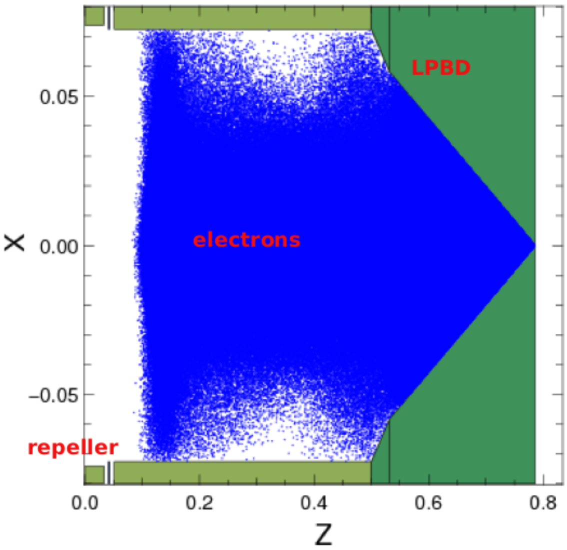

Fig. 3.16 Steady state regime of simulation of secondary electrons generated by the collisions of 5 MeV deuteron beam energy onto low power beam dump. The electron are colored in blue

- secondary electrons: when the BS does not intercept all the beam, some particles collide with the end of the diagnostic chamber. Back streaming electrons can be then emitted. If these secondary electrons are absorbed by the BS, they cause an underestimation of the current [27]. From previous measurements, the difference on the current was about 11% of the current transmitted. As a safety margin, it was decided to add this uncertainty contribution for any transmission lower than 85%.

3.3.4 Doppler shift spectrometer

The Doppler shift species portion measurement is a technique based on the Doppler effect, which allows to determine the species fraction in a non destructive manner.

As an example in the proton case, the H^+ are extracted with some contaminants from the ion source: the H^+ beam and its contaminants (H_2^+, H_3^+) interact with the residual gas in the beam pipe, in such a way that they undergo dissociative charge-exchange collisions with the residual gas molecules, emitting photons. Neutral hydrogen atoms with three different energies are formed: the energy of these atoms are, for the above case, eV_{ext}, $eV_{ext}/2$ and $eV_{ext}/3$ (V_{ext} is the ion source potential). Therefore, the emitted wavelength will depend on the neutral ion velocity in such a way that, observing the beam direction with a certain angle θ, the shifted wavelength becomes:

$$\lambda = \lambda_0(1 - \beta cos(\theta)) \tag{3.22}$$

where λ_0 is the unshifted wavelength and θ is the angle between the viewing line of sight and the beam direction of propagation. Therefore, the contaminant ratio is determined from the light intensity (analyzed by a monochromator) associated with each Doppler-shifted line. In the IFMIF/EVEDA LEBT, the Doppler Shift Spectrometer is placed between the two solenoids, in the first diagnostic box.

3.3.5 The Four Grid Analyser

The aim of the four grid analyzer is to evaluate the beam neutralization by measuring the the residual gas ions or electron kinetic energy. The ions and electrons belong to the secondary plasma generated by intense ion beams due to ionization processes. Thus, their energy are related to the beam residual potential (the beam potential which has been reduced by the electrons contributions); therefore, an estimate of their energy gives an estimate of the residual self-field potential.
In order to do so, the FGA is generally composed by 4 grids placed at specific potential:

1. the first grid defines the ground equipotential.
2. the second grid is set to some potential in order to accelerate or reject the ion or the electrons, depending on which species the study is set.
3. the third grid is the analyzer grid: the potential is scanned within the energy range the user wants to study; depending on the kinetic energy, the residual gas ions which arrive on the grid will pass through or will be rejected. The percentage of ions/electron that passes through the grid and reaches the FC, gives the signal of the FGA related to the 3^{th} grid potential. The reading (V_3, I), in first approximation, is the cumulative function of the secondary plasma energy distribution.
4. the last grid is the electron repeller suppressor of the final Faraday cup collector

For the above considerations, the current collected by the FGA obeys the following equation:

$$I(\Phi) = \int_{\Phi}^{\infty} f(u)du \tag{3.23}$$

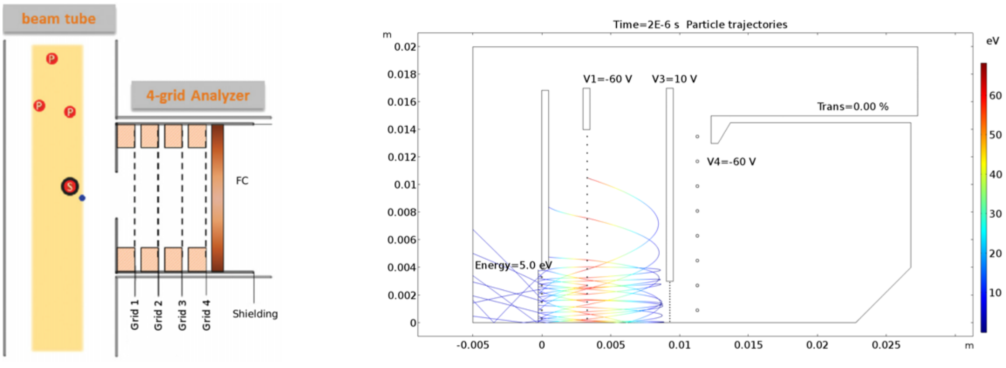

(a) (b)

Fig. 3.17 (a) FGA sketch: the position respect to the beam pipe is shown [28] (b) FGA example with 5 eV particles and 3^{rd} scanning grid voltage of 15 V

where f is the energy distribution of the residual gas ions/electrons. In order to calculate this integral, a possible choice is to consider the ions from the residual gas to have a Maxwellian distribution in velocity. In first approximation an ion reaches the FGA with a velocity equal to $v^2 = v_i^2 + 2eV_p/m_i$, where v is the final velocity, v_i is the initial velocity, V_p is the residual plasma potential and m_i is the ion mass. The contribution to be analyzed is given by the plasma potential, which contains indeed the information on the space charge compensation. v_p can be expressed as $v_p^2 = 2eV_p/m_i = v^2 - v_i^2$. Substituting v_p into the Maxwell distribution equation, the formula becomes:

$$f(v) = 4\pi \left(-\frac{m_i}{2\pi k_B T_i} \right)^{3/2} e^{\frac{m_i(v^2-v_i^2)}{2k_B T_i}} (v^2 - v_i^2) \tag{3.24}$$

where T_i is the ion temperature and, k_B is the Boltzmann constant. Considering that $v_p^2 eV$, the Maxwell distribution can be expressed in terms of energies. Taking into account that the energy selection made by the FGA is done with V_3 (3^{rd} grid potential), the expression becomes:

$$f(V_3) = \frac{4}{\sqrt{\pi}} \left(\frac{m_i}{kT_i} \right)^{1/2} e^{-\frac{eV_3 - eV_i}{kT_i}} \frac{eV_3 - eV_i}{kT_i} \tag{3.25}$$

The cumulative distribution function of the 3.25 can be expressed as:

$$I_{fga}(V_3) \propto erf\left(\frac{V_3 - V_i}{\Delta}\right) - \frac{\sqrt{\frac{V_3-V_i}{\Delta}}e^{-\frac{V_3-V_i}{\Delta}}}{\Delta} \tag{3.26}$$

where Δ is a factor proportional to kT_i and the σ of the distribution, and contains all the information on the space charge residual potential hole.

Deviation from theoretical treatise

The condition $E_p > eV_3$ (E_p is the particle kinetic energy) for a particle to pass through the 3^{rd} grid and to be collected by FC is necessary but not sufficient. As an example, if a particle with an energy higher than the selecting grid gains a transverse component in velocity (i.e. orthogonal the FGA axis) due the previous grids (which act as focusing/defocussing lens), it may be deviated in such a way to collide against the metal part of the detector. As a consequence, its charge is not collected by the FC. The same situation may not occur with a different ion energy (provided the kinetic energy is still higher than 3^{rd} grid voltage), due to the different focusing/defocusing effect of the grid.

Therefore, there is a dependence of the transmission function (through the 3^{rd}) respect to the velocity components of the ions ($v_\perp$ and $v_{||}$) which can bias the measurement.

Another source of uncertainty refers to the potential drop between each wire of the 3^{rd} grid: it determines the resolution of the system. Indeed, if a particle with 14 eV passes right in the center between two wires, where the potential drop brings the value from 14 V (value applied on the grid) to 13 V, the particle will pass the grid, generating spurious signal. The system has a resolution worse than 1 eV.

Therefore, the output signal of the FGA is not the simple CDF of the Maxwellian distribution, but it is a convolution of the response function (which takes into account all the above considerations) and of the CDF. Therefore, if the CDF of the Maxwellian distribution is chosen as a fit of the FGA signal, it may encounter difficulties in the fitting at the beginning and the end of the V_3 interval values. This uncertainty was added to the estimate.

Other sources of errors may came from the voltage amplifier stability: these errors are taken into account when deriving the fitting parameters.

3.4 The RFQ

The RFQ is a linear accelerator which focuses, bunches and accelerates a continuous beam (coming from the ion source).

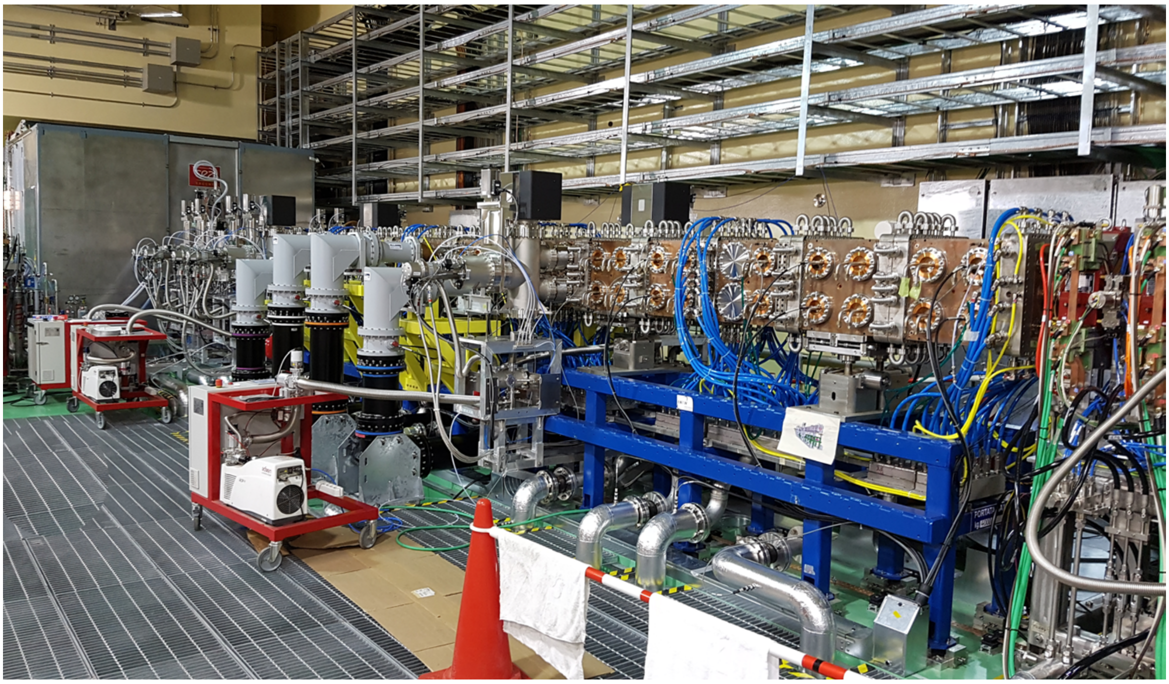

Fig. 3.18 RFQ installed at LIPAc facility

The transverse focalization strength is managed by the apertures of the electrodes (a is the minimum distance while ma is the maximum distance from axis of the electrodes, see Fig.3.19 and R_0 is the average radius). Eq. 3.27 shows the focusing factor B_{foc}, which depends on the electrode apertures, the vane potential V and the electrode geometry.

$$B_{foc} = \frac{qV}{c^2 M} \frac{\lambda^2}{R_0^2} \tag{3.27}$$

where M is the ion mass (here called M instead of m in order to avoid confusion with the modulation factor m). The bunching and accelerating effect, given by the E_z component of the electric field, is obtained by a longitudinal modulation of the quadrupole electrodes. An example of 3d view of the RFQ electrodes can be see in Fig. 3.19. The modulation is given by the parameter m (modulation factor).

The RFQ is particularly suited for low energy beams, due to the fact that the transverse focusing system is supplied by the electric field, which is the most convenient way (in terms of focusing strength) to manage low velocity particles.

In order to ensure the synchronization between the particles and the cavity RF field, it is necessary to set the spatial period of longitudinal fields equal to $\beta\lambda$, λ being the wavelength of the RF field. Only the particle with given velocity is synchronous, at the beginning of the

RFQ, or given electrostatic pre-acceleration, only a given A/q ratio will be accelerator. As an example, for the IFMIF/EVEDA case, this property forces to choose the energy of the proton beam as 50 keV instead of 100 keV, in order to be synchronous.

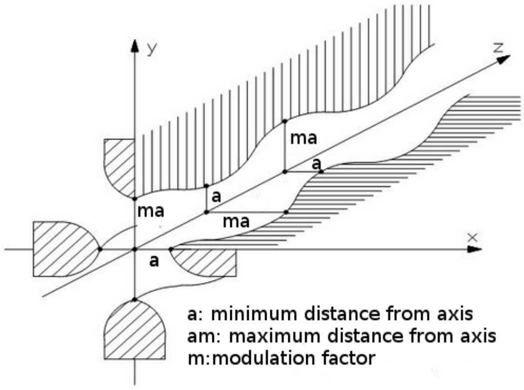

Fig. 3.19 3d view of the RFQ electrodes

Another effect of the periodicity of the longitudinal forces is that the bunching effect can be done adiabatically over several cells (the cell length is $\beta\lambda/2$). This is the reason why the RFQ structure maximizes the longitudinal capture ($> 90\%$) and minimize the emittance growth: the phase spaces of the beam are indeed not subjected to strong solicitations, the longitudinal kick is distributed along many cell, applying many longitudinal weaker forces at each chosen cell. Therefore the preservation of the beam quality is ensured.

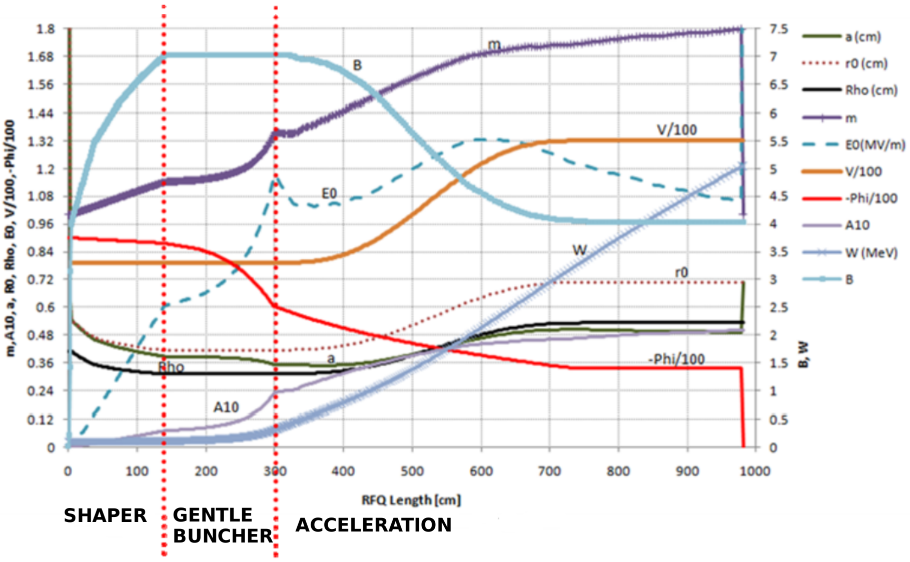

Fig. 3.20 RFQ parameters with the shaper, gentle buncher and accelerating section reported.

From the design point of view, the RFQ is divided in three sections: the shaper, the gentle buncher and the accelerating section. The shaper prepares the beam for being bunched, starting the modulation. In this section, the synchronous phase falls within -90^o -80^o (for IFMIF-EVEDA RFQ). Then, the gentle buncher section bunches the beam, with a minimum phase of about -60^o (for IFMIF-EVEDA RFQ). When the gentle buncher ends, the acceleration starts and continues up to the end. The IFMIF-EVEDA RFQ design method ensures the optimization of the voltage and R_0 (average radius defined as $(ma+a)/2$) law along the RFQ, and the enlargement of the acceptance in the final part of the structure. As it can be seen from Fig. 3.21 plot (b), the power density is increasing at the end of the RFQ, due to the accelerated particles. The smaller aperture at the beginning ensures a safe design, since the particle are mainly lost in that zone with a smaller energy instead to the end section, with higher energy.

The resulting design parameters are shown in Fig. 3.20 and refers to 125 mA matched (see Chapter 2) deuteron beam of $\varepsilon_{rms,n,x} = 0.25$ mm mrad at 100 keV. The Table 3.1 shows RFQ design parameters:

Table 3.1 RFQ main parameters

Parameter	Value
Length	9.814 m, (5.7 λ)
Total Cell number	489
Voltage Min/Max	$79.29/132$ kV
Max modulation m	1.799
Min aperture a	3.476 mm
R_0 min/max	$5.476/7.102$ mm
Ratio ρ/R_0 x,y,z	0.75 constant
Final Synchronous phase	-33.5^o
Total RF power + Beam power	1.6 MW
Transmission (Gaussian)	93.7%
$\varepsilon_{rms,l}$	0.2 MeV deg
$\varepsilon_{rms,n,x}$	0.25 mm mrad
Nominal beam power loss (Gaussian)	1291 W
Max surface field (1.76 Kp)	24.7 MV

3.4.1 RFQ input requirements

At the entrance of the RFQ, the converging beam changes from a time independent solenoid focusing (in IFMIF/EVEDA case the beam is coasting) to a time dependent FODO. Moreover, compared to the solenoid channel, the RFQ FODO focusing channel is much stronger. The

radial matching section of the RFQ (placed at the very begin of the RFQ) provides a transition zone where the beam from time-independent structure becomes time-dependent, adapting from the solenoid to RFQ focusing channel: in order to do so, the B_{foc} is increased adiabatically, starting from very small value at the RFQ input.
It is possible to find the input parameters of the beam (given by the Courant-Snyder parameters) which ensure the periodic trend of the beam envelope, avoiding uncontrolled excursions of the beam. This procedure minimizes the losses due to uncontrolled growth of the beam envelope, which makes some part of the beam to collide with the rfq electrodes. If this condition is not satisfied, the beam is said to be mismatched respect to the focusing channel and it is possible to assign a mismatch factor defined in Chapter 2.
Moreover, when the beam has a not negligible space-charge field, any small mismatch may excite the instabilities such as envelopes and kinetic alike, or even higher order modes. This problem increases the probability of beam losses along the accelerator.
Therefore, it is very important to ensure beam matching. The Courant-Snyder parameters needed for the input beam in order to ensure the matching are listed table 3.2.

Table 3.2 RFQ Twiss

Parameter	Value
α_x	1.3
β_x	0.109 mm/mrad
a	1.63 mm
a'	24.36 mrad

These input beam conditions need to be supplied by the LEBT solenoids: the smaller and convergent beam is needed, the more challenging will be the LEBT tuning in case of space charge dominated beam. Moreover the matching itself from the LEBT is intrinsically difficult due to several factors: transition from the space-charge compensated regime to the space-charge beam; the not equilibrium state of the distribution at the entrance of the RFQ. Despite the new low B design of the IFMIF/EVEDA rfq requires less focused beam at entrance [23], this is still one of the most challenging aspect from the LEBT point of view; three conditions need to be satisfied at the same time: matching (see table 3.2), emittance rms normalized below 0.3 mm mrad and the nominal intensity 135 mA deuteron beam. As it will be shown in Chapter 5, these values are strictly correlated to the injector beam output, and therefore, it is not always possible to ensure all requirements at the same time.
The beam behavior in case of 0.3 mm mrad normalized rms emittance, matched beam Gaussian distributed is shown in Fig. 3.21. The RFQ is not the ideal one, but contains the

information of built errors and real tuned voltage profile. The transmission is 92%, while in the case of the 0.25 mm mrad design emittance, it is 94.4

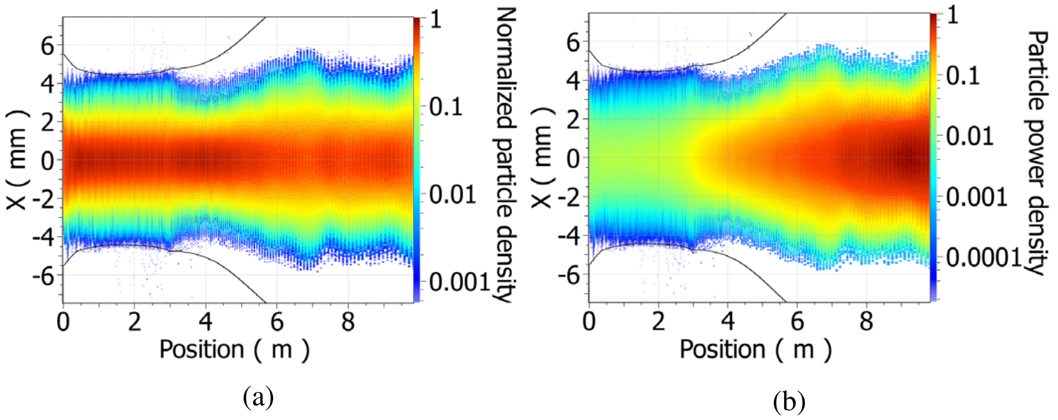

(a) (b)

Fig. 3.21 x (a) and power (b) densities respect to axis of the as built RFQ. The beam is gaussian distributed, the input emittance is 0.3 mm mrad and the Twiss parameteres are the matched ones

3.5 The MEBT and HEBT

The MEBT and HEBT are transfer lines composed by several quadruples and bunchers. As far as the MEBT is concerned its role is to match the beam longitudinally and transversally from the RFQ onto the SRF cavities. Due to the relative large perverance of the beam at 5 MeV, the MEBT is as much short as possible, in order to avoid space-charge induced halo on the beam. For the same reason the focusing period is smaller than in the HEBT.

After the SRF, the HEBT takes in charge to deliver the 9 MeV beam, up to the power beam dump. There are no bunchers, the transverse focusing system is composed of 2 triplets and one doublet. Before the last triplet, a magnetic dipole depletes the residual contaminants which may come from the source. Due to the higher energy of the beam (thus the lower perveance), the focusing period is larger than the MEBT. This design characteristics will be a key point if a commissioning of the RFQ without the SRF cavities is planned.

3.6 Commissioning phases

The complexity of this accelerator and of the beam physics underlying requires a careful commissioning of each part of the machine [29]. In order to do that, 3 phases have been identified, corresponding to the three energy sections of the accelerator: low energy ($\beta =$

0.0103) which involves the injector, medium energy ($\beta = 0.0729$) which involves the RFQ and the MEBT and the high energy section ($\beta = 0.0976$), composed by the HEBT and the high power beam dump.
Many reasons justify this subdivision: any interface between the accelerator sections can be considered a strong perturbation on the beam dynamics; as a consequence, it changes the beam stability status which may cause possible losses; an excellent example is the interface between the LEBT and the RFQ, where, from the transverse point of view, the beam is transiting from a smooth focusing channel of the solenoids to the strong focusing channel, alternating gradient type of the RFQ. Moreover, from longitudinal point of view, the beam is being accelerated and bunched from its previous coasting state.
Therefore, the complete study of the beam behavior at the interfaces are essential for minimizing such perturbations.
Another important point comes form the maintenance and machine protection point of view: the average power deposition P$_{av}$ of the beam is directly proportional to the kinetic energy, the number of particle per second I/e and the duty cycle (D.C.) of the accelerator Eq. 3.3:

$$P_{av} = K_{beam}\frac{I}{e}D.C. \tag{3.28}$$

where I is the average current per bunch. As the energy increases, so does the average beam power. Therefore, higher energy sections can have larger risks for the machine integrity in case of losses. It is worth to mention that at the beam final energy 9 MeV, nuclear reactions may happen due to the collisions of the beam with the accelerator parts: as the beam energy increases, more nuclear channels open, leading to possible activation of the line.
In conclusion, besides the obvious recommendation to avoid losses, the subdivision in such phases allows to manage the different working backgrounds in the most efficient way from safety and maintenance point of view.

3.6.1 Phase A

The injector is tested in order to find the optimal source and LEBT tuning for injecting the beam into the RFQ. This phase is also very useful in order to benchmark the simulation models to the experimental data. Within this phase, several other sub-phases were performed. The commissioning phases are not presented, in this list, in chronological order, but in a logical order.

Phase A3

The phase A3 consists of the source and extraction column test. As shown in Fig. 3.22 the line consists in the source and one diagnostic box attached together. There are no focusing elements but the extraction column. The available diagnostics are: the emittancemeter, the F.C., the beam profile monitor and the Doppler shift spectrometer. In this way it is possible to characterize the extraction column directly, without the influence of the solenoids. However it is important to notice that the effect of the emittancemeter on the neutralization is not negligible as it will be demonstrated, and influences significantly the neutralization ratio, thus the output beam quality. The possibility of injecting Kr gas in the line is foreseen, in order to change the space-charge compensation in the line.

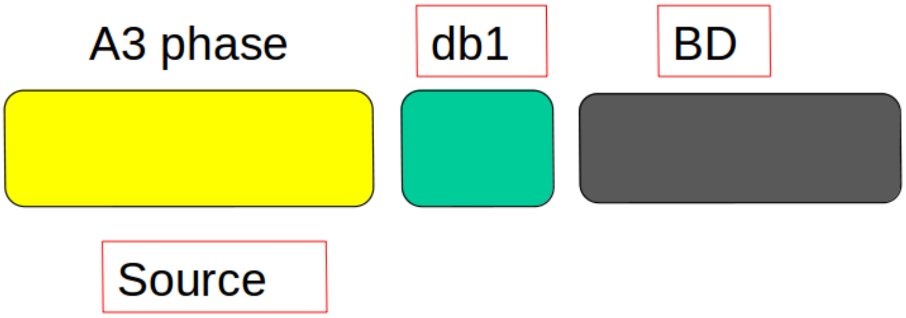

Fig. 3.22 Sketch of the phase A3. db1 is the diagnostic box.

Phase A1

The phase A1 consists of the insertion of one solenoid lens between the source and the emittancemeter. In this phase, it is possible to observe the emittance increase due to the combination effect of the non linearities of the solenoid (if any) and the not perfect compensation of the space-charge field. It is important to notice that this emittance growth depends on the the beam envelope and thus on the solenoid value. As it will be shown in Chapter 5, this phenomenon creates restrictions on the matching degree of freedom of the LEBT.

From the commissioning point of view, it is possible to pick up the phase-space plane of the beam at the emittancemeter position and to extrapolate with the simulation model the solenoid lens values for injecting the beam into the RFQ. The available diagnostics are the same of the Phase A3. A gas injection is foreseen between the two solenoids, in order to improve the space charge compensation.

Phase A2

Now all the line is assembled: the source is connected to the whole LEBT, which includes the solenoids, and the injector cone. In order to study the beam characteristics after the cone (transmission, emittance and current) in function of the injector parameter tunings such as the solenoid values, a second diagnostic box is inserted after the cone.

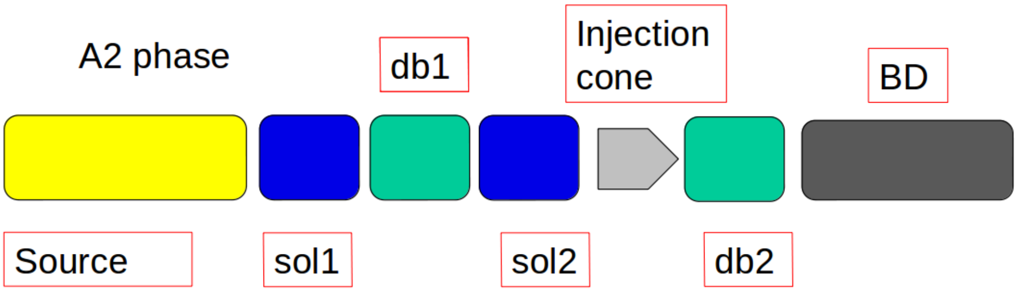

Fig. 3.23 Sketch of the phase A2. db2 is the second diagnostic box.

In the second diagnostic box the emittancemeter and a beam stop are placed, in order to evaluate the current and the emittance after the cone. In the first diagnostic box (placed between the two solenoids) the F.C., the Doppler Shift Spectrometer and the Four Grid Analyzer are implemented. As in the other phases, there is the possibility to inject an external gas species in order to improve the neutralization in the two diagnostic boxes. The main difficulty of this phase is to evaluate the compensation process in the second diagnostic box, since the effects of the emittancemeter and of the better vacuum (one order of magnitude less respect to the other parts) need to be taken into account; otherwise overestimation of the emittance may occur.

3.6.2 Phase B

In this phase the performances of the RFQ and MEBT are evaluated. Once a working tuning on the injector is found, it is possible to attach the RFQ, the MEBT and a suited beam dump in order to continue the commissioning.

Phase B0

Due to the considerably high value of beam power (625 kW), calculated from Eq.3.1 in the case of 125 mA of deuteron beam at the RFQ output, the beam pulse will be reduced down to 100 of μs with a D.C. not larger than 0.1%. For this phase, a temporary specific power beam dump was designed [30] which can sustain up to 1 ms and 1 Hz beam pulsed operation, which is called Low Power Beam Dump (LPBD). In this thesis it was estimated the evolution of the beam parameters at RFQ input due to the space-charge compensation transient

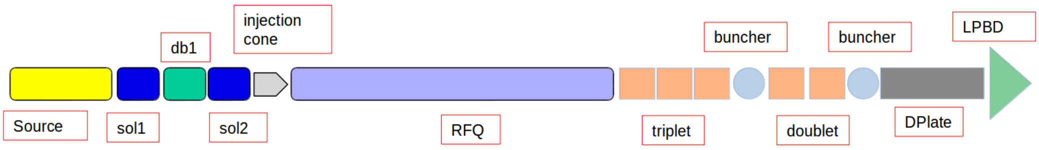

Fig. 3.24 Sketch of the phase B0

As far as the implemented diagnostics, there will be a whole section called diagnostic plate which includes several instrumentations, as reported in [31]: DCCT and ACCT for current measurements; the beam centroid will be controlled via four-stripline monitors. As far as the beam profile is concerned, two types of non-interceptive diagnostics are implemented; one type works with the residual gas ionization, the other one works with the photons of the residual gas excitation molecules. These monitors, in combination with the longitudinal and transverse focusing elements, will give also an estimation of the emittance of the accelerated beam.

Phase B1-CW

One of the fundamental aspect of the operation of this RFQ is the CW operation. In order to test such regime, it is required to substain more than 1 ms pulse at 5 MeV and 125 mA current. Only the high power beam dump can stand such power deposition. In the original commissioning plan, the CW steady state evaluation is foreseen after the installation of the SRF-cavities and the HEBT line in order to reach the beam dump. However, it is not worth to anticipate this study before installing the SRF cavities. In this thesis, the study of the possible line configurations which can transport efficiently the beam from the RFQ to the power beam dump bypassing the SRF cavities is presented. The line layout is presented and studied in Chapter 7.

Chapter 4

The SCUBBEx-ghostbuster

4.1 Problems of beam emittance measurement

The emittance estimate is one of the most important measurement performed during the LIPAc commissioning.

As it was seen before, the 6D emittance is, if the system is Liouvillian, conserved along particle orbit. However, it is very difficult to measure experimentally the whole 6D emittance due to the fact that there are not only the so called diagonal planes (i.e. $\{x, x'\}$) but also the so called off-diagonal planes, like $\{y, x'\}$, at the same axial coordinate. All these planes need to be measured at the same position.

Therefore, it is easier to measure the projection of the 6D phase space in the transverse and longitudinal phase space: in particular, the root mean squared emittance formula allows to have an estimate of the 2D emittance from the measurement.

More stricter conditions are needed in order to ensure that the 2D rms emittance is an invariant of the motion: the applied and self forces must be linear and the equation of motions (x and y) must be decoupled (this is not verified within a solenoid field). For example, if the space-charge field introduces non linear forces, the ellipse-like phase space of the beam starts to deform; as a consequence, the rms emittances measured at different s positions have different values (generally larger) than the starting rms emittance value.

From the experimental point of view, different emittance at different points indicates an emittance evolution. Indeed, the rms emittance gives a direct measurement of the quality of the beam; in this way it is possible to verify if the LIPAc requirements are met; as the simulation and modeling part is concerned, it supplies an essential input and benchmark test. Therefore, for all the above reasons it is important to estimate this quantity correctly. The measurements presented in this thesis were taken with the Allison scanner (positioned in the

LEBT, in different points) which scans the 2D phase plane via the mechanism explained in Chapter 3.

The output of this detector are couple of (xx'). Each couple is associated with its current intensity collected. An example can be seen in 4.1.

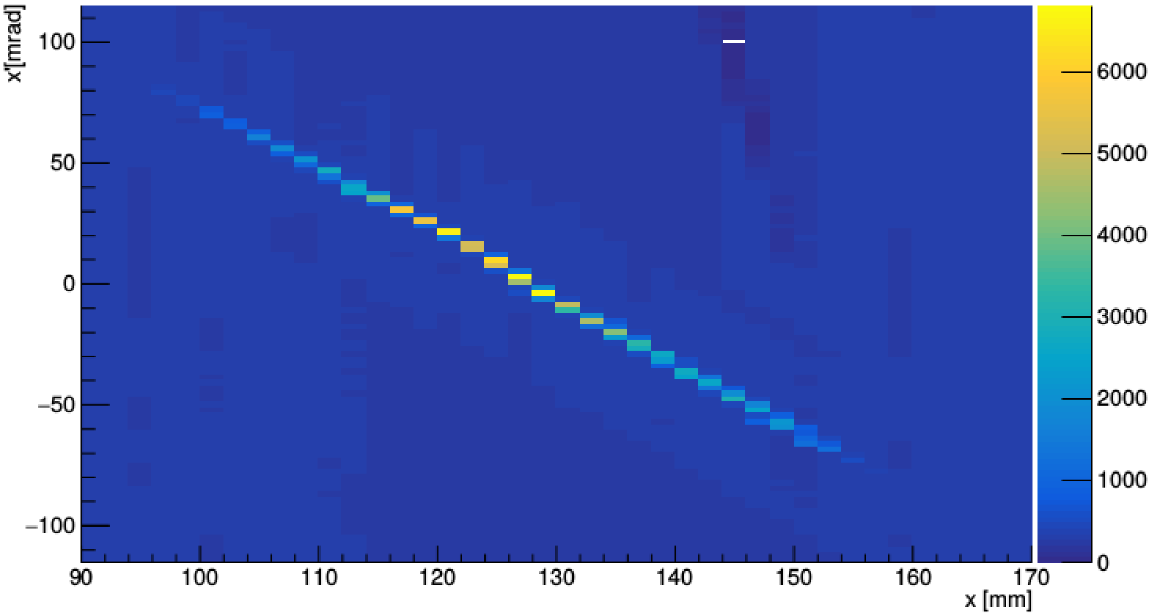

Fig. 4.1 Output signal of the Allison scanner measurement. The signal which is significant for the emittance measurement is the yellow ellipse in the middle of the plane.

Such kind of devices may be affected by several issues:

- particle which does not follow the nominal trajectory defined by the electric field of the plate.
- electronic noise
- different beam species
- the main beam is a 135 mA at 100 kV, which led to a total power at 100% DC of 13 kW. The power deposition on the tungsten shield of the Allison scanner due to the beam collision is not negligible and can cause a deformation of the selection slits with over/down estimation of the beam tales, as shown in Chapter 3.

The net effect of these phenomena is that not all the signal belongs to the real beam emittance: as a matter of fact (see Fig.4.1), there are several "artifact" that surrounded the beam signal. In order to look at their effect it is needed to define the rms quantities on which the emittance rms is based, in the experimental framework. As it was written in Chapter 2, it is possible to associate the spread of the distribution on this phase space to a single value, based on the root-mean square formula 2.8. Experimentally, all quantities are averaged over the intensity c measured by the Allison Faraday cup, such as:

$$\langle x \rangle = \frac{\sum_{i=1}^{N} x_i c(x_i, x'_i)}{\sum_{i=1}^{N} c(x_i, x'_i)} \tag{4.1}$$

This weight average is done for each set of (x_i, x'_i, I_i), where $I_i = c(x_i, x'_i)$; if there are some artifacts, it is possible to see from the equation 4.1, how they can modify the second order moments, giving a biased reading of emittance. Their contribution can be identified as the sum of the three terms. Considering Eq. 4.1, for the sake of simplicity:

$$\langle x \rangle = \langle x \rangle_{\text{sign}} + \langle x \rangle_{\text{backg}} + \langle x \rangle_{\text{art}} \tag{4.2}$$

Therefore it is crucial to find a way to manage the output signal correctly, clearing the contribution from the background and the artifact. Similarly, the Twiss parameters can be affected by the same issue:

$$\alpha_x = -\frac{\langle xx' \rangle}{\varepsilon_{rms,x}}, \qquad \beta_x = \frac{\langle x^2 \rangle}{\varepsilon_{rms,x}}, \qquad \gamma_x = \frac{\langle x'^2 \rangle}{\varepsilon_{rms,x}}, \tag{4.3}$$

4.2 Artifact types

The two main artifacts in the output are: the ghost signal and the background noise.

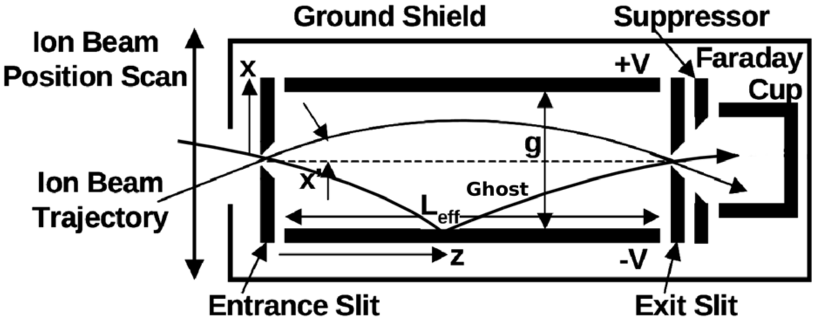

Fig. 4.2 Sketch of the ghost particle trajectory. The particle collides with the lower plate and are re-emitted with a different angle x'

The ghost signal is generated by the collision of the beam particles onto the deflecting plates. If the particle is deflected (instead of being absorbed), the emittance scanner collects a divergence which is the results of $x'_{\text{tot}} = x'_{\text{plate collision}} + x'_{\text{electrical deflection}}$.

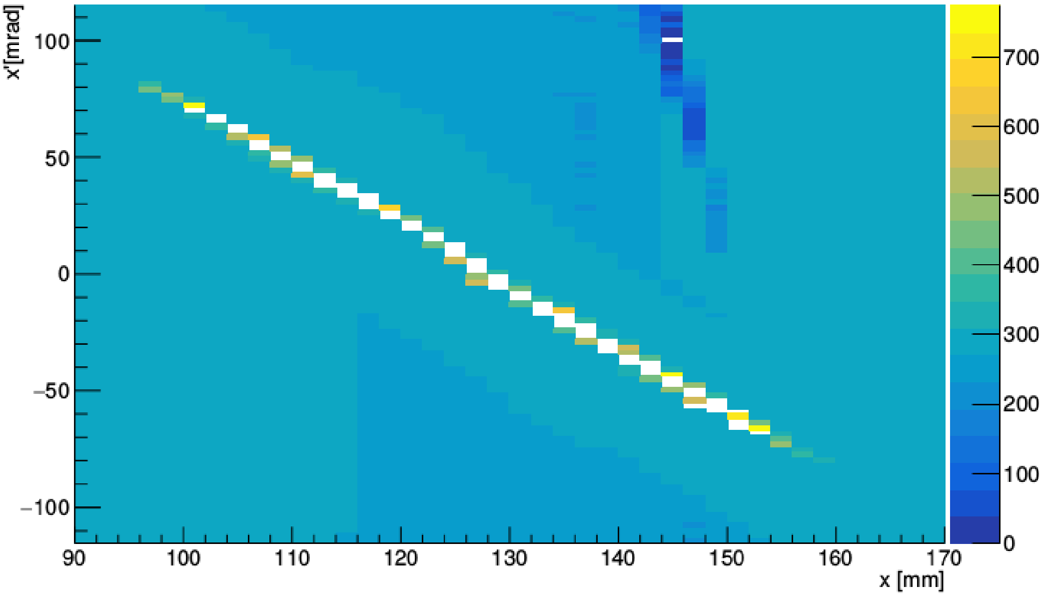

Fig. 4.3 Background output signal of the Allison scanner, taken from Fig. 4.2

The first term is not easily predictable and therefore perturbs the Allison signal. In Fig. 4.3 the nominal signal was reduced in order to enlighten the background. The signals above and behind the emittance (like shadows of the main signal) belongs to the ghosts.

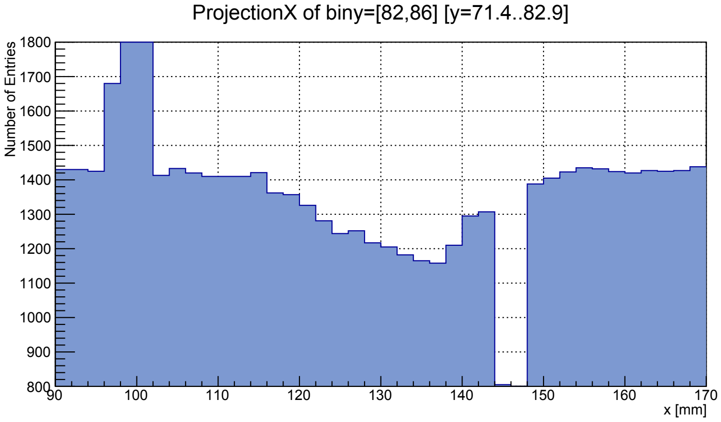

Fig. 4.4 Particular of Fig. 4.3. The signal peak is on the left, while the ghost depression can be clearly identified on the right.

The background noise, generated by the acquisition system causes the presence of the correlated backgrounds. As it was said above, their contribution to the emittance overestimation is not 0. Therefore, they need to be taken into account in order to properly calculate the emittance.

In Fig. 4.4 it is shown an x-projection of the measured phase space plane. The peak on the left is the main beam signal, while the two valleys are the effect of the ghost signal. The small oscillations are the correlated noise. The main bias at 1425 can be also seen.

There are two different ways to manage the ghost signals: from the hardware or via software analysis. For the first one, a possible solution is described in [32]: the main idea is to implement an indented profile for the parallel plates, which re-intercept the ghost trajectory after its deflection, in order to increase the absorption probability, as shown in Fig. 4.5

In the case of IFMIF-EVEDA this solution was not implemented. Therefore, the removal via software is necessary. On the other hand, the electronic noise signal cannot be completely canceled via hardware and therefore needs to be removed via software.

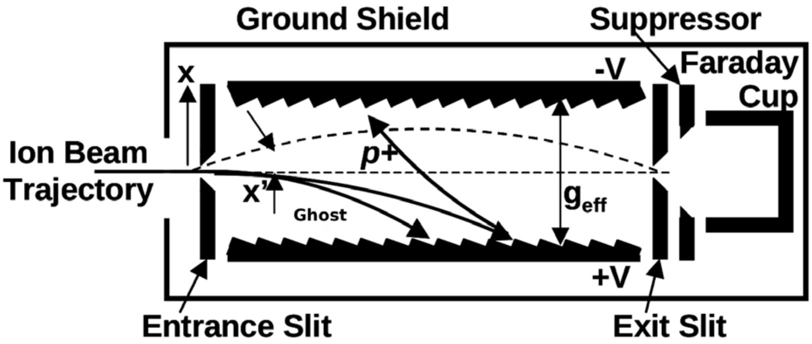

Fig. 4.5 Sketch of the system for the ghost signals. The plates are made with an indent profile which suppresses the probability of a ghost to be collected by the FC.

4.3 The SCUBEEx algorithm

One way to remove the noise signal and infer the emittance was described in reference [33]. It combines two other methods: the threshold and the exclusion ellipse method.

4.3.1 Threshold analysis

The threshold method consists in subtracting to all distribution a certain level of signal. The values above the threshold remain unchanged, while the signals below, which become negatives are set to zero, before calculating the rms emittance. For each threshold the emittance is calculated as soon as for small bias increase the emittance does not change. However, this method shows a strong sensitivity due to even small contributions of positive signal and small bias at large coordinate in the plane (x,x') [33].

4.3.2 Elliptical exclusion analysis

The emittance estimate can be improved by excluding pure background data. The most reliable estimates are obtained when the exclusion boundary surrounds the data tightly without excluding any real signal. Normally, ellipse shape are chosen due to the fact that they are best suited to conform tightly typical emittance data. Due to the fact that some background hides the real signal, it is very difficult to decide the shape and the exclusion ellipse contour. This led to sensitivity to small bias [33]

4.3.3 SCUBEEx

The SCUBBEx (Self-Consistent UnBiased Elliptical Exclusion) analysis combines the two above methods in the following procedure:

1. for each exclusion ellipse, the outer data threshold is calculated, as the average value of the external signal.

2. the threshold is subtracted, with an important difference. The negative values are not set to zero, but they will contribute to the next threshold estimation. In particular, the background fluctuation is not anymore considered "unphysical" respect to the signal of the beam; therefore, its contribution must not be simply put to zero, but integrated (and canceled) through the emittance estimation process.

3. the procedure is iterated, increasing the exclusion ellipse area, until a steady state is reached.

This method provides self consistent bias estimation. Nevertheless, if the emittance data presents some artifacts like ghost, the emittance estimation becomes unreliable [32].

4.4 Effect of the ghost signal on the SCUBEEx.

As it was said in the previous section, the prerequisite of the SCUBEEx routine is to avoid the ghost signal from the emittance data.

Since the IFMIF-EVEDA Allison scanner output does not fit this prerequisite, it is necessary to introduce a pre-routine which reduces these kind of artifacts. Nevertheless if the SCUBEEx routine is used without taking care of the ghosts, the results is not consistent, as shown by Fig. 4.6. The beam $\varepsilon_{rms,n}$ results larger than 1.00 mm mrad (while the measured emittance with other methods results around 0.26 mm mrad), which means that the asymptotic trend is never reached.

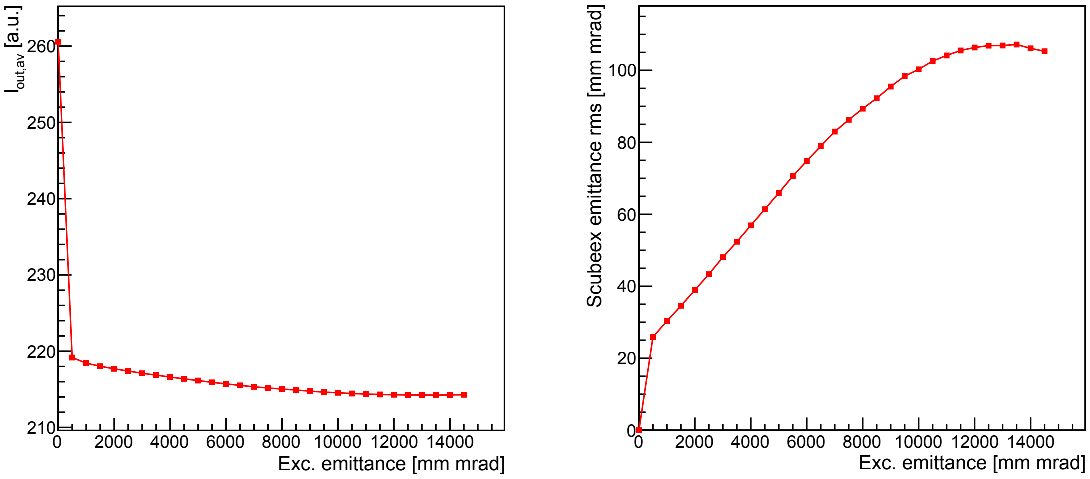

Fig. 4.6 Plots of the current outside the exclusion ellipse (left) and the SCUBEEx emittance vs the exclusion ellipse area (right). It is possible to see that an asymptotic shape is never reached, neither in the emittance calculation nor in the average current.

The ghost signals and similar artifacts give a non-zero contribution to the emittance. Considering Eq. 4.4, when appling the SCUBEEx routine (represented by f function which applies on experiemntal data ensemble $\xi = \{(x_i, x'_i, I_i), i = 1...N\}$), the residual terms are given by the artifact and the signal, while the background is reduced:

$$f(\xi) = \varepsilon_{\text{sign}} + (\varepsilon_{\text{back}} \simeq 0) + \varepsilon_{\text{art}} \tag{4.4}$$

In order to further clean the data another routine is needed to set $\varepsilon_{\text{art}} \simeq 0$

4.5 The ghostbuster routine

The ghostbuster routine aim is to reduce the contribution of the ghost signal, keeping it negligible. Due to the working procedure of the SCUBEEx, it is not possible to simply put their contribution to 0.

This means that the coherent signal of the ghosts must be replaced with an incoherent signal (whose average sum at each step is approximately 0). Many different signals were investigated, such as random Gaussian or the same correlate noise of other part of the measured phase space plot. In the end, it turned out that the uniform noise is the best for this purpose. The procedure of the ghostbuster routine is the following:

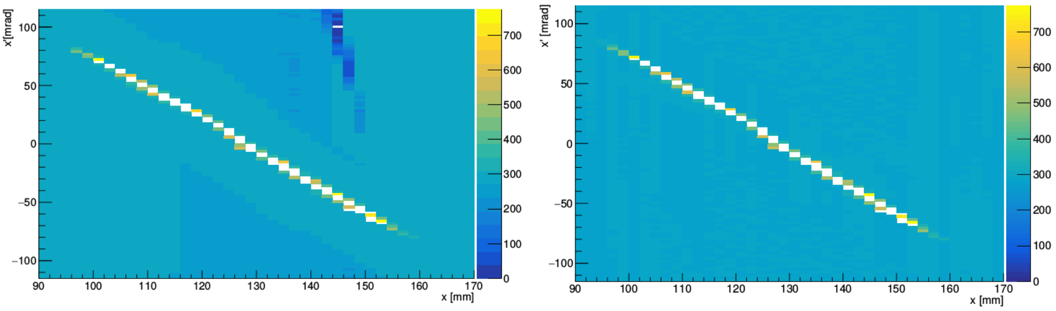

(a) Ghostbuster not applied

(b) Ghostbuster applied

Fig. 4.7 Measured phase plane in case without ghostbuster (a) and with ghostbuster routine (b).

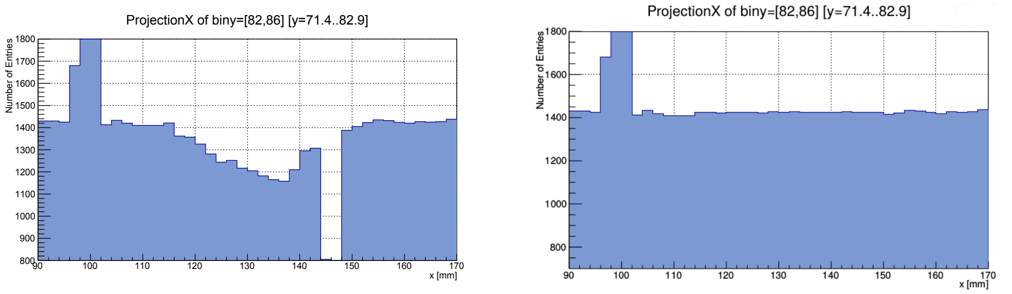

(a) Ghostbuster not applied

(b) Ghostbuster applied

Fig. 4.8 Projection on the measured phase plane in case without ghostbuster (a) and with ghostbuster routine (b).

1. in a zone of the phase space plot free of ghosts and signal, the routine individuates the maximum and minimum oscillations of the correlated background intensity $[I_{\min}, I_{\max}]$.
2. for any couple of points, anywhere in the measured phase plane with $I_i < I_{\min}$, the routine generates a uniform random noise between the $[I_{\min}, I_{\max}]$ values.

The qualitative results can be seen on the Fig. 4.7 and on 4.8. The ghost signals are busted; a uniform noise can be seen at their place. As far as the emittance is concerned, a large difference can be seen. On Fig. 4.9 the two process for emittance estimate (with and without Ghostbuster) trends at each step are compared. The ghostbuster routine allowed to retrieve the asymptotic behavior requested for a self consistent calculation.
The value with the ghostbuster is 0.25 ± 0.01 mm mrad (which is in agreement with other methods), while without is 1.00 mm mrad. There is still a small residual effect due to the ghosts, consisting in small oscillations of the emittance value. However, this effect does not prevent to retrieve the information, but gives the error in the background estimation. From the routine point of view, the oscillations are due to the transitions between the correlated and the uniform background.
In conclusion the routines gives the rms values ($\varepsilon_{\text{rms}}, \alpha_x, \beta_x$) and the associated error from the oscillations ($\Delta\varepsilon_{\text{rms}}, \Delta\alpha, \Delta\beta$)

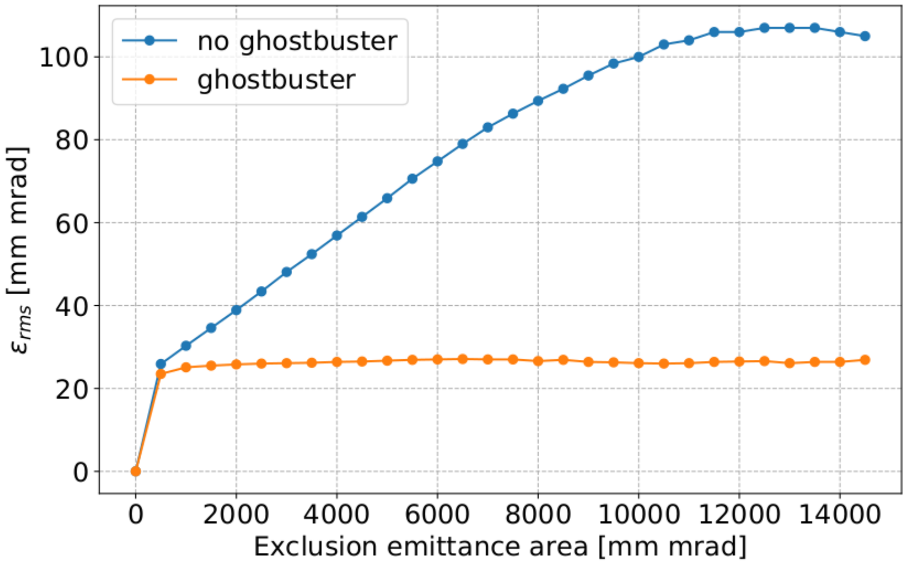

Fig. 4.9 Emittance trends with or without ghostbuster routine. It is possible to see how the blue curve (no ghostbuster) looses quickly the asymptotic value, while the orange one maintains it.

4.6 Benchmark and validation via blind tests and comparison

4.6.1 Blind test

In order to validate this method, it was decided to check the routine via blind test: several type of beam, noise and ghost where generated via software using the simulation program Tracewin [14] and the analysis software ROOT [34]. The procedure used was the following:

1. a beam with high perveance was simulated with Tracewin in a drift with a given emittance and Twiss parameters.
2. a script implemented in ROOT simulates the response function of an Allison scanner, introducing the chosen artifacts. The background could be correlated or uncorrelated, Gaussian or uniform.
3. the result of the script was analyzed by the SCUBEEx-Ghostbuster. If the routine estimates correctly the emittance value, then the test is passed.

An example of reprocessed simulated phase space is shown in Fig. 4.10.

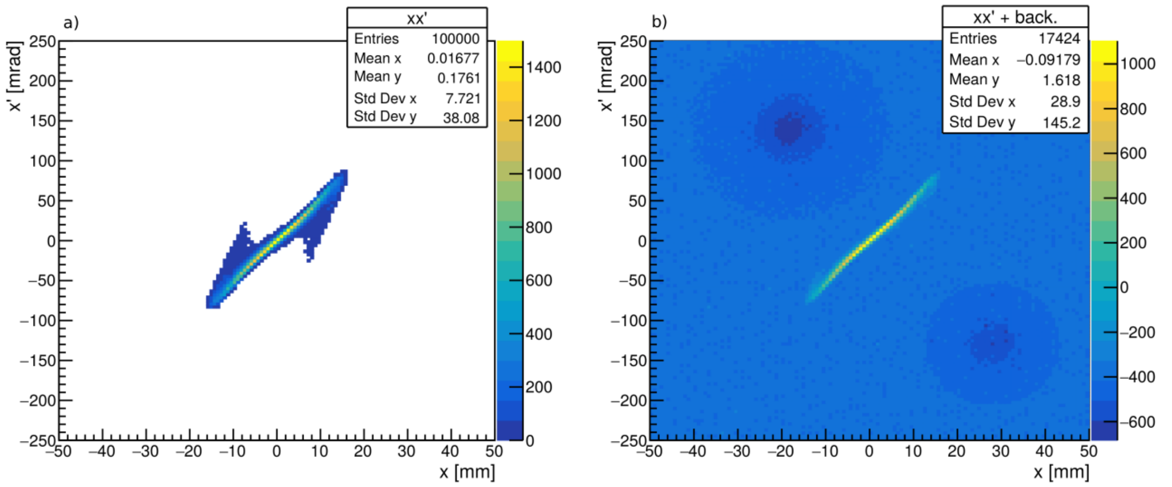

Fig. 4.10 Simulated measured emittance phase plane. **a):** It shows how the phase plane appears without the background. **b):** The background is superimposed to the emittance ellipse, via a ROOT script. First and second order moments are shown for both the plots. There is a large change on their values between the two cases

As it is possible to see, the reported first and second order moments of the distribution change a lot between the two cases.

Table 4.1 Results of the blind tests

Noise type	Ghost	Correlation	Simulated value	S.G. estimate
Uniform	0	no	0.10	0.10 ±0.01
Gaussian	1	yes	0.50	0.49 ±0.03
Gaussian	2	yes	0.50	0.47 ±0.04

The results of the script respect to the different background and the presence of the ghosts are summarized in table 4.1. The script errors became larger when there are superpositions of the ghosts to the beam emittance, as in the last case reported on the table. In this case the error (and thus the oscillations) grows up to 8.5%. However, even in such extreme case, the script succeeds to enclose the real value in the error interval.

4.6.2 Other analysis software

A further validation to the script comes from the CEA developed software [35] used for the LIPAc commissioning. In this case, both softwares contribute with a reciprocal counter check. In Fig. 4.11 it is shown the emittance trend of a deuteron beam of 135 mA at 100 keV, versus different LEBT solenoid strengths, calculated by the Scubeex-ghostbuster and the CEA routine is shown.

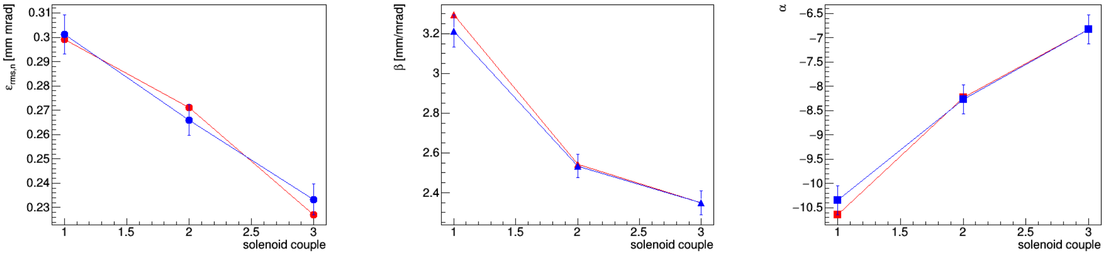

Fig. 4.11 Comparison between the SCUBBEx-ghostbuster and the CEA routine [35]. The abscissa indicates the different solenoid couples at which the emittances were taken. The blu curve is the result from SCUBEEx-ghostbuster, while the red curve belongs to the [35]. The values are in good agreement within the error bars.

The two trends are compatible within the error bars and therefore the post-analysis of the emittance scanner output is reliable. The point 1 has the larger difference between the two routines: this is due to the larger deformation of the beam distribution resulted from the optical transport of the beam through the solenoid channel. The phase space distortions due to solenoid non-linearities have low intensity, mixed with the background; therefore, point 1 (which is more affected by such distortions) is more sensitive to the different background evaluation of the two routines.

4.7 Limitations

The SCUBEEx-ghostbuster has some limitations on its validity; one of them was already discussed in Sec. 4.6. The other two are listed below:

- the routine cannot exclude the contribution of different species (if any) with a signal superimposed to the main beam. This makes it suitable for the emittance measurement in phase A3 and A2 (see 3.6), but not in phase A1 (i.e. when the other species are superimposed with the beam emittance and tilted due to the solenoid 1 lens)
- the routine retrieves the second order moments of the beam distribution. However, it does not supply the clean beam signal, clearing out the background. As an example, it is not possible to get the profile x or x' of the beam from the output. Therefore, another routine was developed for such purpose,

4.8 Profile routine

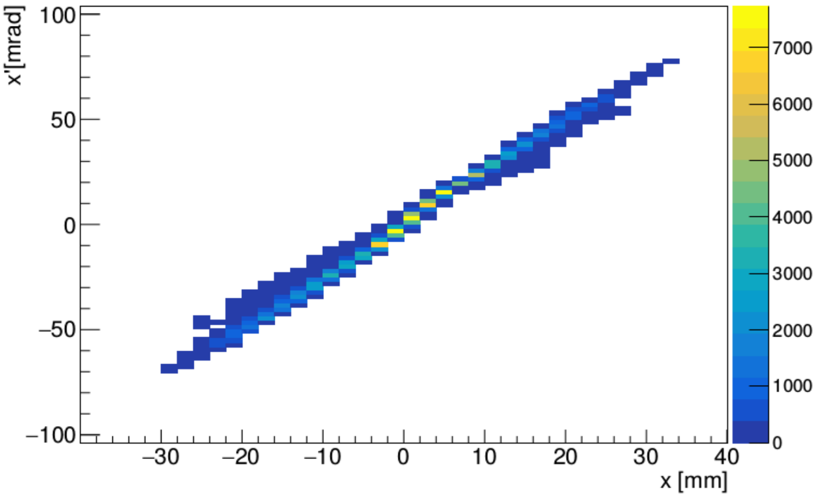

Fig. 4.12 Result of the threshold routine. The beam is composed by D^+ of 135 mA at 100 keV.

In order to obtain the clean signal of the beam, the threshold method was used. First, a small threshold, given from the SCUBEEx-ghostbuster, is considered. This threshold is then subtracted to the whole plane.

The procedure is repeated increasing with small step the threshold. The emittance is checked at each value, in order to follow its evolution.
The procedure is stopped when the resulted emittance and Twiss parameters of the cleaned signal are equal to the SCUBEEx-ghostbuster emittance (or within its error bar). The result are shown in Fig. 4.12. If there are separated artifacts from the main ellipse that survive the threshold, they are set 0 graphically and the emittance is recalculated.
This method does not only give the clean signal, but also counter-checks the results of the emittance calculation.

Chapter 5

Rms trace-forward method with constant s.c.c.

5.1 Introduction

The first approach to study the system was performed using a simple model described in the following pages. The main characteristics and the trend of the beam parameters with the line settings were studied.
Once the main beam dynamics characteristics of the transfer line were identified, the trace-forward method with constant neutralization was applied with this model. The estimated beam input was accelerated into the RFQ in order to analyze its behavior. The beam studied is H^+ of the order of 60 – 55 mA at 50 keV.

5.2 Preliminary study

The implemented model was based on a single species transport, starting 19.8 mm away from the plasma electrode up to the emittancemeter position or the BS. The line layout is reported in Chapter 3 and refers to phase A2: the emittancemeter is placed downstream the injection cone at approximately 367 mm from the cone end.

5.2.1 Extraction simulation

The input conditions are given by preliminary AXCEL simulation of the extraction source, simulating 80 mA of total extracted current with a 70% proton fraction, 25% of molecular H_2^+ and 5% of H_3^+.

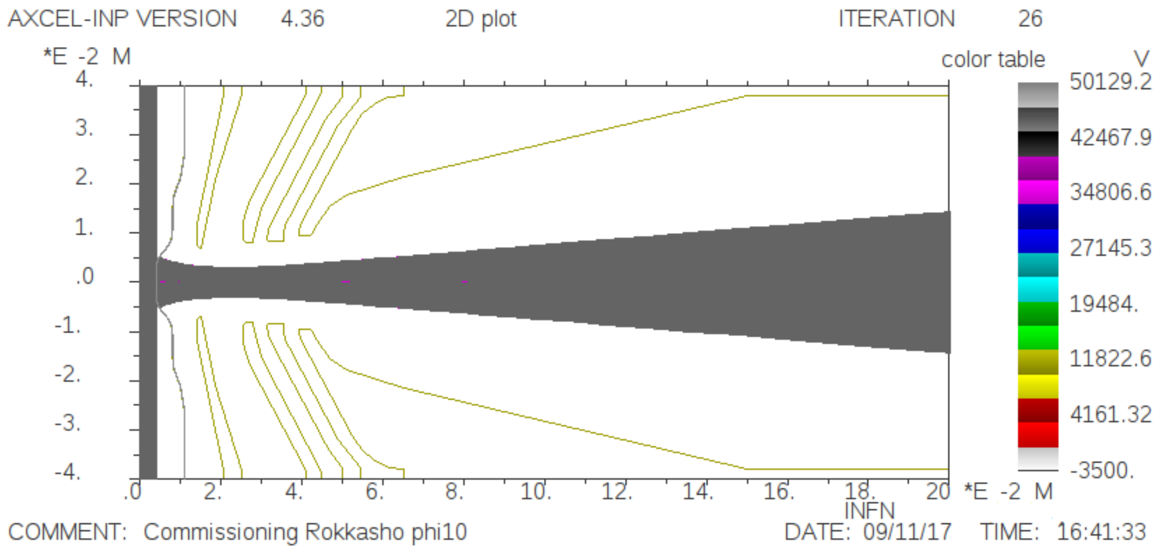

Fig. 5.1 Trajectory in the extraction system for proton case. The total current extracted is 80 mA

The intermediate electrode potential is set to 25 kV, while the repeller at -3.5 kV. When the trajectory finds on its path a negative voltage of -100 V, then, a neutralization factor of 0.965 applies.

The resulted Twiss parameters and emittance are applied to a parabolic distribution generated at 19.8 mm where the transport simulation began. The choice of not using the AXCEL phase space distribution is related to the possibility of a fast change of the input Twiss and emittance, directly on the transport simulation.

5.2.2 Line simulation

The line simulation is performed via Tracewin software. The model includes the solenoids and the repeller cone field map. The line clearance was implemented in the simulation: such characteristics are important especially in the cone zone, where it acts (with a large mismatch beam) as a collimator. The symmetry of the system was assumed to be cylindrical. Fig. 5.3 reports an example of the particle density along the line as well as the beam line apertures and the space charge compensation factors.

As far as the neutralization level along the line is concerned, a constant space charge compensation factor, radial independent (i.e. $\frac{\partial \eta(r,z)}{\partial r} = 0$) was used. In axial interval of 10 cm, almost centered on the repeller cone electrode, the space charge compensation was set to 25%.

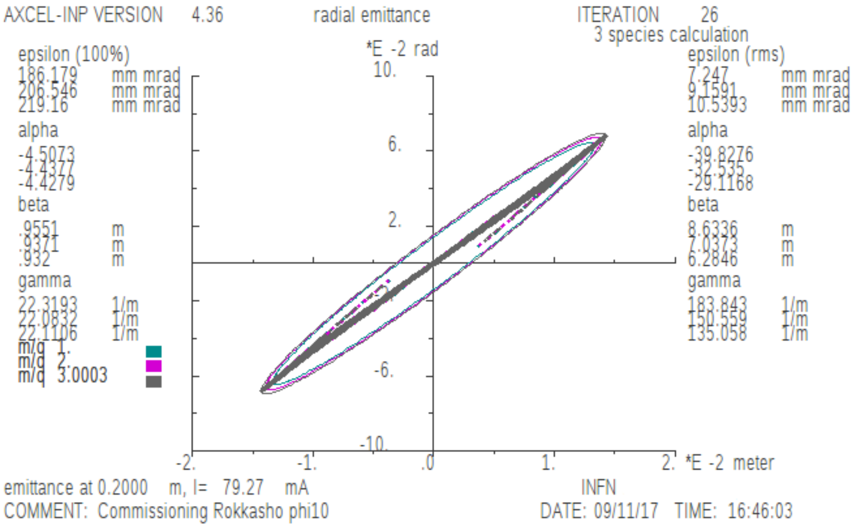

Fig. 5.2 Emittance of the proton beam extracted at 19.8 mm from plasma electrode with AXCEL-INP

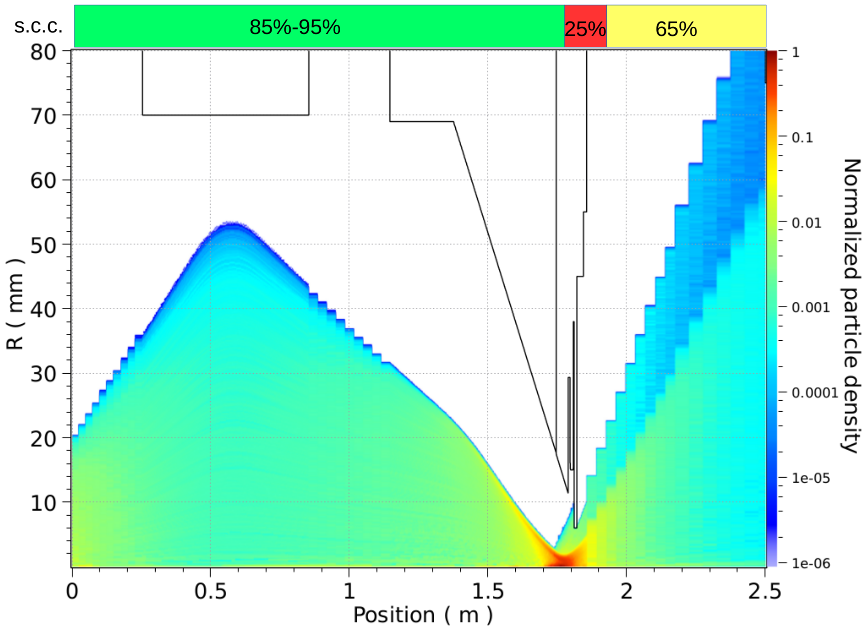

Fig. 5.3 *rz* particle density plot of a typical transport with the preliminary model of 60 mA proton beam along the LEBT. The beam density and the space charge compensation factor (s.c.c.) are reported at the top of the plot.

After the cone repeller, the neutralization was set to 65%, a lower value than the previous line segment. This was justified by the better vacuum conditions, often one order of magnitude less than the pipe before the cone. It is important to remember that the following studies were preparatory to the trace-forward; therefore the focus was on the qualitative response of the line, not on the quantitative calculations. Despite the not self-consistency of the choices (but neither not-realistic), this simplified model was still able to give interesting results.
In order to estimate the effect of the beam pipe clearance, the applied and self-fields on the beam distribution, the macro-particle tracking routine PICNIR [14] was used: 30000 macroparticles for each $\beta\lambda$, 16×8 mesh subdivision in r and z, based on [36] in order to reduce simulation noise and entropy growth.

5.2.3 Results of the simplified model

The main objective was to discover the response of the LEBT to different beam inputs and the neutralization on the first segment (see Fig. 5.3).
The tested beam inputs are presented in table 5.1:

Table 5.1 rms parameters of the input beams for the study of preliminary model

Twiss set	$\varepsilon_{\mathrm{rms,n},x}$	α_x	β_x	a'_{rms}	a_{rms}
1	0.15	-15.9	3.4	46.5	9.9
2	0.1	-15.9	3.4	38.0	8.1
3	0.07	-30.0	8.6	37.7	10.8
4	0.08	-12.0	3.4	25.7	7.3
5	0.095	-18.0	4.9	35.0	9.5

At each beam input is associated the relative rms divergence of the beam, which has an important role on the emittance growth along the line. For each beam input and each neutralization, the solenoid strengths were varied. The first solenoid (closer to the source) strength was varied of 25%, while the second solenoid (closer to the RFQ) of 50%.
The observables were: the root mean square normalized emittance $\varepsilon_{rms,n}$, the beam current (i.e. transmission) and the Twiss parameters. The values were taken at different points of the lines in order to follow the beam evolution.
An important measurement performed during the commissioning involves the beam stop current vs different solenoid couples. The transmitted current is a function of the extracted beam characteristics and the geometry of the system:

$$I_{\mathrm{BS}} = f(\varepsilon_{\mathrm{rms,n}}, \alpha, \beta, \eta, \langle x \rangle, \langle x' \rangle, \xi_{\mathrm{geo}}, \mathrm{B}_{\mathrm{sol1}}, \mathrm{B}_{\mathrm{sol2}}) I_{\mathrm{ext}} \tag{5.1}$$

where $\varepsilon_{rms,n}$, α_x and β_x are respectively the rms normalized emittance and the Twiss parameters; $\langle x \rangle$ and the $\langle x' \rangle$ are the first order moment of the beam; η is the beam s.c.c. factor, which directly influences the neutralization and ξ_{geo} is the factor which takes into account the geometry aperture.

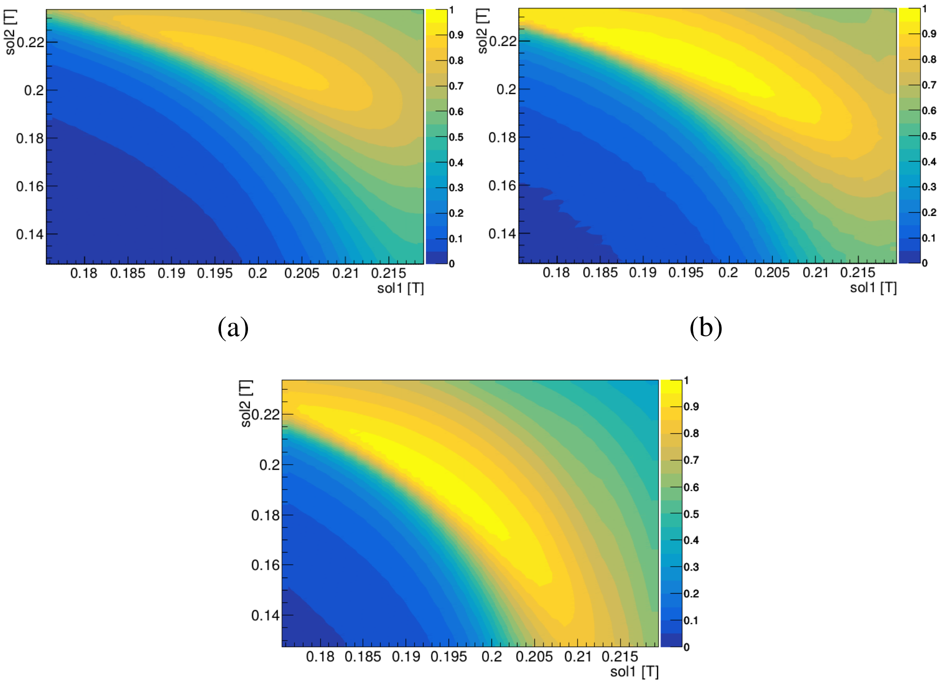

(a)

(b)

(c)

Fig. 5.4 Transmission up to BS for different Twiss set and s.c.c. (a)Twiss set 1 85% s.c.c., (b)Twiss set 1 91% s.c.c., (c)Twiss set 2 91% s.c.c..

In the study misalignments and consequent beam deviations were not taken into account. Example of how the different Twiss parameters and the neutralization in the first part of the line can modify the transmission function to the beam stop is shown in Fig. 5.4.

The areas are strongly related to the solenoid strength, while the maximum reachable transmission decreases with smaller compensation degrees. The orientation of the transmission isobars depends on the extracted Twiss parameters. As a result, it is possible to use these plots to qualitatively estimate the behavior of the transport: larger area of maximum transmission indicates a good quality beam through the LEBT, which implies a better emittance at the

RFQ injection point. Moreover, it is possible to use the measurement of this plot to infer the input beam.

The simulation allows also to calculate the emittance at different position for several solenoid couples. The trend of the emittance with respect to the solenoid couple is shown in Fig. 5.5. In all cases a), b) and c) the emittance is increasing from the lower right (solenoid 1 stronger than solenoid 2) to the upper left corner (solenoid 2 stronger force than solenoid 1). This effect is given by the combination of the non-linearities of the applied fields (solenoid 2) and the space charges: as far as the solenoid 1 is weakened, the beam radius in the second solenoid increases. In this way, part of the beam will experience emittance growth due to the non-linear focusing of the magnetic lens. This behavior was confirmed experim?entally during the commissioning campaign [9]. The emittance values does not follow a monotonic trend with respect the s.c.c.: while there is an increase of the emittance growth due to low neutralization, it is also true that the non linearity of the solenoids and the cone contribute strongly to the emittance growth/decrease.

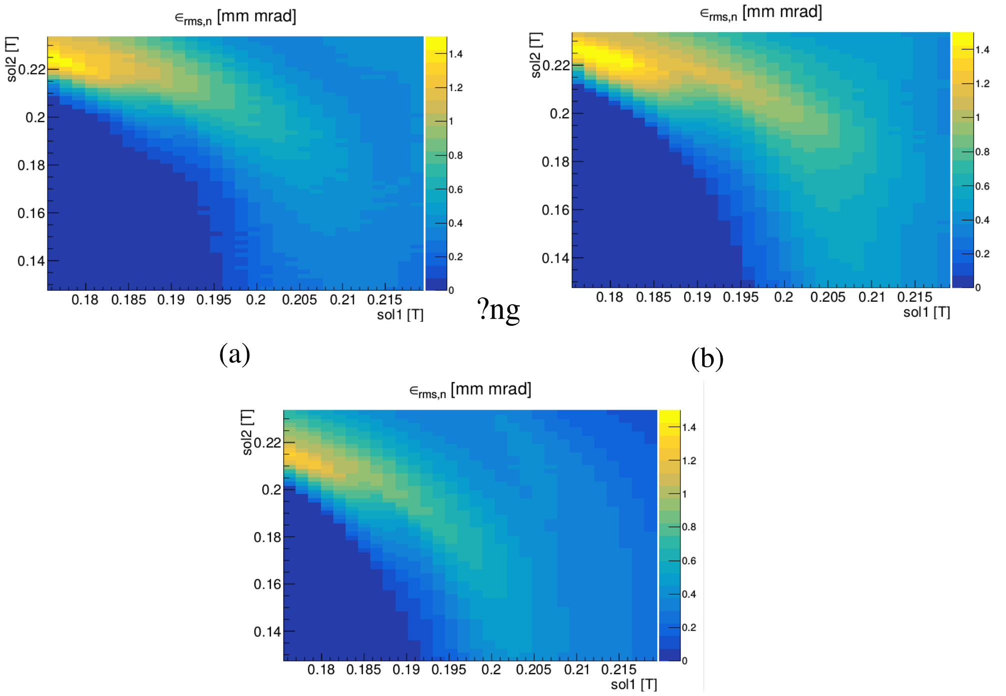

(a)

(b)

(c)

Fig. 5.5 Emittance for different Twiss set and s.c.c. at EMU (emittancemeter): (a)Twiss set 1 and neutralization 85%, (b)Twiss set 1 and neutralization 91%, (c)Twiss set 2 and neutralization 91%.

The net effect of the above considerations is the possibility to reduce the emittance growth tuning the solenoid lens. However, the range is not very wide, due to the fact that other conditions for the injection into the RFQ need to be fulfilled at the same time (such as the mismatch and the current). Such consideration is validated by Fig. 5.4: the I_{BS} is not monotonic from lower right to upper left corner, the maximum current transmitted does not correspond to the minimum emittance.

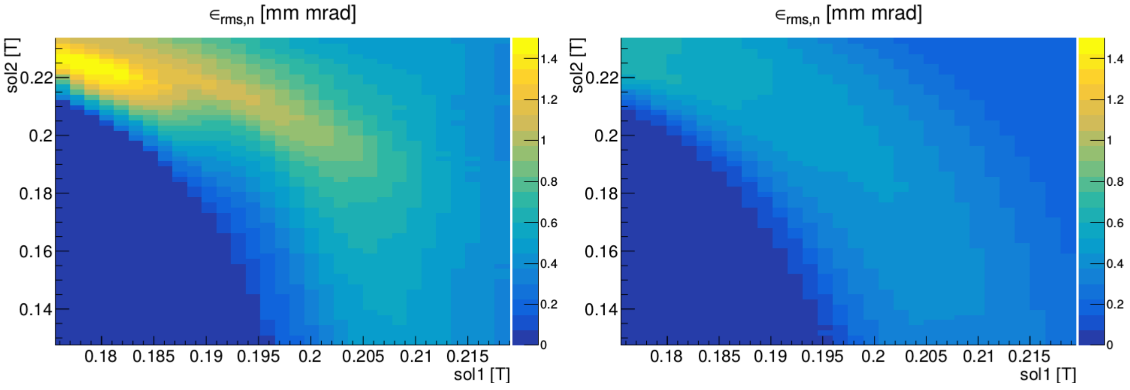

(a) (b)

Fig. 5.6 Emittance at EMU position (a) and at the RFQ injection (b) respect to the same couple range $(sol1, sol2)$

The emittance is also a function of the axis coordinate z. Fig. 5.6 shows the emittances plot in two different positions: at RFQ injection and at EMU position (364 mm after). The maximum values at the EMU position are larger than at the RFQ injection point.

Such behavior indicates a possible overestimation of the emittance, if the emittance itself is measured tens of centimeter after the injection point. Thus, a careful emittance growth estimation is required in order to infer the emittance at the RFQ injection point.

The last important parameter trend to be studied is the mismatch at the RFQ input. The mismatch definition which was used, is explained in [9].

It is worth to compare several beam inputs and line s.c.c., comparing the mismatch and the emittance at the RFQ injection.

In all the cases, smaller values of mismatch are located in the upper left part of the plot. Unfortunately, as shown in Fig. 5.9, the maximum emittance values are located also in that zone.

Collecting all together the requirements ($\varepsilon_{rms,n} < 0.3$ mm mrad, $M < 50\%$ and $I/I_0 > 90\%$) it is possible to identify specific areas where all the conditions are met simultaneously, as in Fig. 5.7. For the set studied, all the matching zones falls in the upper-left part of the scan plot plane. It is important to remember that the results presented up to here belong to a preliminary study; therefore the matching zones can migrate around the plot but not in the

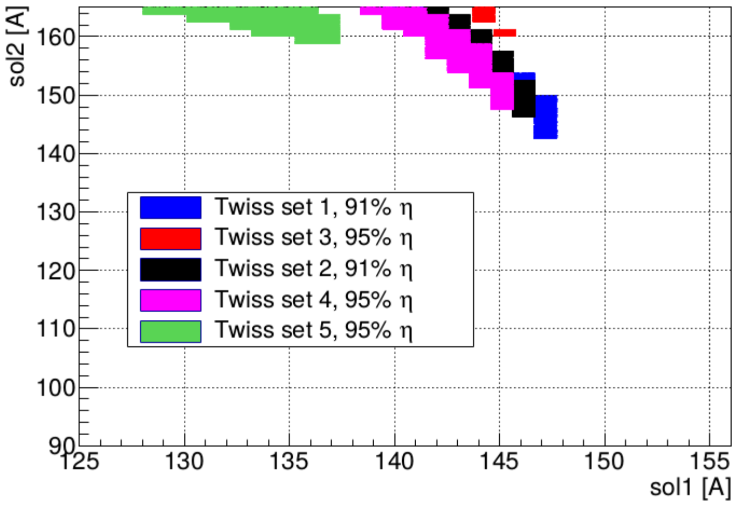

Fig. 5.7 Matching zones for different input conditions and s.c.c. degree which respect $\varepsilon_{rms,n} < 0.3$, mm mrad, $M < 50\%$ and $I/I_0 > 90\%$

lower part (i.e. for values of solenoid 1 larger than solenoid 2) as it will be presented in the last part of the chapter.

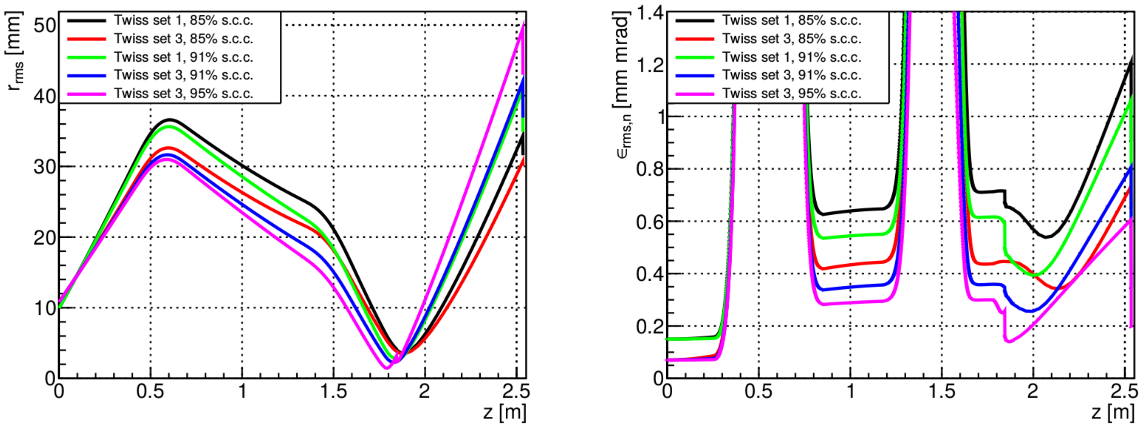

Fig. 5.8 LEFT: rms size of the beam for different input Twiss and s.c.c.. RIGHT: rms emittance for different input Twiss and s.c.c.

The last information given by this model is related to the emittance growth: more divergent is the beam at the extraction system, more emittance growth occurs after the solenoid 1. Fig. 5.8 shows this phenomena. The Twiss set 1 has larger divergence than Twiss set 2 (see 4.1), which means larger beam in the first solenoid: for the same mechanism that brings larger emittance in the upper left plots (Fig. 5.5), the non-linear focus of first solenoid lens couples with the space charge effect, leading to larger emittance growth after the first solenoid (see right plot in Fig. 5.8).

This emittance growth will affect the following transport, causing a low quality beam at the RFQ input. Therefore, a crucial commissioning objective is to ensure a low divergence and low emittance beam after the source extraction. Another result is the high sensibility of this model with respect to the neutralization: a few percent of beam neutralization changes the beam behavior of more than 20%.

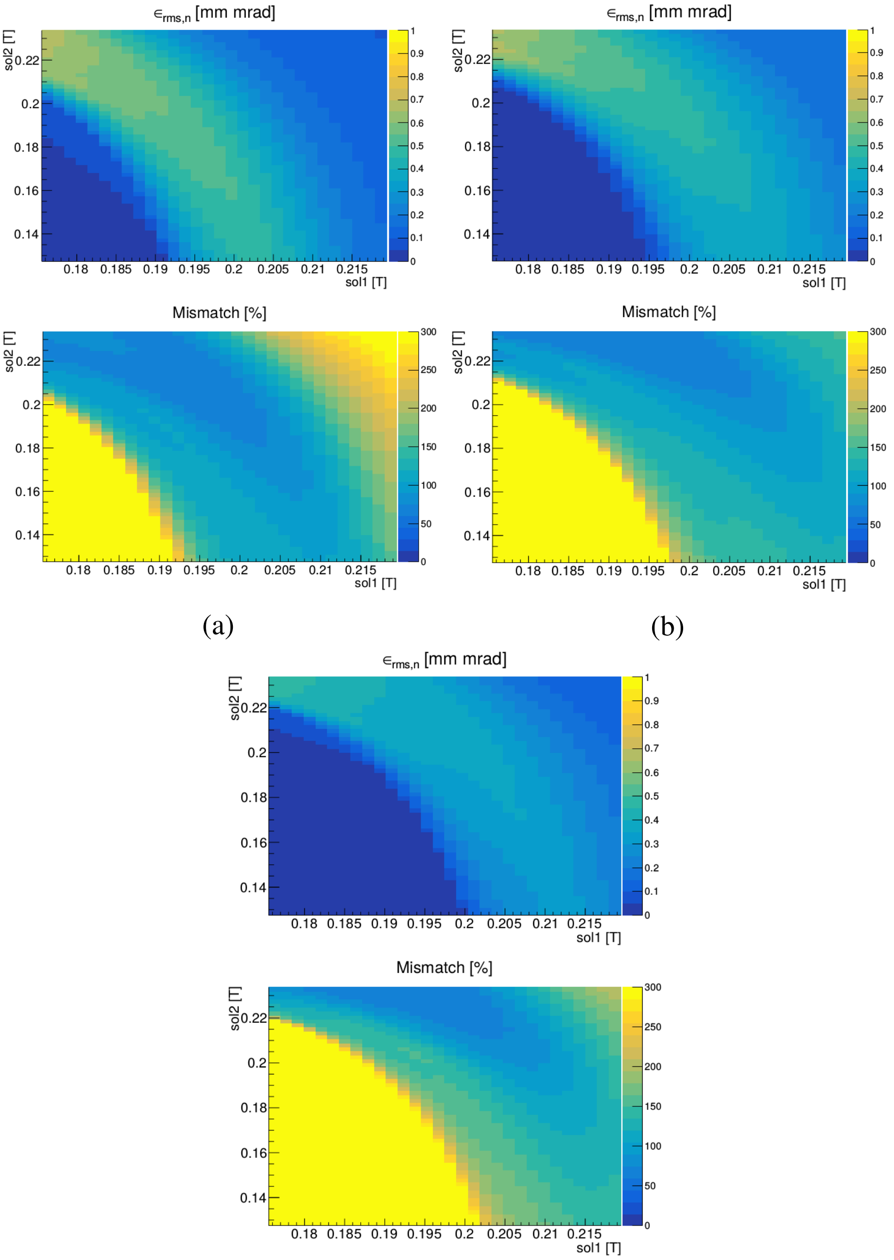

(a) (b)

(c)

Fig. 5.9 Mismatch and emittance at the RFQ input point. (a)Twiss set 1 s.c.c. 85%, (b)Twiss set 1 s.c.c. 91% and (c) Twiss set 2 s.c.c. 91%

5.2.4 Comparison with experimental data

During the proton beam commissioning, a measurement of I_{BS} vs the solenoid couple with the repeller of the cone grounded (switched off) was performed. The experimental 2D plot was then compared with the simulations: two input beam parameters were tested: Twiss set 1 and 2. The space charge compensation was put 91% along the line up to the end of the repeller cone area (see Fig. 5.3). No decrese of s.c.c. are expected in the cone zone because no electron repulsion is obtained in that area without the electric potential. Therefore, the s.c.c. are preserved. The result can be seen in Fig. 5.10. The xy axis shows the currents of solenoid wires.

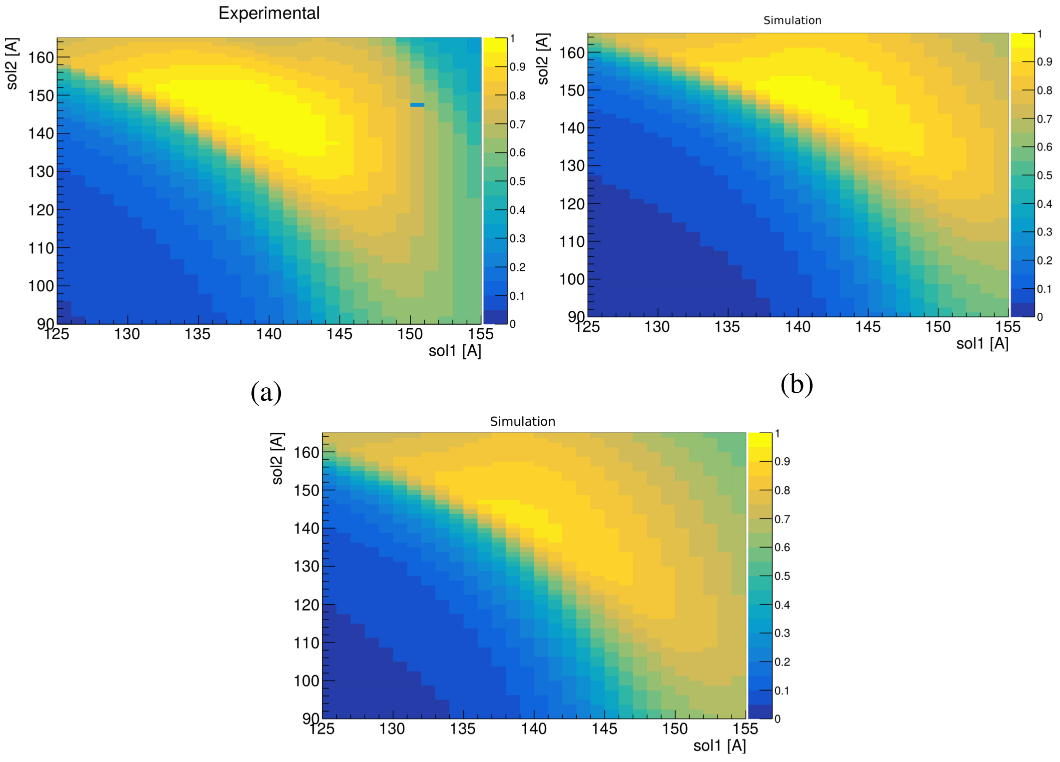

(a)

(b)

(c)

Fig. 5.10 BS transmission vs solenoid couple. Repeller off case. (a) Experimental measurement of the I_{BS}/I_{ext} vs $sol1, sol2$ with the repeller off. (b) Twiss set 1, s.c.c. 91%. (c) Twiss set 2, s.c.c. 91%

In order to analyze the agreement quantitatively, the I_{BS} trend was plotted with respect to the fixed solenoids values, 145 A for solenoid 2 and 140 A for solenoid 1 respectively [27]. The plots in Fig. 5.11, derived from Fig. 5.10, show the comparison between the measurement and the simulations currents for a fixed solenoid 1 and 2, for input Twiss set 1 and 2. The Twiss set 2 follows the trend closer than the Twiss set 2.

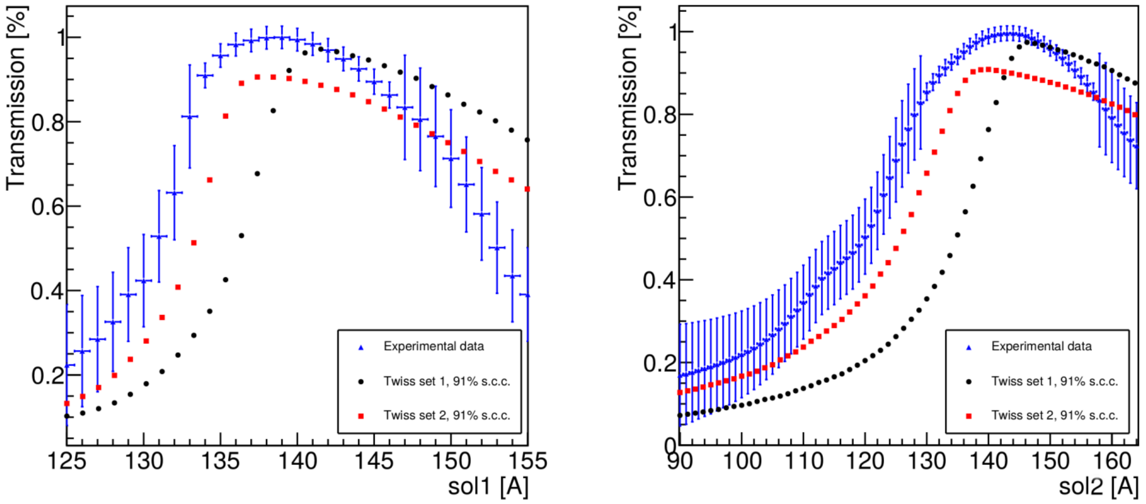

Fig. 5.11 LEFT: plot of the I_{BS}/I_{ext} vs solenoid 1 current, with solenoid 2 fixed 145 A. RIGHT: plot of the I_{BS}/I_{ext} vs solenoid 2 current, with solenoid 1 fixed at 140 A. The experimental data are represented by the blue triangles, the simulations with Twiss set 1 and Twiss set 2 are in black circle and red square respectively.

The difference between the best fit curve and the measured points can be explained by the approximations of the model with respect to the reality, such as the fixed, radial independent and arbitrary degree of the space charge compensation. Another important approximation is the input beam spatial distribution: the ratio of the current transmitted through the cone depends on the beam spatial distribution at the exit of the source, and, in particular, on the ratio intercepted by the cone. Therefore, small distribution differences cause deviations on the current trend on the BS. The source and solenoids misalignment can also change the curve trend.

In conclusion, despite all the approximations, the maximum deviation between the data with errors and the Twiss set 2 simulation is less than 20 % in all the plots. However, the precision of this model cannot reproduce the Twiss parameter and the emittance at the emittancemeter. Therefore, despite a good insight of the LEBT behavior, the best solenoid LEBT tuning to match the beam at the RFQ needs a more precise model.

5.3 Rms trace-forward method application to LEBT

The preliminary model can only supply information on the general response of the transfer line; in order to reproduce more accurately the emittance and Twiss measured during the campaign, the rms trace-forward method was applied.

The method is based on matching the emittance measurements changing the beam input parameters. The results is an equivalent (i.e. rms quantities evolution should follow the real beam rms quantities) beam evolution along the line. Once a solution is found, it is possible to retrieve any information in any point of the line.
There are some specific adjustments on the s.c.c. that need to be done in order to adapt this method to the IFMIF/EVEDA LEBT:

- The space charge compensation along the line is a variable.
- It can be divide in three z intervals: the interval before the cone, the cone region and the zone after the cone. The s.c.c. (space charge compensation) decrease in the cone part up to 0 when the repeller cone is switched on.
- The s.c.c. compensation in the two zones before and after the cone are approximated constant along z, while, in reality, they may have a more complex trend [37, 38]. Nevertheless, this choice was adopted in order to change easily their values during the matching.
- During the experimental campaign, it was possible to measure the s.c.c. between the two solenoids via the FGA (placed between the solenoids): the experimental value was used in order to estimate the value of the neutralization in the part of the line before repeller cone.
- The software Tracewin is capable of a single species transport with space charge interaction. In case of proton extraction, the contaminants present is not negligible and therefore it was important to determine the proton ratio. The Doppler shift spectrometer supplies this information.

The iterative procedure was applied as follow:

1. First set of $\varepsilon_{\mathrm{rms,n},x}$, α_x, β_x was calculate via the AXCEL software. The rms quantities were assigned to a parabolic beam distribution at around 20 cm from the plasma electrode aperture.
2. The neutralization of the line was first set to the measured value from FGA. The value after the cone was set to a starting value (e.g. 80%)
3. All the line optical elements such as the solenoids and the repeller were set as in reality, with the same applied field.

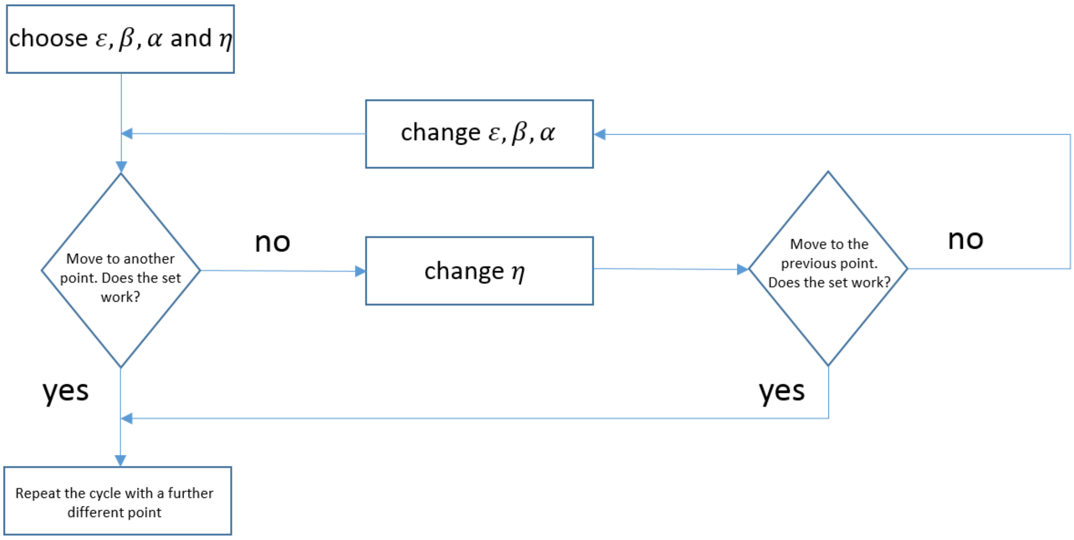

Fig. 5.12 Trace forward cycle adapted to the IFMIF/EVEDA LEBT.

4. The distribution is transported up to the emittancemeter. If the parameters (also the I_{BS}) agree within 30% and the simulation current within 20% the mean value of the error bar, the method proceed with the next measured point. If not, first the s.c.c. after and before the cone is adjusted; if not sufficient, the beam input rms parameters are slightly changed.

5. When a rough agreement is obtained, all the quantities (α_x, β_x, $\varepsilon_{rms,x}$ and η before and after the cone) are slightly adjusted in order to obtain as smaller as possible difference with the experimental data.

6. The procedure is iterated up to a fixed set input parameters within all the experimental points is found.

The iteration between the different measured points on the solenoid scan plane (see Fig. 5.13) is an important counter-check and ensures consistency to the method.

5.3.1 Experimental input point

The simulation results presented here are relative to a 85 mA extracted beam current (I_{ext}) (read at the main power supply) at 50 keV. The Doppler shift spectrometer measurement indicated $70 \pm 5\%$ H^+ fraction [27], thus, with respect to the total extracted current, the proton I_H is $55 - 63$ mA. The generalized perveance of the un-neutralized beam ranges from $3.25 \times 10^{-3} \geq Q \leq 5.0 \times 10^{-3}$. The smaller value refers to the selected proton beam transport, while the largest perveance takes into account the contribution from H_2^+ and H_3^+ (no negligible in the extraction region). The higher contribution will matters only in less of the first half of the LEBT: then the contaminants will be lost due to the collisions with the pipe apertures and cone. The D.C. was 10%, with 10 ms pulse length and 100 ms repetition rate. This implies that the emittance data taken are reliable, because the power deposition onto the slits are below the deformation level (10% see Chapter 3). Moreover, the power deposition of the H^+ for such beam is a factor 4.7 less the deuteron case. Therefore, the expected slit deformation is even smaller than the sam D.C. deuteron case.

$\varepsilon_{\mathrm{rms,n},x}$ and I_{BS} trend respect to the solenoid couples

Following the result of the preliminary model, the emittance measurements were focused on the zone of interest for RFQ matching, located in the upper left of the plane (Fig. 5.13). It was found a monotonic trend of the emittance going from the down right up to the upper left corner, as foreseen by the simulations done in the previous section. Fig. 5.13 shows this effect.

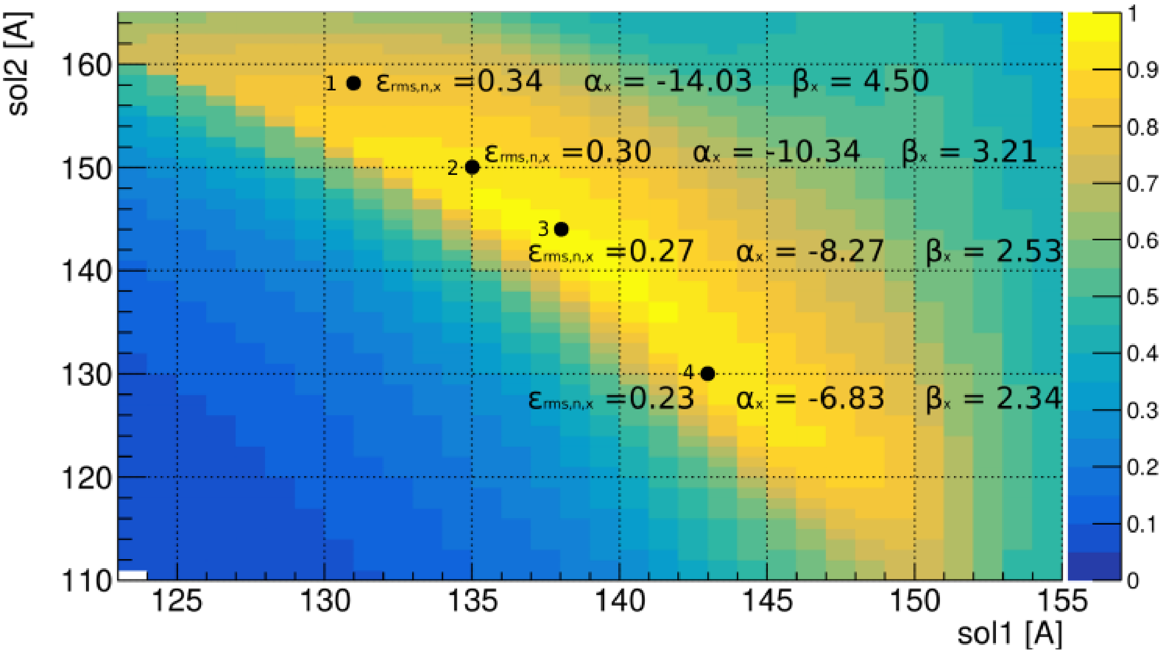

Fig. 5.13 Measured transmission from the extraction up to the BS and $\varepsilon_{\mathrm{rms,n},x}$ (taken at the EMU) vs solenoid 1 or solenoid 2 currents. The four measurements of the emittance used for the trace-forward are reported.

The first point emittance measurement used for the trace-forward is the $\varepsilon_{\mathrm{rmsn},x} = 0.27$ mm mrad (point 3). It is very important to ensure, for the first step of the method, an high level of transmission ($> 90\%$) from the extraction hole to the BS (i.e. on Fig. 5.13 the points at 100% transmission). As a matter of fact, it is critical to collect all the beam for the initial rms quantities calculation, in such a way to avoid a large initial bias on the method. Otherwise, different Twiss and emittance values may results due to the losses of the nominal beam on the cone.

FGA measurement and calculation of space charge compensation

In order to estimate the space charge compensation of the beam, the signal of the FGA was used. The LEBT solenoid 1 and solenoid 2 were set to 135 A and 150 A respectively. In the experimental framework, the derivative of Eq. 3.26 is a convolution of the Maxwell distribution (see Chapter 3) and the response function of the FGA. In order to check the results of the Maxwellian fit model, a fit based on the sum of two erf functions was also use. The fit results are shown in Fig. 5.14.

Table 5.2 FGA fit results

Fit f	σ [V]	FWHM [V]
Maxwellian	0.60 ±0.11	1.16 ±0.22
double erf	0.63 ±0.06	1.48 ±0.14

The fitting range is reduced to the central part of the FGA signal: the initial part (from 0 to 2 V) shows current trend due to the grid optics: as the V_3 voltage increases, the lens effect of the grids exchanges the $v_\perp$ of the ionized gas with v_z, decreasing the number of ions repelled by the grid. As explained in Chapter 2, the space charge compensation factor η is a function of the neutralized $\Delta\Phi$ and unneutralized beam potential $\Delta\Phi_{\text{un}}$. The sigma of the ion distribution, obtained as a function of a parameter (see Eq. 3.26), is proportional to the depth of the residual potential hole.

Taking the $2 \times 3\sigma$ values, it is possible to get the energy interval which encloses the 99% (for the erf function fit) of the gas ions. For this case, the 3σ value is 3.78 ± 0.36 V for the double error function and 3.60 ± 0.66 for the Maxwellian function. Thus, $\Delta\Phi = 3.78$.

The estimation of $\Delta\Phi_{\text{un}}$ needs the transverse spatial distribution of the beam in order to be estimated. During the data acquisition, it was not possible to measure directly the beam profile. Therefore, it was calculated with the Tracewin software, which however depends on the s.c.c. used. In order to overcame this issue, several line transport simulations with s.c.c. range from 91% to 99% were performed (this range is consistent on what found in Section 5.2.3). This allows to check the sensibility of the beam radius at the FGA position respect the applied neutralization calculation. The variation resulted less than 10%.

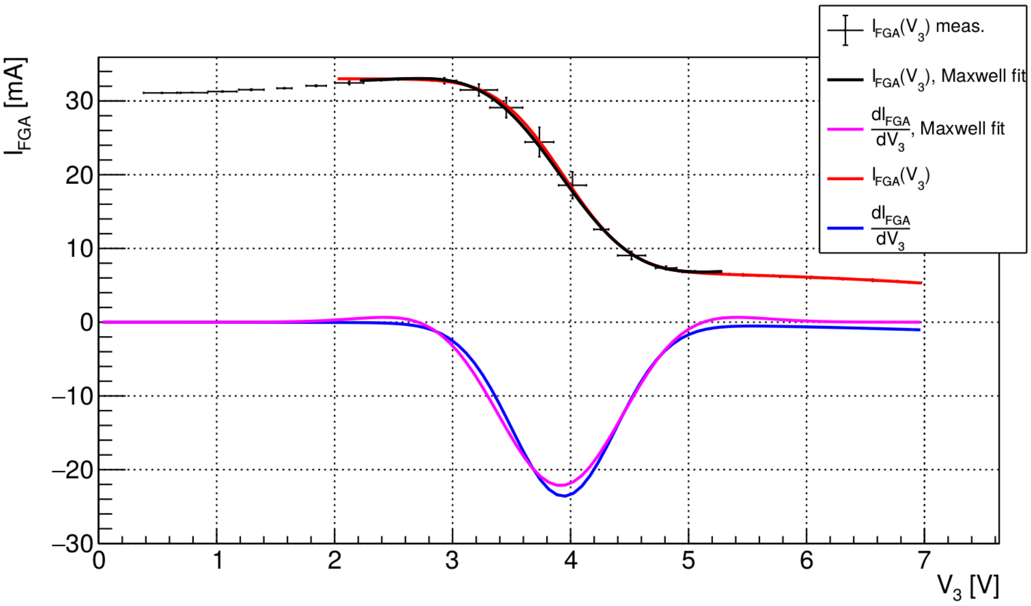

Fig. 5.14 Measured signal of the FGA for the 50 keV 55 mA proton beam extraction. The CDF of the Maxwell distribution and the double erf functions are shown (red curve is the double erf fit, while the black is the CDF Maxwell fit). Their derivatives are also displayed (violet curve for CDF Maxwell and blue for double erf fit).

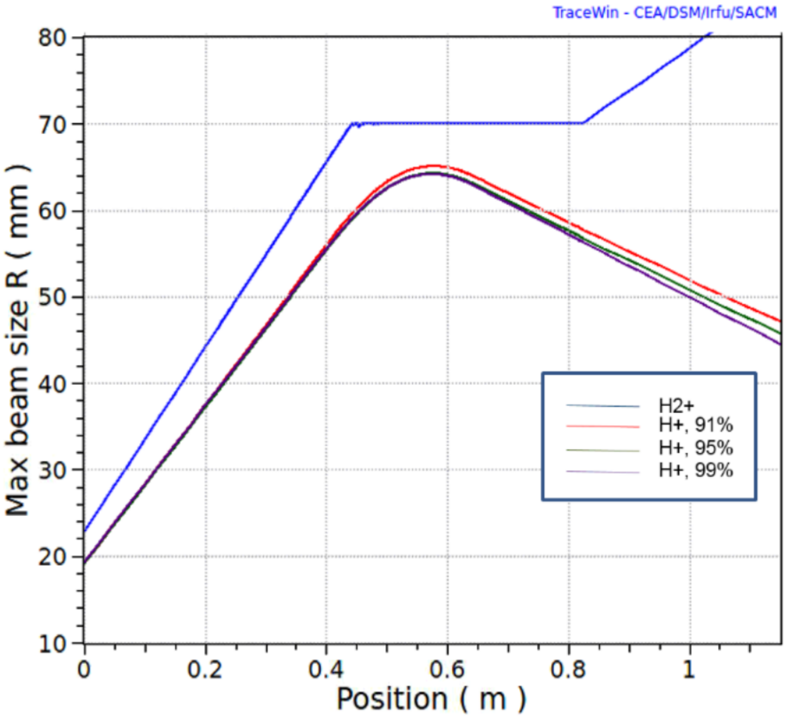

Fig. 5.15 Beam envelopes for different s.c.c. cases. The H_2 envelope is also displayed.

The contaminants contribution (H_2^+ and H_3^+) was not negligible for the proton extraction case. Therefore, the H_2^+ distribution was also calculated and added to the estimation. The beam envelopes are shown in Fig. 5.15.

The Tracewin program does not give the information on the self potential of the beam. Therefore, the H^+ and H_2^+ distributions at the FGA positions were extracted and inputed in COMSOL. A beam pipe with 253 mm diameter surrounded the macroparticles. The model calculates, for each beam transport, the potential, solving the Poisson equation with a finite element method.

In order to compare the results, the potential of a uniform cylindrical charge distribution with the radius equal to the mean radius of the simulated distribution was used.

The relative formula is described by Eq. 5.2:

$$\Delta\Phi_{un} = \frac{I_{sp}}{4\pi\varepsilon_0\beta c}\left(1 + 2ln\left(\frac{r_\mathrm{p}}{a}\right)\right) \tag{5.2}$$

where I_sp is the species current (H_2^+ or H^+), r_p is the beam pipe.

Table 5.3 Unneutralized beam potential for different simulated s.c.c. factors

s.c.c. in sim.	simulated Φ_un [V]	calculated Φ_un [V]	$\eta_\mathrm{sim}[\times 10^{-3}]$	η_calc $[\times 10^{-3}]$
91%	692.21	719.04	4.33	4.24
95%	747.31	781.22	4.08	3.90
99%	788.10	789.52	3.89	3.86

The unneutralized potentials are reported in table 5.3. The ratio between the neutralized vs unneutralized potential as shown in Chapter 2 is $\eta = \Delta\Phi/\Delta\Phi_{un} = \Phi_{peak}/\Phi_{un,peak}$.

The neutralized value is taken from the previous section (i.e. 3.78 V). The formula 5.3 gives the total degree of neutralization:

$$s.c.c. = 1 - \eta = 1 - \frac{\Delta\Phi}{\Delta\Phi_\mathrm{un}} \tag{5.3}$$

The s.c.c. estimation is shown in 5.17. The values are reported with respect to the simulation neutralization level.

The parametric simulations shows that for each simulated beam transport condition, the expected s.c.c. is above 99%, with negligible deviation.

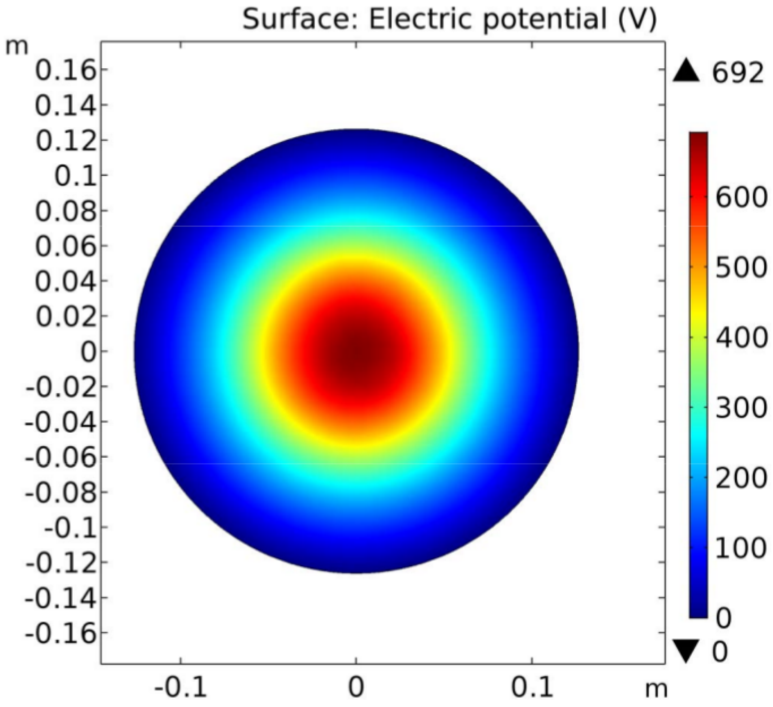

Fig. 5.16 86 mA total beam 2D transverse potential distribution for 91% s.c.c. beam transport at the FGA axial position

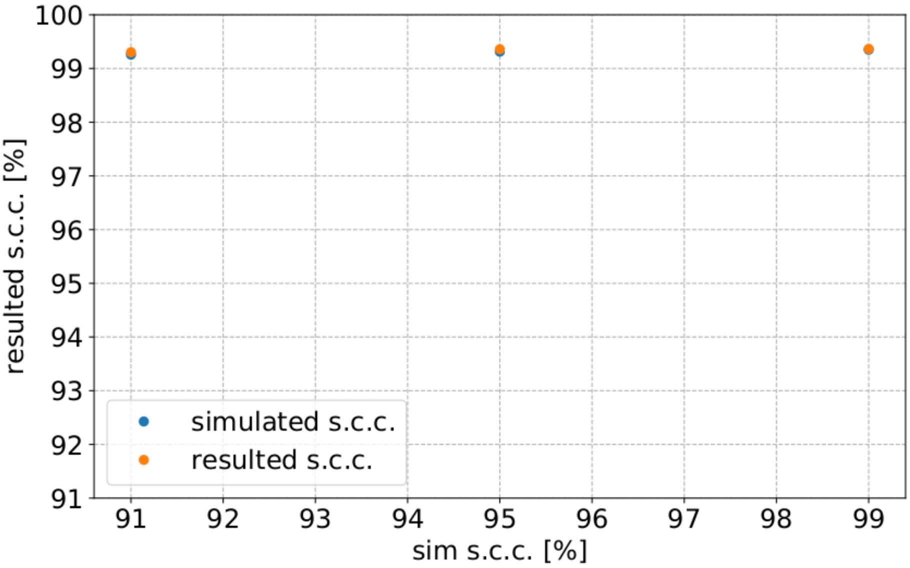

Fig. 5.17 86 mA beam s.c.c. estimation. The points (blue simulated and orange theoretical) are reported respect to the neutralization values implemented in the simulation. All values are above 99% for any implemented simulation neutralization level

5.3.2 Results

s.c.c. behaviour

In the previous section the s.c.c. compensation for the $(135,150)$ point was estimated. During the trace-forward process it turned out that the model approximation on the constant neutralization and value is limited to certain extension in the plane (sol1,sol2)
As far as the solenoid couple moves closer to the boundary of one of these zone, the difference in between the simulation and experimental results grows more than 20%. The boundaries of these areas are reported in 5.4.
Therefore, it was necessary to tune the s.c.c. before and after the cone for each part of the plane. One of the effect of such approach (from 5.4) is the not low neutralization after the cone, despite the very good level of vacuum.

Table 5.4 Simulated neutralization before and after the cone

point	sol1,sol2 [A]	s.c.c before cone	s.c.c. after cone
3	(134,145), (135,145)	96%	80%
2	(127,138), (145,155)	99% (meas.)	84%
1	(125,135), (155,165)	99%	87%

The vacuum level after the cone was around 10^{-7} mbar, while in the main LEBT assembly was 10^{-5} mbar. Thus, the candidates for the neutralization after the cone are the electrons emitted from the emittancemeter due to proton collisions. Therefore, the neutralization in the model after the cone should be different when transporting the beam up the BS or during the emittance measurement. In order to preliminary check this phenomena, the trace-forward study was used: as described at the beginning of the section, the method uses also the transmitted current at the BS in order to match the s.c.c. and the input bem parameters. In order to match the emittance value and the BS transmission with the same solenoid couples, input beam parameters and the s.c.c. before the cone, two neutralization factor values after the cone needed to be implemented, as shown in 5.5.

Table 5.5 Effect of the emittancemeter, preliminary results

s.c.c.	Meas. $\varepsilon_{\mathrm{rms,n,x}}$	Sim. $\varepsilon_{\mathrm{rms,n,x}}$
87%	0.34 ±0.02	0.32
0%	0.34 ±0.02	0.43

s.c.c.	Meas. $\mathrm{I_{BS}}$	Sim. $\mathrm{I_{BS}}$
87%	50 ±1	46
0%	50 ±1	55

The table shows that in order to match the values, it was necessary to change the neutralization after the cone. In this way model correctly treats the different s.c.c. regime: when the

Allison is inserted 87% of neutralization resulted from the routine. In the other case, when transporting the beam up to the BS, the s.c.c. obtained was 0%. This was the first preliminary evidence of the effect of the emittancemeter (and secondary electron in general) on the measurements. As it will be explained in Chapter 6 and mentioned above, this phenomena can be ascribed to the contribution of the secondary electrons, emitted when the beam collides with the tungsten shield of the Allison scanner. Their dynamics is fairly complex and need a different software in order to be treated.

Benchmark between the simulation and experiment

In order to simplify the treatise, at each emittance measured point in the solenoid scan plot it was assigned a code number: from the upper left to lower right corner (see Fig. 5.13)
The phase space emittance for point 2 can be seen in Fig. 5.18. The rms trace-forward method increases the tale contribution with respect ot the overall distribution.

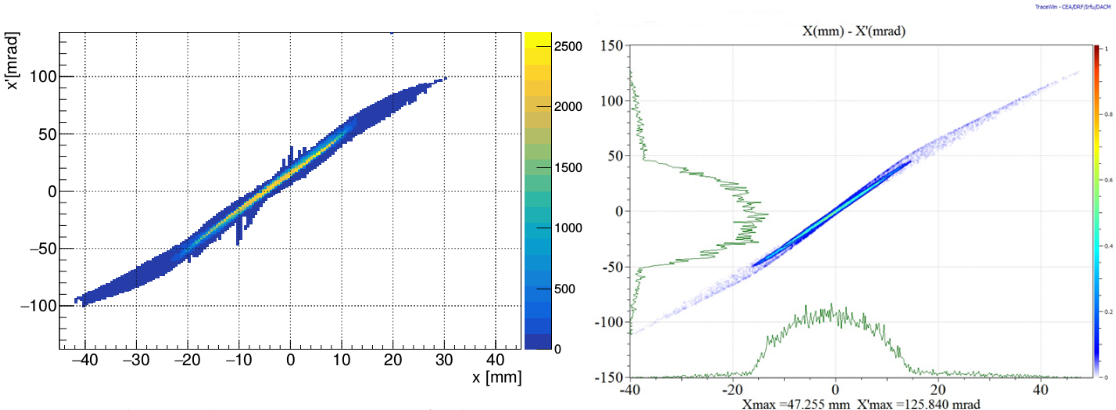

(a) Experimental measurement of the I_{BS} vs $sol1, sol2$ with the repeller off.

(b) Twiss set 1, s.c.c. 91%

Fig. 5.18 Simulated and measured beam phase space for point 2. a) is the measured phase space, while b) is the simulated phase space

In order to do a quantitative comparison, the x distributions (simulated and measured) of the phase spaces were analyzed and reported in Fig. 5.19. The red and the blue markers are the simulation and experimental data respectively. Despite the over-estimation of the tails, the agreement between the measurement and the simulation works quite well despite the multitude of approximations done. The rms of the distributions are 9.6 mm and 13.4 mm for the experiment and simulation respectively.
It is possible to identify a core part which follows a waterbag distribution while the tale component can be represented by a more wide distribution.

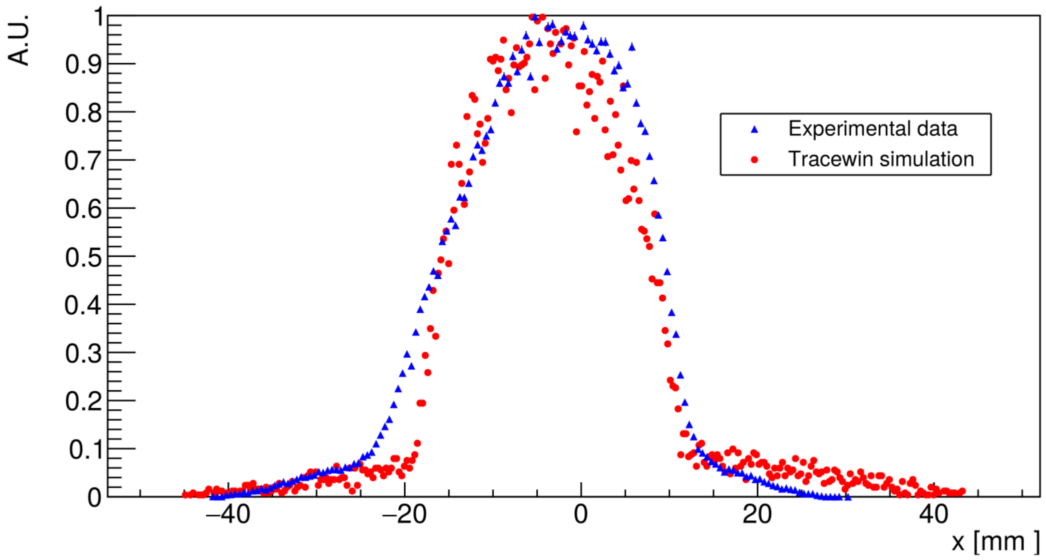

Fig. 5.19 x profiles of the experimental and simulated 55 mA 50 keV H$^+$ beam, with the solenoid couple $(135, 150)$ A. the blu points are the experimental data, while the red markers are the simulation data.

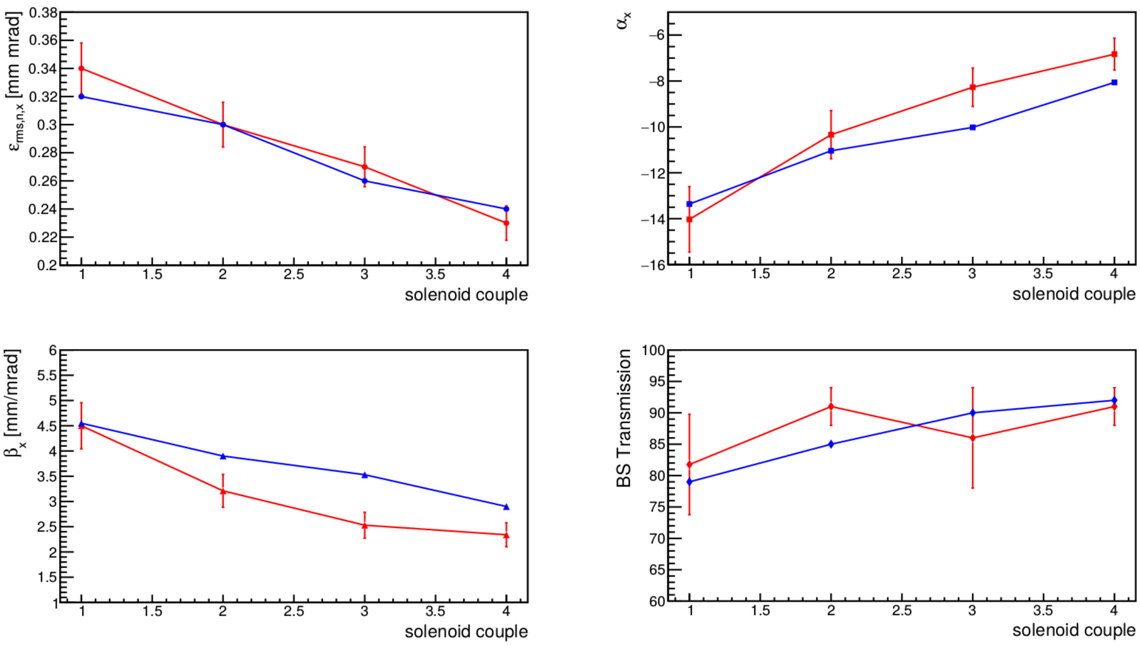

Fig. 5.20 The 4 plot shows the comparison between the simulation and the measurement (blue and red respectively): $\varepsilon_{\text{rms,n,x}}$, α_x, β_x and the BS transmission are shown.

Finally, the results on the 4 points are shown in Fig. 5.20. The measurements are taken at the Allison scanner position. The simulations and the measurements (blue and red respectively) show an increasing of emittance and a corresponding growth of β_x and α_x; it indicates a stronger focus performed by the solenoids in the region of the RFQ injection.

The larger differences affects the Twiss parameters, which are very sensitive to the s.c.c. modeling. However, a good level of agreement is reached. Thus, the model obtained allows deeper study of the main characteristics of the rms quantities evolution along the transfer line physics.

Trend of the parameters with different solenoid couples

The s.c.c. zones, centered on the experimental measured points (see Fig. 5.13), were analyzed in order to characterize the beam behavior: the objective was to estimate the Twiss parameters and emittance at the entrance of the RFQ.

Each area represents a type of injection optics: the main interest for the injection into the cavity are the zones which lay on the imaginary line from the upper left to the lower right corner, i.e. following the experimental points $1-4$. Fig. 5.22 shows the $\varepsilon_{\mathrm{rms,n,x}}$ iso-lines as well as the relative mismatch ($< 100\%$) to the RFQ beam input. The values were taken at the RFQ injection.

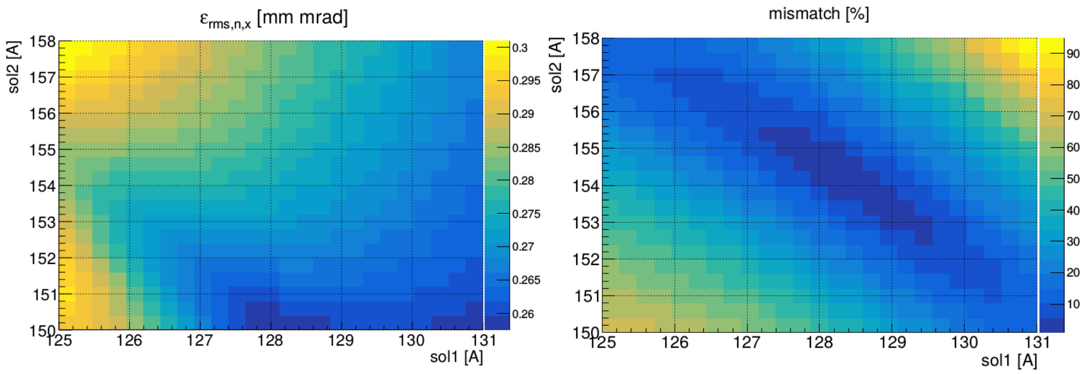

(a) (b)

Fig. 5.21 Matching area. Emittance and mismatch vs solenoid couple of 55 mA at 50 keV H^+ at RFQ injection. a) shows the emittance trend, while b) shows the mismatch

Despite the complex pattern followed by the function $\varepsilon_{\mathrm{rms,n,x}}$(sol1,sol2), it is possible to notice an increase of the emittance from lower right to upper left corner, as foreseen in the preliminary model. All the three zones are mainly covered by an $\varepsilon_{\mathrm{rms,n,x}} < 0.3$ mm mrad. The area which shows a value larger than the limit is centered on point 1 (see Fig. 5.13), when the ratio of the beam radius and the bore is maximum.

The minimum mismatch zone is located in the upper left corner of 5.13, which means solenoid 1 strength smaller the solenoid 2, as foreseen by the preliminary model (point 2).

Once the smaller mismatch area is identified, the results for emittance and mismatch are studied for this zone (Fig. 5.21) at RFQ injection.
While the minimum of the mismatch is centered in plot (b) 5.21, the emittance (a) is almost monotonically decreasing from the upper left to the lower right corner. The emittance ranges from $0.3-0.26$ mm mrad. The RFQ transmission of this area was tested and the result are shown in the next section.

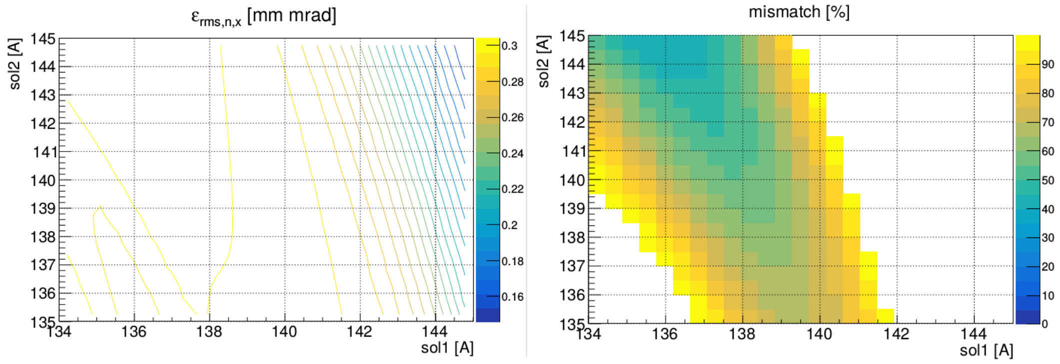

(a) point 3 (b) point 3

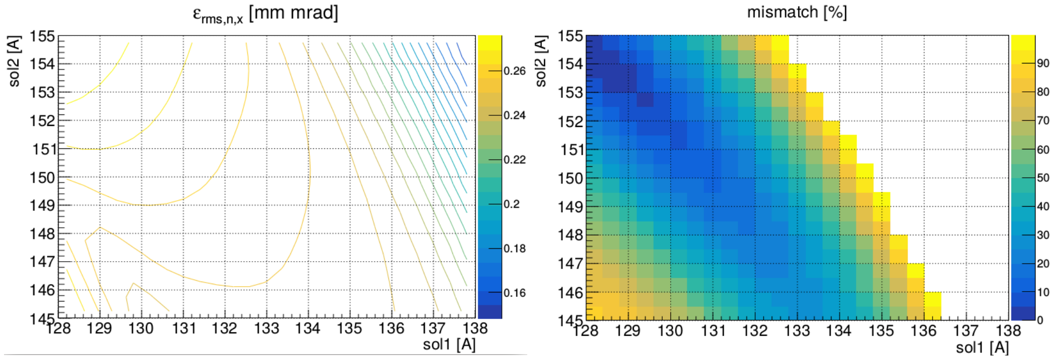

(c) point 2 (d) point 2

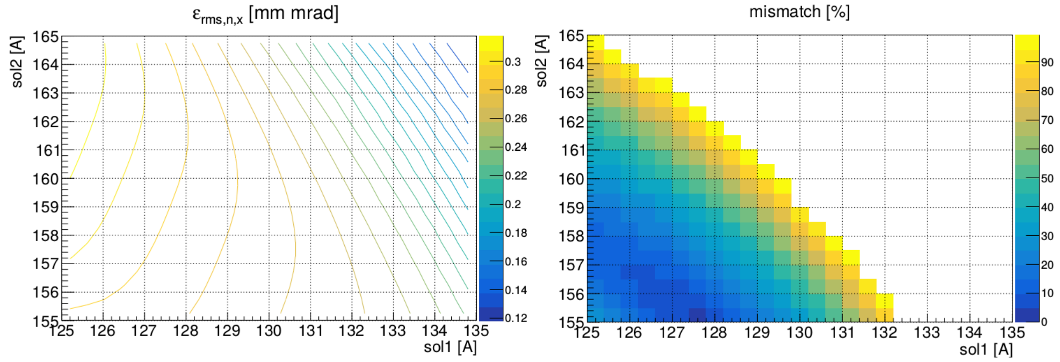

(e) point 1 (f) point 1

Fig. 5.22 Matching area, emittance and mismatch vs solenoid couple of 55 mA at 50 keV H$^+$ at RFQ injection. a), c), e) are the emittances centered at 3, 2, 1 points. b) d) f) show the mismatches

5.3.3 Acceleration with the RFQ

The particular of the interface between the LEBT and RFQ is shown in Fig. 5.23. The RFQ is modelled with TOUTATIS software [15]. The discontinuity as the one between the end of the cone and the RFQ is due to the visual match of the Tracewin-TOUTATIS software.

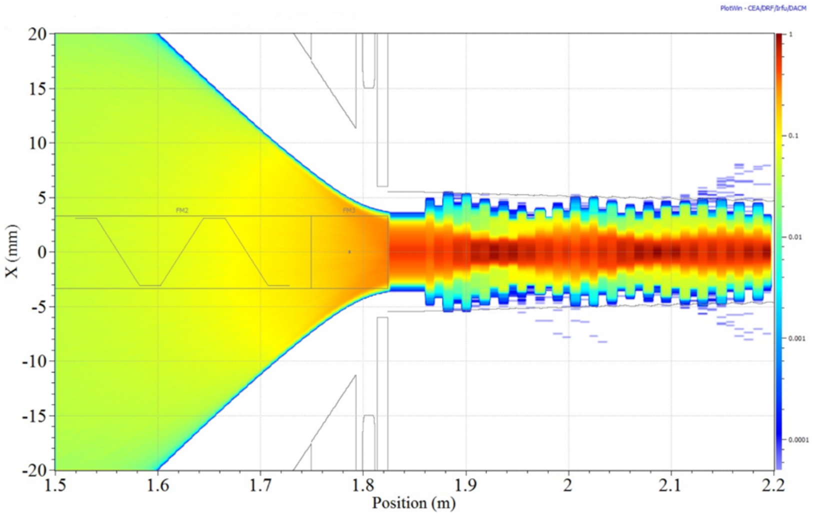

Fig. 5.23 Particular of the injection into the RFQ of a 55 mA H^+

The RFQ model includes the as built geometry (electrodes and modules real positions) and the after-tuning voltage profile [39]. The interest in this case is to study the output performance of the RFQ respect the beam input mismatch and emittance.

The RFQ output beam will be transported with the MEBT transfer line up to the beam dump during the commissioning phase. The resulting overall system transmission contains the information on the RFQ transmission, which needs to be decoupled from the other subsystems (i.e. LEBT and MEBT).

The previous sections explored the relation between the LEBT settings and the input beam at the RFQ. In the following section, the RFQ behavior respect to the LEBT setting will be studied. The (b) plot shown in Fig. 5.24 refers to the transmissions of the RFQ as a function of the solenoids strength. It is interesting to notice how it is possible to obtain a large transmission with a larger mismatch (than the minimum), following the low mismatch "valley" along imaginary bisector from upper left to lower right.

The effect is mainly due to the direction of the mismatch "valley" in the solenoids plan (a) plot: it still maintains a low sustainable mismatch to the RFQ (i.e. $< 20\%$) and at the same time decreases the emittance value (from 0.29 mm mrad down to 0.26 mm mrad), as shown in Fig. 5.25. In the transmission calculation shown in plot (b) 5.24 only the accelerated

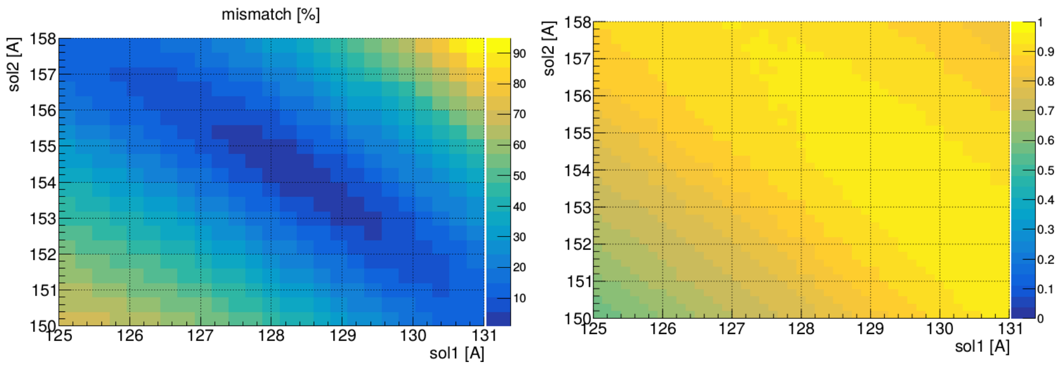

(a) (b)

Fig. 5.24 a) Mismatch at the RFQ injection point. b) Transmission of the RFQ at its output. The not-accelerated particles are considered as losses.

particles are taken into account (i.e. the particle that belong to the energy range 2.5 ± 0.150 MeV).

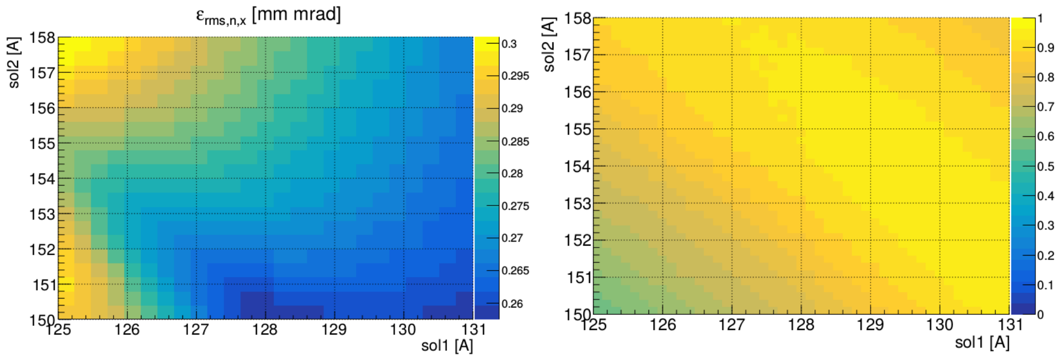

(a) (b)

Fig. 5.25 a) $\varepsilon_{\text{rms,n,x}}$ mm mrad at RFQ injection point. b) Transmission of the RFQ at its output. The not-accelerated particles are considered as losses.

The resulting maximum transmission is 93%, at $(151, 130.8)$ A solenoid 1 and 2. At the minimum mismatch point (but large emittance) $(154, 128.5)$ it results 90%. The previous plots show the strong correlation of the RFQ respect to LEBT input beam. Understand how strong is the dependence of MEBT respect to the RFQ output is also a key point for the beam commissioning and experimental data interpretation. Therefore, it is worth to study the sensibility of the RFQ output beam parameters with respect to the nominal LEBT-RFQ dynamics. In particular, for this case, the focus is on transverse emittance and Twiss, Fig. 5.26. The mismatch is defined now respect to the nominal output RFQ beam parameters at the maximum transmission point.

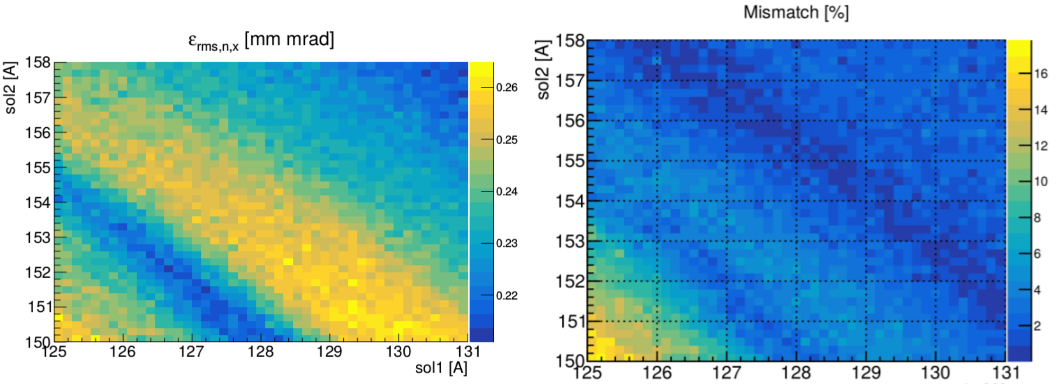

(a)

(b)

Fig. 5.26 a) $\varepsilon_{\text{rms,n,x}}$ mm mrad at RFQ exit b) Mismatch respect to the RFQ output Twiss of the maximum transmission point.

The emittance ranges from 0.27 up to 0.21 mm mrad, while the mismatch is generally smaller than 8%. As far as the solenoid couples move closer to the lower right corner, the transverse emittance increase from 0.24 to 0.26 mm mrad. In conclusion, if the solenoid strengths vary within 10% the matching point, the RFQ output beam does not change drastically its characteristics.

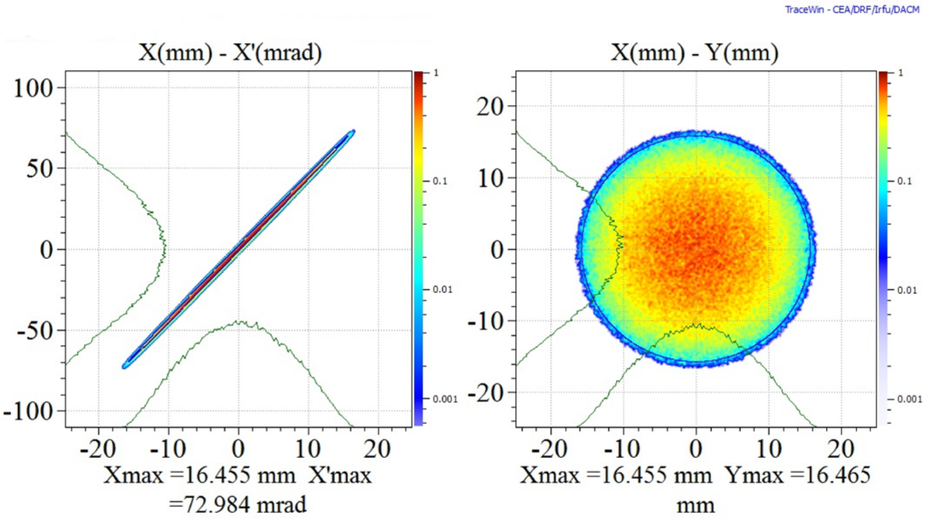

Fig. 5.27 Transverse planes at the LEBT simulation input

Therefore, during the commissioning the MEBT quadrupoles can be set with their nominal tuning, due to the fact that is not strongly varying with the RFQ output.

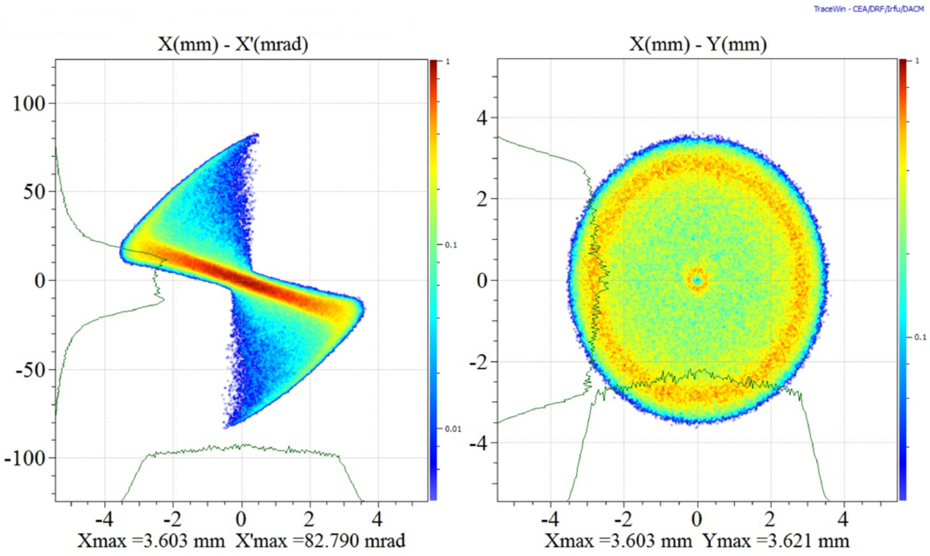

Fig. 5.28 Transverse planes at the RFQ input

In order to study with higher precision the maximum transmission point found, the number of macro-particles was increased up to 3×10^5. The mesh was adjusted accordingly [36].

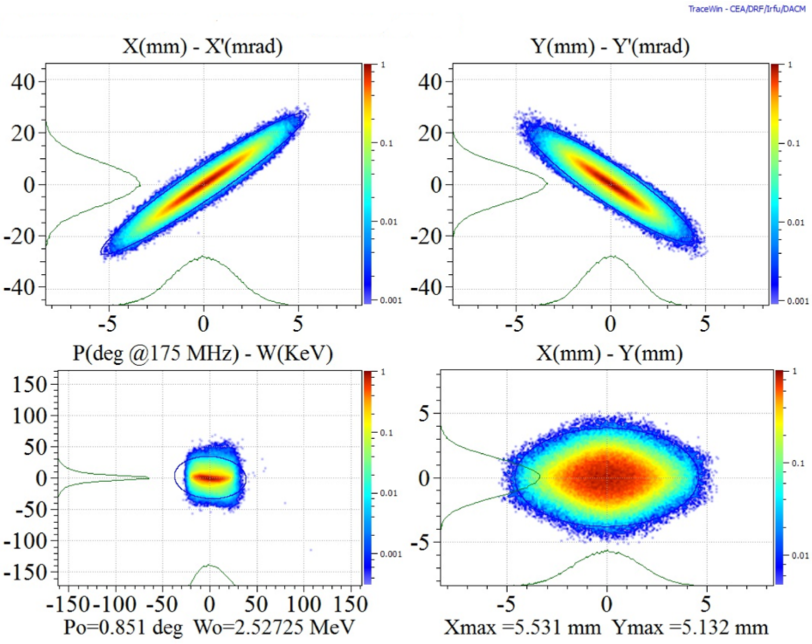

Fig. 5.29 Transverse and longitudinal planes at the RFQ exit are shown

The input beam transverse spaces at LEBT start are shown in 5.27. No deformation of the phase spaces can be seen due to the fact that distribution is generated *ex novo* with a parabolic distribution (as it was done for the trace-forward method).

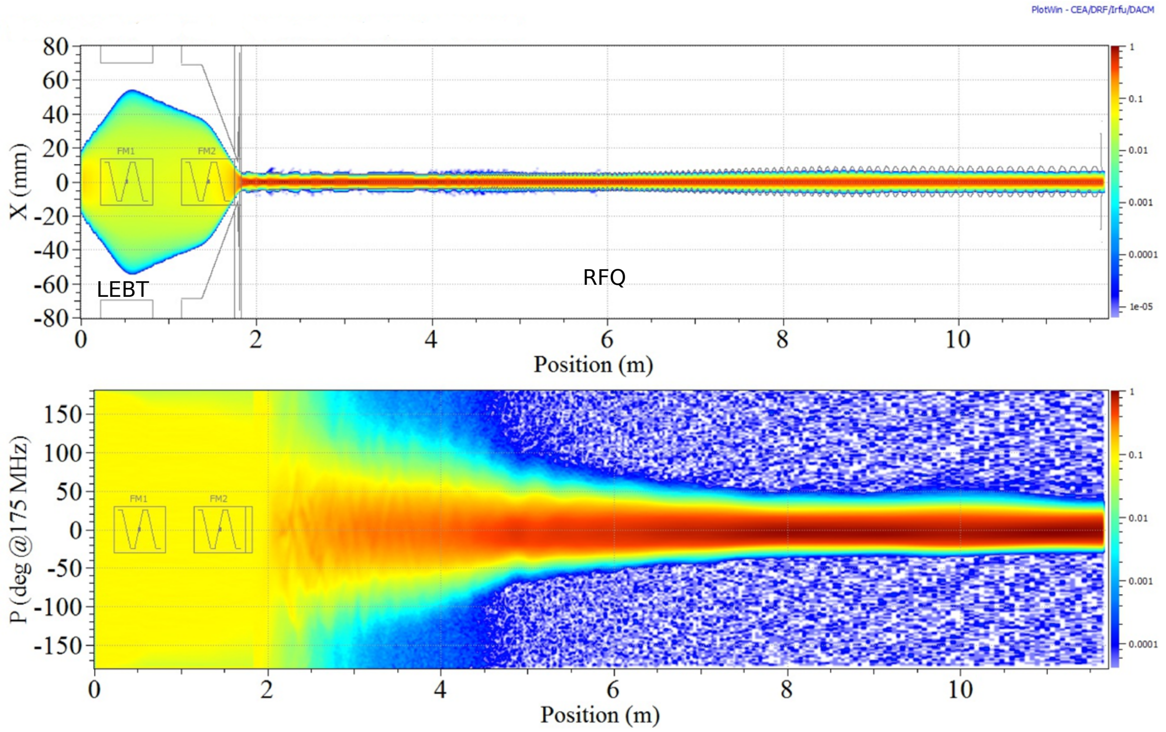

Fig. 5.30 xz and Φz planes of 55 mA beam 50 keV transport and acceleration through the RFQ. The not accelerated particles are excluded.

On the contrary, the spatial distribution of the beam at the RFQ input (see Fig. 5.28) shows concentric structures due the non-equilibrium state reached after the interaction between the solenoid focusing channel and the space charge. The same behavior will be seen in the next chapter, when a self consistent software will be used. The phase spaces at the output of the RFQ are displayed in Fig. 5.29. In 9 m of strong focusing channel, the system relaxes and reaches an equilibrium state.

This fact will be confirmed by the emittance trends. The effect consists in a re-organization of the phase space distribution: the particles out of the acceptance or which oscillations grow (due for example by the excitation of the breathing and quadrupole modes due to the mismatch) on the first meters are lost on the RFQ copper.

Fig. 5.30 shows the H^+ particle density on the xz and r plane for the LEBT and RFQ complex. The Φz plane shows the bunch formation, from $\pm180^o$ (coasting beam) to $\pm20^o$. The non-accelerated particles (about 5% of the input beam) are excluded in both the plots.

Table 5.6 Rms quantities of the beam at LEBT input, RFQ injection and RFQ exit

Parameters	LEBT input	RFQ injection	RFQ output
$\varepsilon_{\text{rms,n,x}}$[mm mrad]	0.05	0.26	0.24
β_x[mm/mrad]	8.80	0.12	0.76
α_x	-39.00	1.17	-3.64
$\varepsilon_{rms,\Phi w}$[deg MeV]			102.61
$\beta_{\Phi w}$[deg MeV]			1.13
$\alpha_{\Phi w}$			0.07

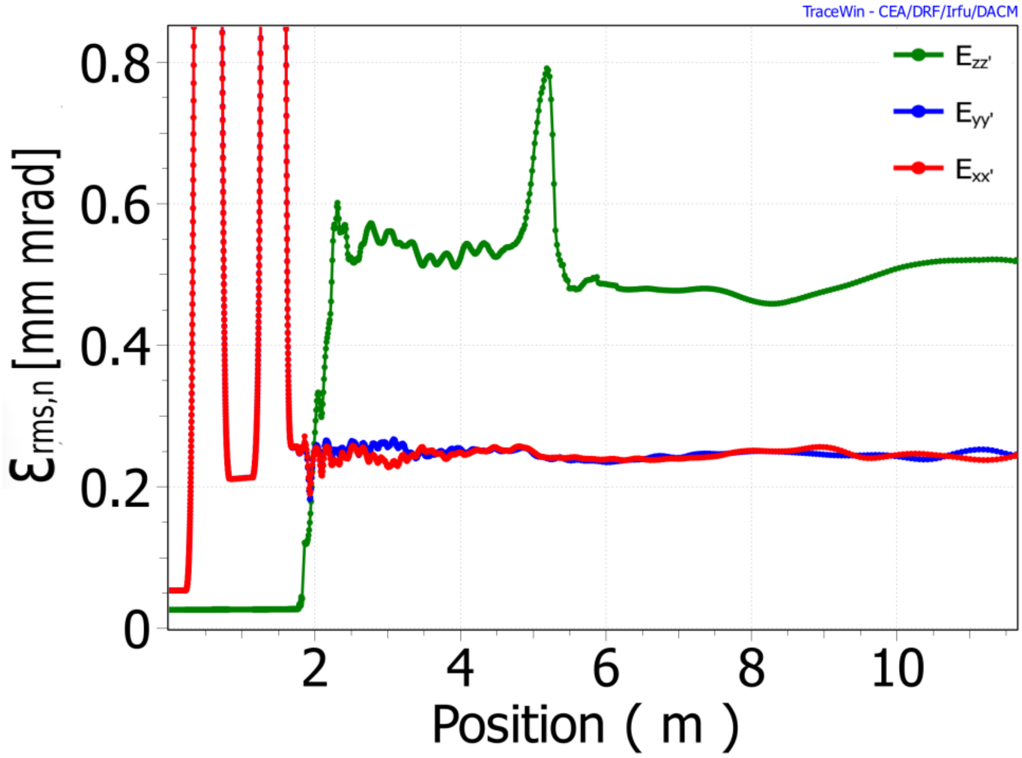

Fig. 5.31 Emittance trend of 55 mA beam and 50 keV energy transport and acceleration. The red and blue curves are the x and y transverse emittance, while the green curve is the longitudinal emittance

The beam parameters at the beginning of the simulation, at the RFQ injection and output are reported in table 5.4. The emittance trends along the LEBT and RFQ are displayed in Fig. 5.31. The blue and red curves are the transverse emittance, while the green curve is the longitudinal emittance. After solenoid 1 there is a first emittance growth due to the space charge and applied field non-linear focusing. At the entrance of the RFQ, the longitudinal structure of the beam starts to generate, as well as the longitudinal emittance.
Due to the not perfect matching, the transition between the two different focusing (the solenoids and the RFQ) excites the space-charge waves in the beam distribution (see Fig. 5.28), which led to rapid oscillations and distribution deformations.

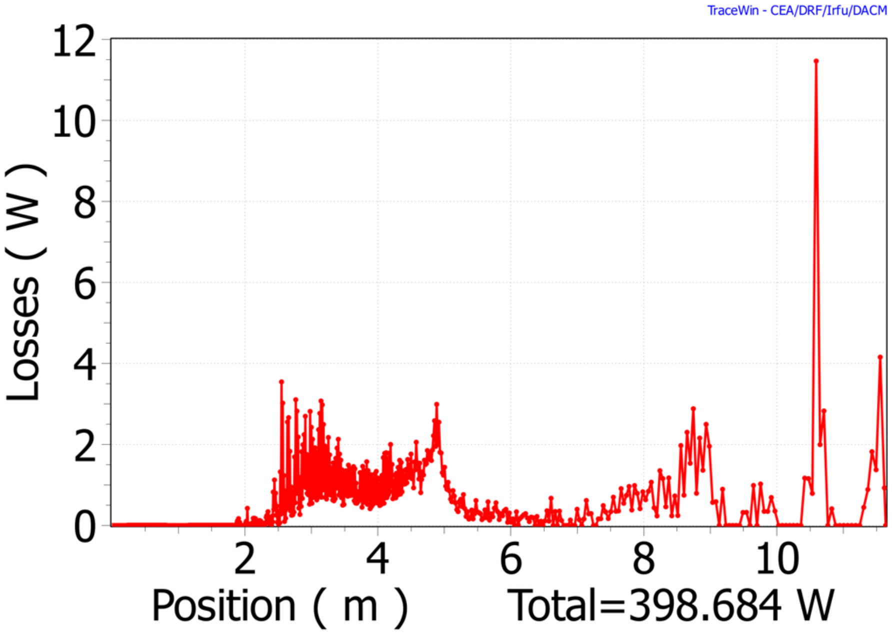

Fig. 5.32 55 mA H^+ 50 keV beam power deposition along the LEBT and RFQ. The larger peak at 11 m is due to construction errors.

As far as the system relaxes, (after the first 2 m of RFQ), via losses or re-distribution, the emittance trend stabilizes in its final values. The particle losses are located at the low energy section of the RFQ, in such a way to reduce the power deposition due to particle collisions. The power deposited is shown in Fig. 5.32. As far as the accelerated particle reaches the high energy section, it gains energy, and therefore the loss of few particles causes a larger power dissipation on the RFQ copper.
Some peaks due to accelerated particle lost are present in the final part of the RFQ. However, the total power lost (in case of CW beam) is 396.7 W, mainly located at low energies, as expected.

5.3.4 Conclusions and limitations of the model

The model is limited by two type of approximations:

- physics representation: constant s.c.c. along z and r, input beam distribution which does not belong to the plasma meniscus formation process and non-linearities of the extraction, single species transport.
- hardware errors: misalignment of the solenoids/emittancemeter/cone, solenoid field settings etc. All of these effects are not included in this model.

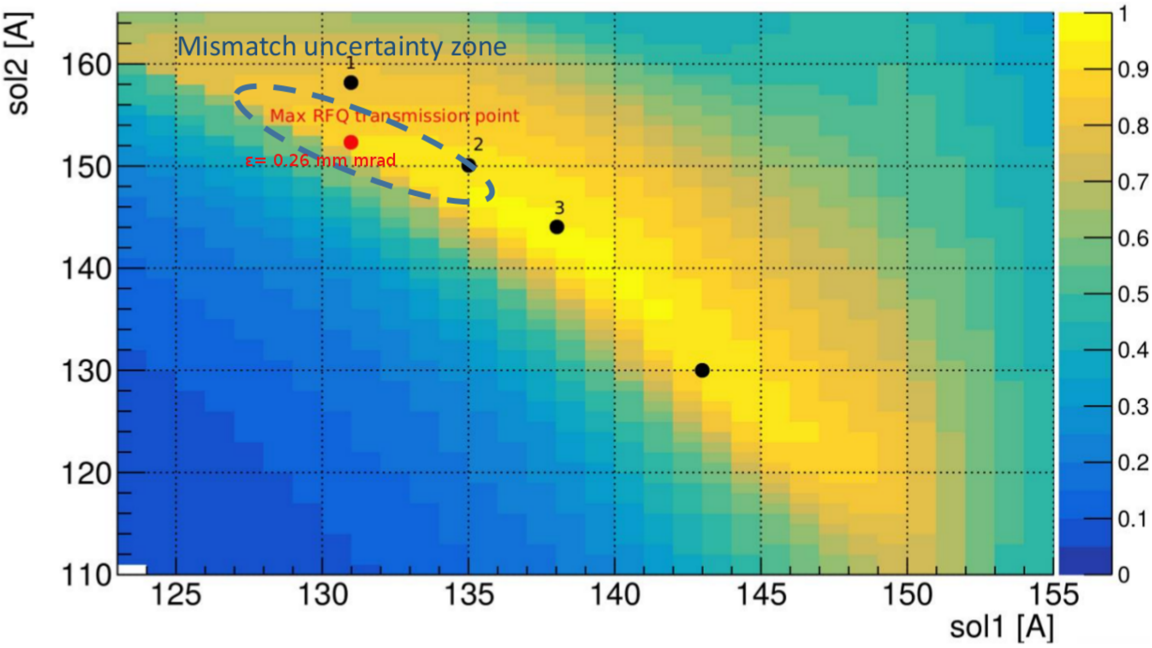

Fig. 5.33 Experimental solenoid scan plot of 55 mA H^+ 50 with the resulting estimated area with low mismatch RFQ input beam. The maximum transmission point is also shown

Despite all these approximations, for the studied beam H^+ $65-55$ mA at 50 keV the model was able even to reproduce with a good accuracy the spatial distribution at the emittancemeter. The uncertainty on the RFQ matching point can be estimated by the deviation between the experimental and simulation shown in Fig. 5.20. Since point 3 exhibits the largest differences in Twiss, the relative deviations were applied to the RFQ nominal input parameters and the mismatch was calculated. Two deviations were taken into account: $(\beta_{\mathrm{exp}} \pm \sigma_{\mathrm{err}}\beta_{\mathrm{exp}}) - \beta_{\mathrm{sim}}$. The maximum deviation (+ contribution) results in a mismatch of 36%, while, for the minimum (− contribution) is 18%. The maximum mismatch was chosen as error.

Another uncertainty belongs to the longitudinal dynamics treatment of TraceWin in case of strong coasting beam focus. As shown in Fig. 5.8 there is an exchange between longitudinal and transverse emittance which are related to the number of simulated macroparticles.
The induced error on the Twiss calculation between 10^4 and 10^5 number of macroparticles is about -6.3% of the value. This uncertainty is not symmetric: it always moves the matching point closer to the lower right part of the plot (i.e. less divergence and large beam at the emittancemeter). Adding this error, the resulting mismatch area related to uncertainty increases up to 41% (in mismatch). The estimated area has a rough elliptical shape and it is shown in 5.33. Each area width and position is indeed strongly dependent on all the line characterization and, as seen by the preliminary model, on the output source Twiss parameters.

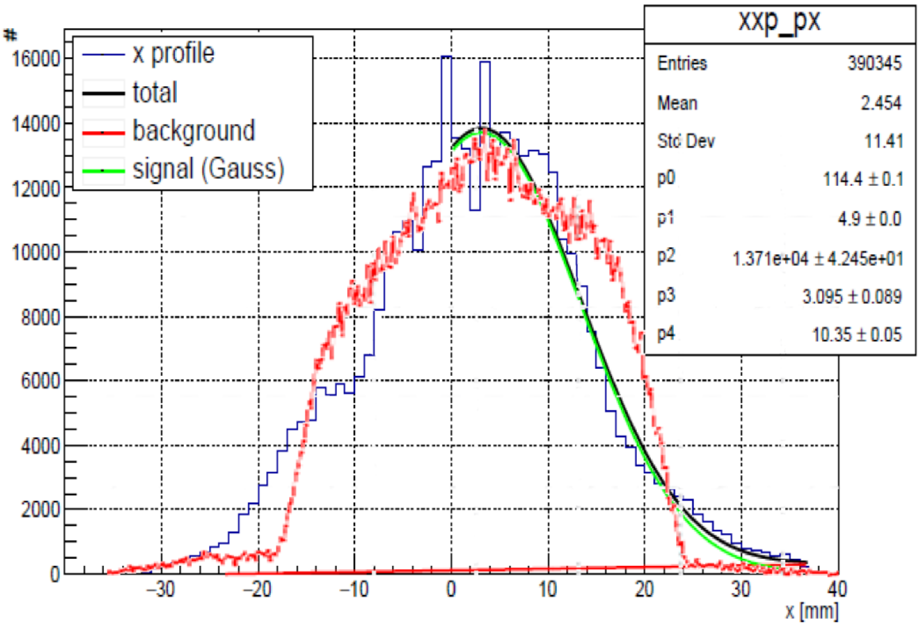

Fig. 5.34 x profile of 133 mA deuteron beam at 100 keV with trace-forward results comparison, done with Tracewin. Red curve is the Tracewin obtained profile, the blue histogram are the experimental data. Other fit are shown

The absolute s.c.c. values obtained by the trace-forward do not only depend on the real neutralization but also by the approximation of the spatial beam input distribution. They are strongly related to the concept of equivalent beam transport. Therefore, if a more realistic s.c.c. compensation trend is required, another software shall be used. The problem arises when the transfer line is not emittance dominated for the large part of the transfer (such as the proton case studied) or/and in the nonlinearities from the source modify strongly the input distribution. Some inconsistencies may be obtained, such as too large exaggerate tales.

It is possible to recover partially the resulted inconsistency with a different software with a more accurate implementation of the compensation process.
Fig. 5.34 displays this fact: a *x* profile of a deuteron beam of 133 mA at 100 keV is shown (blue histogram). The red curve reports the trace-forward estimated profile with Tracewin, normalized on the experimental max number of entries. Other fits are shown. The trace forward tried to stretch the core-tale distribution in order to match the rms quantities. However even if they are matched to the rms values (which is the objective of the method), the spatial distribution is not well reproduced

Chapter 6

Rms trace-forward method with dynamic s.c.c.

6.1 Introduction

In the previous chapter the trace-forward method was tested and its limitations were analyzed. In order to obtain a more self-consistent model for the deuteron beam (larger perveance than proton beam), the WARP code was utilized.
3d simulation were used in order to reproduce and predict the characteristics of the beam transfer in the LEBT.

6.2 Rms trace-forward method application to LEBT

The rms trace-forward method applied can be simplified due to the smaller number of approximations with respect to the previous chapter.

- the space charge compensation is a result of a Monte-Carlo process where each particle is generated via a defined cross section which depends on the energy of the incident particle.
- The secondary particle is governed by the self and applied field.
- the WARP code can transport multiple species.

This modelization of the dynamic space charge compensation requires extremely time demanding simulations with serial core processing. In order to reduce the time needed for a run, the parallelized version of the software was used: the 2 m length simulation was subdivided in 20 longitudinal domains (the max core number at disposal of the machine). Still the simulations required more than one month in order to be performed.
The forward-method in this framework does not foresee any arbitrary change of neutralization level. It will be determined by the process itself.

1. First set of $\varepsilon_{\mathrm{rms,n},x}, \alpha_x, \beta_x$ was calculated via the AXCEL software. The rms quantities were assigned to a parabolic beam distribution placed at the extraction column repeller position.
2. All the line optical elements such as the solenoids and the repeller were set as in reality, with the same applied field.
3. The distribution is transported up to the emittancemeter. If the parameter triad agrees within 30% and the simulation current within 20% the mean value of the error bar, the method proceeds with the next measured point. If not, only the Twiss parameters and the emittance are changed.
4. When a rough agreement is obtained, the process is concluded.

6.3 Experimental input point

The beam studied is a 155 ± 5 mA D^+ at 100 keV. From the Doppler Shift measurement, the D ratio respect D_2^+ is 93 : 7. Since the production of secondary electrons depends on the gas type [40] (and the number of scatter centers), the measurement of the residual gas analyser was taken into account: between the two solenoids the partial gas pressure resulted almost 6.5×10^{-6} mbar D_2 and 6.5×10^{-6} mbar Kr; after the cone, in the second diagnositic chamber the vacuum was degraded from 10^{-7} mbar to 3.6×10^{-5} mbar, injecting Kr. Thus, the situation is very different compared to the proton point; however there will be still an effect of the emittancemeter on the induced space charge compensation after the cone, as seen by the previous study.

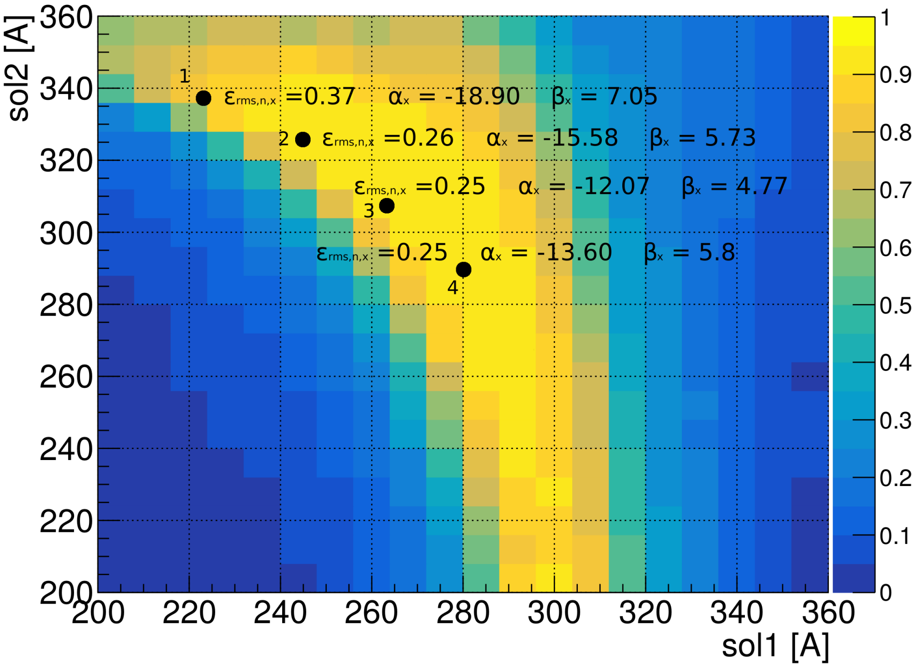

Fig. 6.1 Measured transmission from the extraction to the BS and $\varepsilon_{\mathrm{rms,n},x}$ vs solenoid 1 and solenoid 2 currents for 155 mA 100 keV D beam. The four measurements of the emittance, taken at the emittancemeter position used for the trace-forward are reported.

Also in this case there is a trend on the emittance: the maximum value is located in the upper left corner. However, differently from the proton point, there is not a large variation going to the lower right corner. There is an asymptote value around $\varepsilon_{rms,n,x} = 0.25$ mm mrad after point 1. This can be explained with a lower effect of the non-linear focus of the solenoids, due to the smaller r_s/a (solenoid radius/ beam radius) respect to the proton beam dynamics of the previous chapter. The expected generalized perveance ranges from 3.9×10^{-3} (135 mA deuteron beam) to 4.5×10^{-3} (158 mA given by D^+, D_2^+ and D_3^+) in the extraction region. Compared to proton point studied in the previous chapter, the nominal beam perveance is 20% higher, thus will dominate the beam transport.

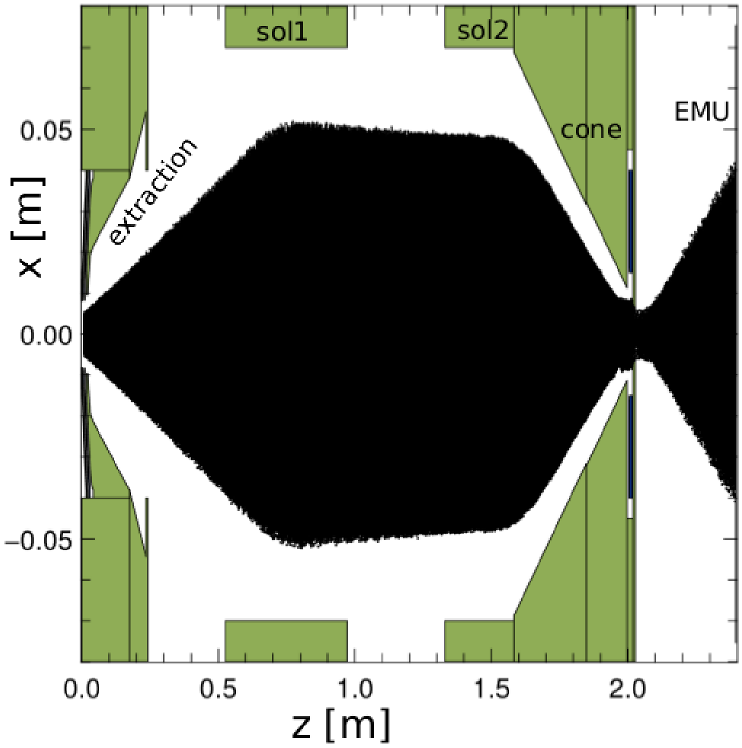

Fig. 6.2 WARP model of the IFMIF LEBT

6.4 Simulation model

The simulation consists of 2.397 m long LEBT, starting from the repeller electrode up to the emittancemeter. The repeller electrode is critical for the simulation, because it contributes to the longitudinal boundary of the electrons and cannot be neglected. The initial guess for the beam Twiss were obtained via AXCEL simulation which stops at the repeller position. The WARP software simulates the beam propagation through the LEBT. It was decided to use the multigrid Poisson solver routine in order to manage the space charge beam dynamics. All the simulation were preformed with full 3d geometry in order to check if the formation of circular structures in the spatial domain shown in Fig. 5.28 is an artifact of the simulations.

6.4.1 Mesh and macro-particles per bunch

The mesh size along the simulation is fixed. There are two criteria in order to determine the cell volume: keeping the number of macroparticle per mesh fixed, in order to avoid simulation noise and, at the same time, ensure as much as resolution possible to resolve the space-charge waves.

In order to do so, there are 3 levels of mesh refinements were chosen: the minimum transverse mesh size is 250 μm in the cone hole region (500 μm in z-direction), where the maximum is 4 mm near to the border of the simulation.

It is important to compare the mesh size with the Debye length, in order to check how far the model is from resolving the space-charge phenomena. The more demanding part is close to the rfq cone. The calculation is taken at the steady state. Considering $I_{\mathrm{D}} = 135$ mA, the residual electron temperature between $5 - 15$ eV (since the major contribution to electron temperature is supposed at the steady state to belong from the residual potential hole of the beam, given from the FGA measurement), $\varepsilon_{\mathrm{rms,x}} = 25.00$ mm mrad, it is possible to calculate the λ_{D}. The ion temperature is given by [6] and reported in Eq. 6.1:

$$T_{i,\perp} = \frac{(\beta c)^2}{k_{\mathrm{B}}} \gamma m \left(\frac{\varepsilon^2_{\mathrm{rms,x}}}{\langle x^2 \rangle} \right) \tag{6.1}$$

The ion density n_i is approximated to be uniform. Thus, n_i can be calculated as:

$$n_i = \frac{\lambda_q / e}{\pi a^2} = \frac{I / e\beta c}{\pi a^2} \tag{6.2}$$

where λ_q is the linear charge denisty. n_i results 9.6×10^{15} m^{-3}, and following $\langle x^2 \rangle = 1.7$ mm at RFQ injection. In conclusion, Eq. 6.1 gives $T_i = 4.8 \times 10^5$ K. The electron temperature is $T_e = 1.7 \times 10^5$. Therefore, at the cone injection $\lambda_{\mathrm{D}} = 3.4 - 2.6 \times 10^{-4}$ m depending on the solenoid focusing. The ratio between the Debye length and the minimum mesh size is $1.36 - 1.0$ and it is maintained as much as possible constant along the line.

In order to reduce the time needed for each run, the number of macroparticle of the primary beam (D$^+$ particles) per $\beta\lambda$ was set approximately 30000, injected with a parabolic distribution at the repeller position.

The last parameter to set was the time step for the integration. It was set to $dt = 20$ ps in order to avoid multiple cell cross in one time step by macroparticles. The fastest particle type in the simulation is the electron: assuming 1.250 kV (max potential of the cone repeller without beam at extraction cone radius) as maximum energy, the longitudinal distance traveled by the electron in one time step is 419 μm which is smaller than the smallest longitudinal mesh refinement. Moreover, the dt chosen is enough to resolve the space charge waves, compared to the estimated ω_p.

6.4.2 Boundary conditions

The WARP software is a finite element multigrid Poisson solver. Therefore, in this model, the beam dynamics of the electrons depends on the boundary conditions and the groundings which surrounds the beam.

There are two diagnostic chambers and one aperture after the extraction region which modifies the ground profile. Due to the very large pipe radius (> 190 mm) respect to the mean drift bore (70 mm), it was decided to apply Neumann condition at slightly larger aperture (see Fig. 6.2). Also the beam cone was carefully modelized in order to correctly represent the boundary.

This choice allows to save computation time thanks to lower number of mesh cells. It is important to notice that the geometry of the diagnostic boxes apertures does not fit the cylindrical symmetry; on the contrary of all the other surfaces.

6.5 Secondary electron formation

In this model, two mechanisms for the electron generation were considered: the gas ionization and the secondary electron generation due to ion collisions.

At each step, the Montecarlo process calculates the ion and electron generation due to gas and collision phenomena, given the cross section by the user. Once the macroparticles are generated, the softwares calculates the overall charge density and applies the self/applied fields to each particles, starting again the process.

6.5.1 From residual gas

The vacuum of the LEBT line ranges from 10^{-6} to 10^{-5} mbar. In other parts of the LEBT, such as in the second diagnostic chamber it was degraded from 10^{-7} mbar down to the above values, in order to take advantage of the ionization process, supplying electrons for the space charge compensation.

The time needed for the neutralization can be estimated by the formula 2.26, for a uniform cylindric charge density. The σ_i values for many gas types at different proton energy can be found in [12, 41]. For the typical gases type in the LEBT, such as H_2, O_2, Kr the cross section for H^+ at 50 keV are respectively 2.12×10^{-20} m^2, 5.18×10^{-20} m^2, 8.13×10^{-20} m^2.

Also the electrons undergo to ionization process with the residual gas. For Kr ionization the maximum of σ_e is located around the 100 eV, and it is generally smaller than σ_i: for example, while Kr gas $\sigma_{e,max} = 4.0 \times 10^{-20}$ m^2, the $\sigma_i = 8.13 \times 10^{-20}$ m^2 for deuteron beam, at 100 keV. Despite the smaller values, the phenomena has same order of magnitude of the ion case and cannot be neglected, as Fig. 6.3 shows.

The residual gas components taken from RGA measurements during commissioning campaign were implemented in the simulations. The process taken into account are listed below (the same applies for the d_2 gas):

$$\begin{cases} D^+ + Kr \to Kr^+ + e^- + D^+ \\ D_2^+ + Kr \to Kr^+ + e^- + D_2^+ \\ D^+ + D_2 \to D^+ + e^- + D_2^+ \\ D_2^+ + D_2 \to D_2^+ + e^- + D_2^+ \\ e^- + D_2 \to D_2^+ + e^- + e^- \\ e^- + Kr \to e^- + e^- + Kr^+ \end{cases}$$

The cross section semi-empirical formula related to the electron ionization by ions is given by reference [42] while in case of electron ionization by electrons the semiempirical formula refers to reference [43].

These formulas were implemented into the WARP script in order to simulate correctly the ionization process. In particular, in case of electrons, it is important to correctly fit the experimental data in the whole energy range of the incident electron, in order to correctly follow the transient in the s.c.c., when the electron energies may have larger energies respect to some tens of eV. Indeed, at the beginning of the s.c.c. process the un-neutralized potential can increase the electron energy of more than 1 kV, while, at the steady state the electron energies are mainly given by the residual potential hole (5 – 15 eV).

The gas pressure is assumed to be constant along the line. The scatter centers are deposited on the mesh grid: once the ionization process occurs, the secondary particles are emitted with 5 eV kinetic energy Gaussian distributed. The velocities are random distributed in xy plane with a small longitudinal component. In order to speed up the calculation time, the gas pressure was doubled for both the vacuum region (LEBT and second diagnostic part).

6.5.2 Collisions

The electron production due to collisions is not a negligible process: as an example, for H^+ beam at 50 keV is $\gamma = 1.57$ onto SS, which means that, in average, there are 1.57 electrons per proton incident. The modeled processes involve the collisions of the beam ions (D^+ and D_2^+) and electrons with the beam pipe SS, with the cone Cu and with the tungsten shield of the emittancemeter (see Fig. 3.13). The interactions are listed below:

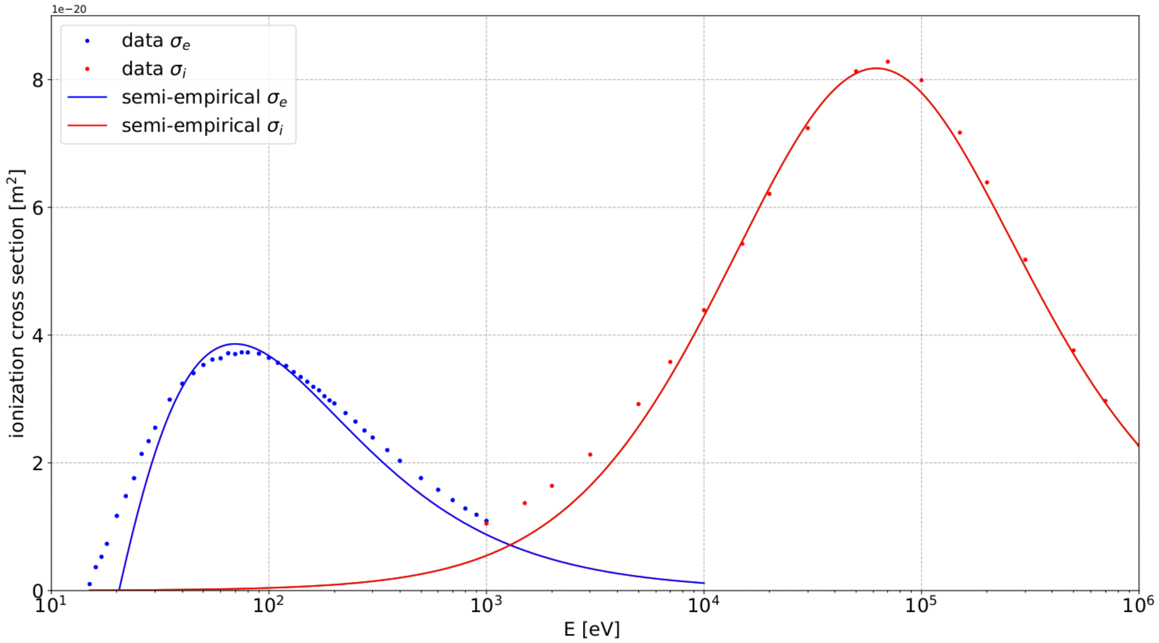

Fig. 6.3 Kr ionization cross section vs incident particle energy. The red is the total cross section for the ions. The blue is the total cross section for the electrons

$$\begin{cases} \mathrm{d}^+ + \mathrm{SS/Cu} \rightarrow e^- \\ \mathrm{d}^+ + \mathrm{W} \rightarrow e^- \\ \mathrm{d}_2^+ + \mathrm{SS/Cu} \rightarrow e^- \\ e^- + \mathrm{SS/Cu} \rightarrow e^- \end{cases}$$

Briagiola's paper [13] shows that γ (electron yields) of D$^+$, H$^+$ and D$_2^+$, He$^+$ (in energy range $1-100$ keV) collisions on several the metallic compounds (Li, Al, Cr, Cu, Ag) have the same energy dependence as that for the electronic stopping power (or inelastic stopping power).

If the electronic stopping power is the main mechanism of energy loss within the specified energy range (respect to the elastic stopping power due to ion recoils), it is possible to estimate the secondary electron emission following the procedure written in reference [44]. $\gamma(E)$ can be calculated via:

$$\gamma(E) = 0.14 C_b \frac{dE}{dx} \tag{6.3}$$

where C_b is the efficiency relative to protons for converting energy lost in a materials to electrons and dE/dx is the average energy loss per unit length. It is possible to obtain the $\frac{dE}{dx}$ curve respect the ion energy E via SRIM [45] simulation considering normal incident ion onto the chosen compound (such as stainless steel). The results are then translated via 6.3. The C_b parameter is adjusted in order to reduce as much as possible the difference with the data taken in reference [13] and the model based on SRIM. The result is shown in table 6.1

Table 6.1 Comparison between Eq. 6.3 and experimental values reported in [13] for D at 100 keV.

Material	$\gamma_{D,exp}$	$\gamma_{D_2,exp}$	$\frac{dE}{dx}_{D,SRIM}$ [eV/A]	$\frac{dE}{dx}_{D_2,SRIM}$ [eV/A]	$\gamma_{D,calc}$	$\gamma_{D_2,calc}$
Al	1.38	0.96	12.59	11.00	1.15	1.08
Cu	1.57	1.08	17.44	14.38	1.59	1.41
Cr	1.42	1.01	21.71	15.60	1.98	1.53
Au	2.15	1.70	17.22	13.13	1.57	1.29

The C_b value results 0.65 for deuterons, while 0.70 for di-deuterons. The routine used in order to implement the emission of secondary electrons is POSINST [46], which treated the yield of secondary electron with a specific expression reported in [44].

Fig. 6.4 shows the SRIM data for the deuterons onto W and SS, as well as the fitting function for the implementation in POSINTS. The region before γ_{max} was the target for the fit in order to estimate the value consistently with the nominal energy of the particle.

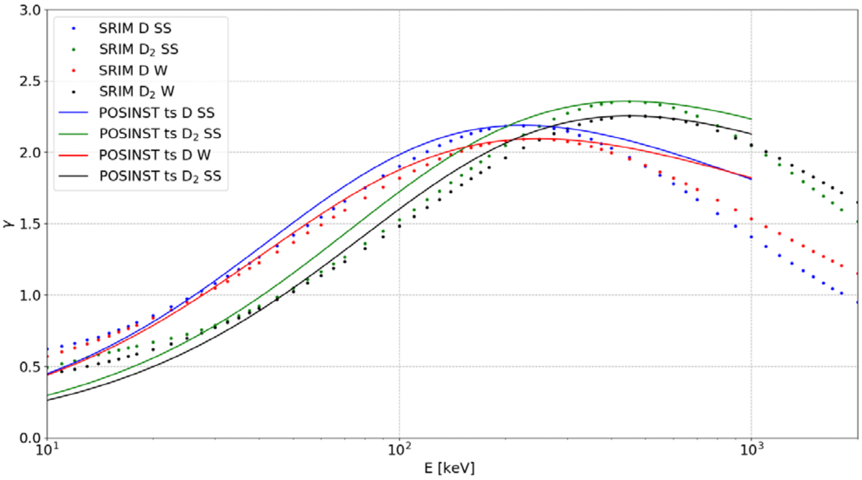

Fig. 6.4 SEY as a function of energy for D and D_2 onto W and SS material. The functions fit are shown for each SEY.

In particular, the values that matter are those closer to 100 keV. The maximum deviation is about 31% in case of D_2 onto SS.

6.6 Results

Two Warp models were compared: one with the secondary electrons ejected from the metal boundaries due to the ion collisions and from the residual gas ionization, the other with only the electron coming from the residual gas ionization. In this way it was possible to determine the limitations of one model respect to the other. The trace-forward method was applied to the model with the secondaries from collisions. The resulted input was then tested also with the model with only the electrons from the gas ionization. The first model requires a much larger performance machine with respect to the second, due to the larger number of secondary electrons emitted from the metals; only one machine was at disposal to do so, thus the trace-forward method was not fully accomplished due to the lack of time. Only two points could be simulated (2 and 3) for this full model. The results are presented in two groups: the transient phenomena and the comparison with the experimental results.

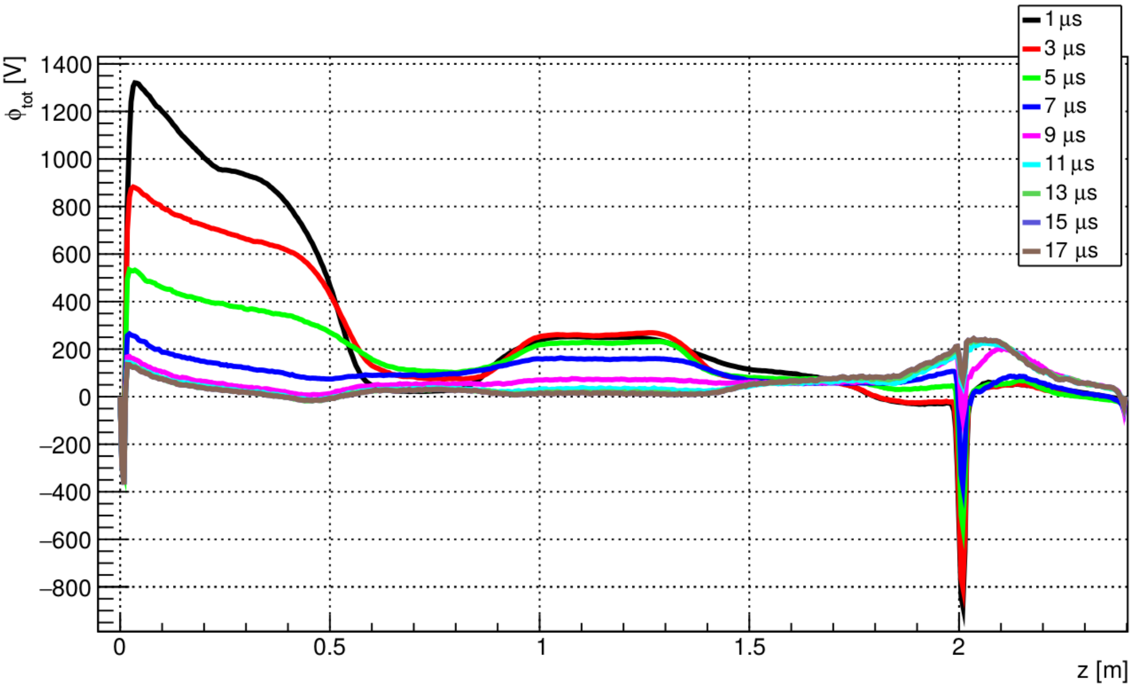

Fig. 6.5 Φ_{tot} along axis at different times for the complete model

6.6.1 Transient phenomena

The transient potential along axis $\Phi_{tot} = \Phi_{applied} + \Phi_{self}$ with respect to the time for point 3 (see 6.1) is shown in Fig. 6.5. The model used is the complete one.

The trend depends on several conditions: losses, s.c.c. and boundaries. At the very beginning ($t = 1$ μs) the self-field potential of the beam at the exit of the extraction source is 1.3 kV. The beam divergence and dimension are so large to cause losses all along the LEBT (see Fig. 6.6). The secondary electrons from collisions immediately start to be ejected from the various parts of the LEBT.

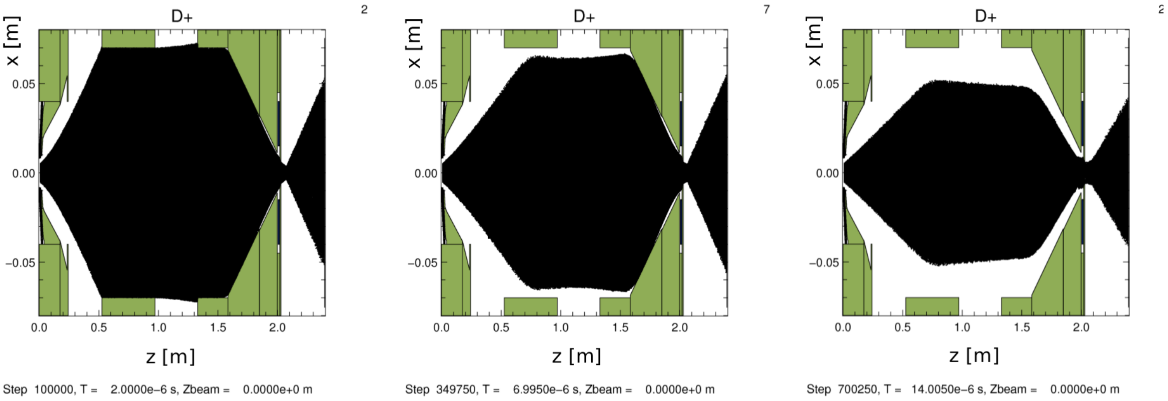

Fig. 6.6 D^+ beam occupancy with respect to different moment in time

At the same time the neutralizing gas is ionized by the D^+, D_2^+ and e^-, contributing to the space-charge compensation. The beam reduces its dimensions, changing the ratio r_p/a and therefore the potential. The waist in the RFQ injection cone starts to build, increasing the potential along the cone. After almost 14 μs the potential is substantially decreased in all the part of the LEBT but at the cone injection.

The steady state of this kind of simulations is not straight-forward to be determined due to phenomena such as electron heating and instabilities of simulation described in [47, 48]. In order to not to be dominated by such phenomena it is important to control all the parameters of the simulation. Fig. 6.7 shows the rms trend of the beam at 300 mm after the PE extraction hole. The transmission through the cone is presented in the lower right plot. It is possible to see that an asymptotic trend is reached after 14 μs. The divergence and dimension decrease such as the transmission through the cone. At the steady state regime small losses occur at the RFQ injection hole due to the formation of beam halo 2.11.

Fig. 6.8 shows the trend of $\varepsilon_{rms,x}$,α_x, β_x at the EMU position and at the RFQ injection in the time window where the transmission through the cone is $> 97\%$. The emittance trend is not monotonic until partial relaxation of the distribution, thanks to the redistribution

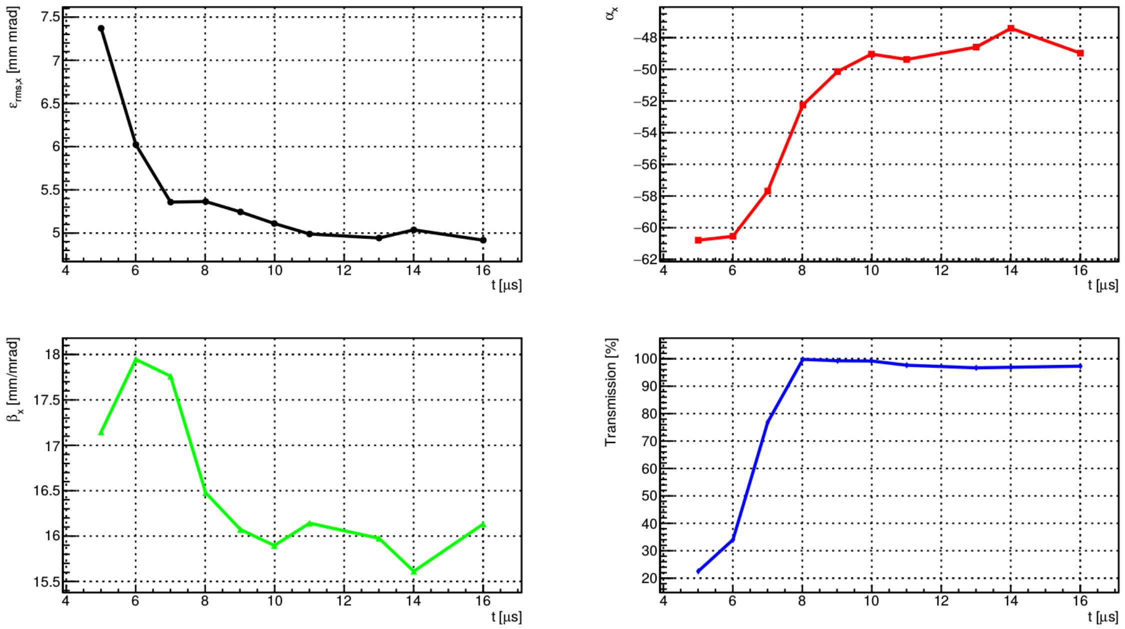

Fig. 6.7 Trend of the rms quantities at 300 mm from PE extraction hole. The plot shows respectively the $\varepsilon_{rms,x}$, α_x, β_x. The transmission through the cone is presented in the lower right plot.

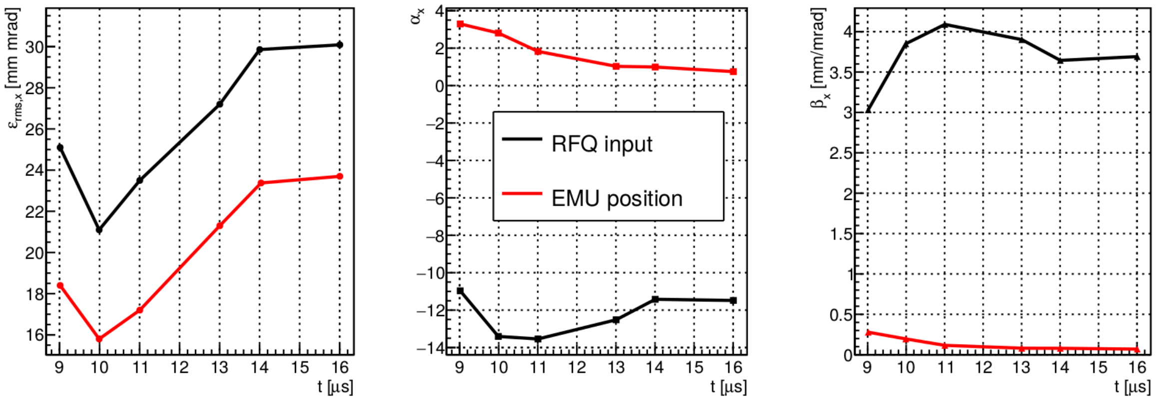

Fig. 6.8 Trend of the rms parameters at the RFQ injection and at the EMU position.

of the phase spaces due the non-linear focus/defocusing of the overall charge density (i.e. $\rho_{\text{tot}} = \rho(\rho_{e^-}, \rho_{d_2^+}, \rho_{d^+})$). After an initial emittance decrease, the halo starts to build up and the emittance increases, stabilizing around $\varepsilon_{rms,n,x} = 0.32$ mm mrad.

The phase space evolution with respect to the time can give an idea of the mismatch of the first μs at the entrance of the RFQ. The closer matching in Twiss can be found in point 2, thus the following results will focus on this point (Fig. 6.9).

It is possible to see the large relaxation of the phase space distribution. At the steady state there is a built up of the satellite structures [49], caused by the nonlinear focusing of the electrons in the solenoid field. There is a large change in the emittance, while the mismatch changes of 5%

Table 6.2 Change of parameters with respect to the time after maximum transmission in reached

t [μs]	$\varepsilon_{n,rms,x}$ [mm mrad]	β_x [mm/mrad]	α_x	mismatch [%]
9	0.58	1.83	0.14	37%
16	0.23	1.53	0.07	42%

In 7 μs the Twiss at at the exit of the extraction stabilize. Taking into account that the gas pressure was increased in order to reach the steady state faster, the difference between the theoretical time for steady state calculated with Eq. 2.26 results 4 μs which is a factor 4 less than the simulation.

This difference can be explained due to the fact that in reality the system redistributes constantly its charges due to the presence of the applied magnetic and external fields (which are not taken into account in the theory). Moreover the charge density is not uniform and changes with the time.

Assuming a direct proportionality, the estimated time needed for s.c.c., scaling the value with the half the pressure, is 59 μs. Similarly the time needed for stabilizing the Twiss parameters after reaching the maximum transmission through the cone, in case of the nominal gas pressure, is 28.1 μs.

The Fig. 6.10 shows the projection of the x coordinate at the RFQ injection. It is possible to see the space charge wave that propagates in time, changing the hollow distribution to a peak distribution. The final structure shows regular concentric charge distributions similar to what was found in Chapter 4 (see Fig. 5.28).

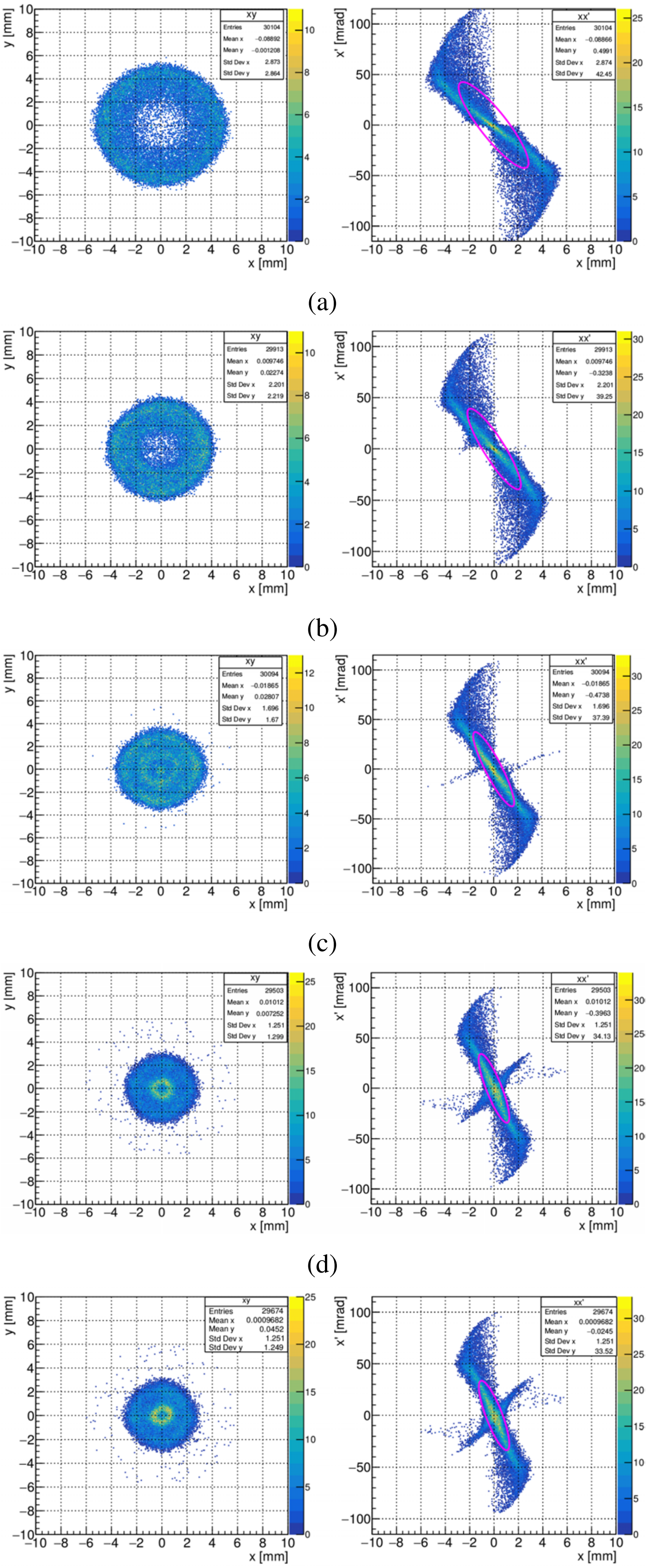

(a)

(b)

(c)

(d)

(e)

Fig. 6.9 Phase spaces evolution in time at the RFQ injection for point 2

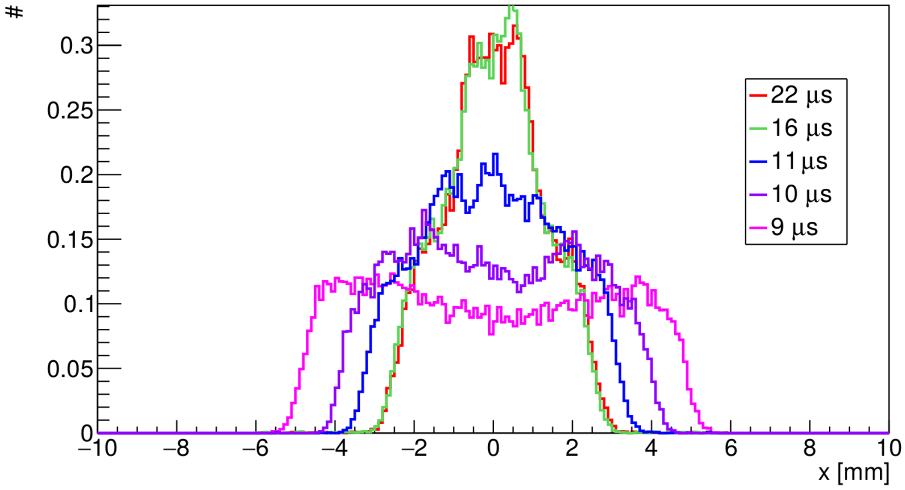

Fig. 6.10 x-projection of the beam at RFQ injection at different times.

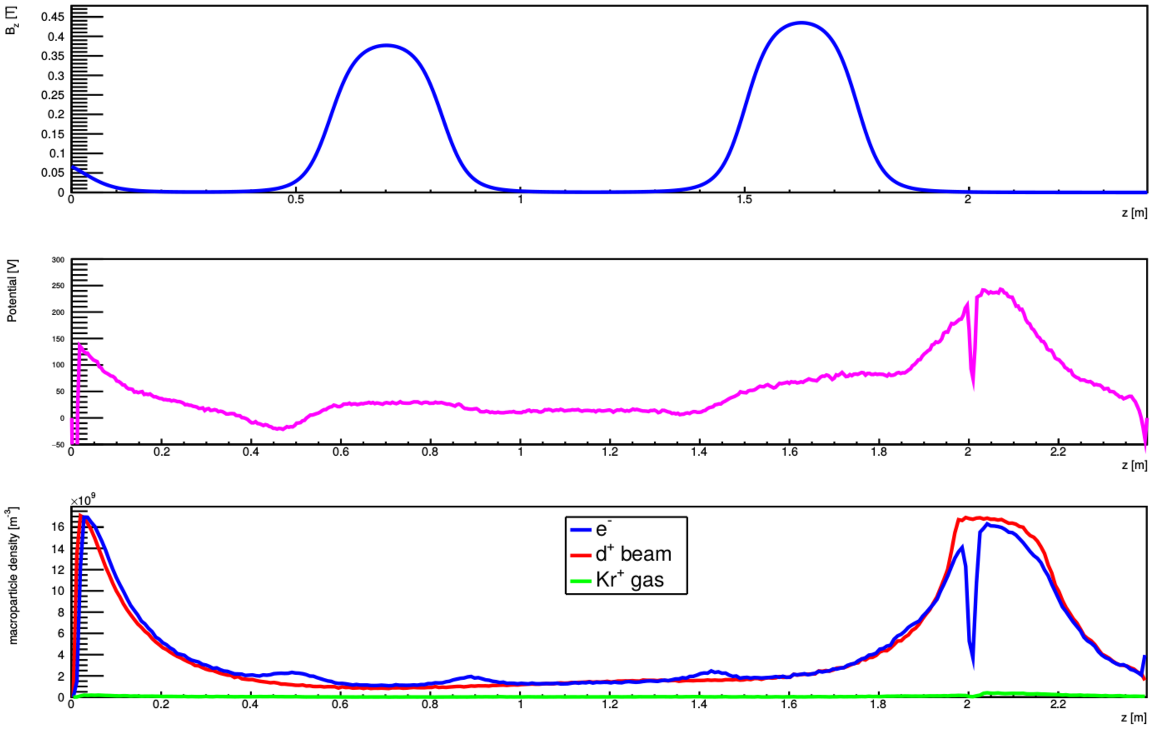

Fig. 6.11 B_z, Φ_{tot} and $\rho_e, \rho_d, \rho_{Kr}$ along z.

In this case the simulation is full 3d and there are no rz approximations. Some more complex phenomena such as the satellites (see Fig. 6.9) can be seen as far as the simulation reaches the steady state. In order to investigate further the self-field potential and the macroparticles-densities at the steady state, it is worth to study the trend along z and r. As an example, point 2 is considered.

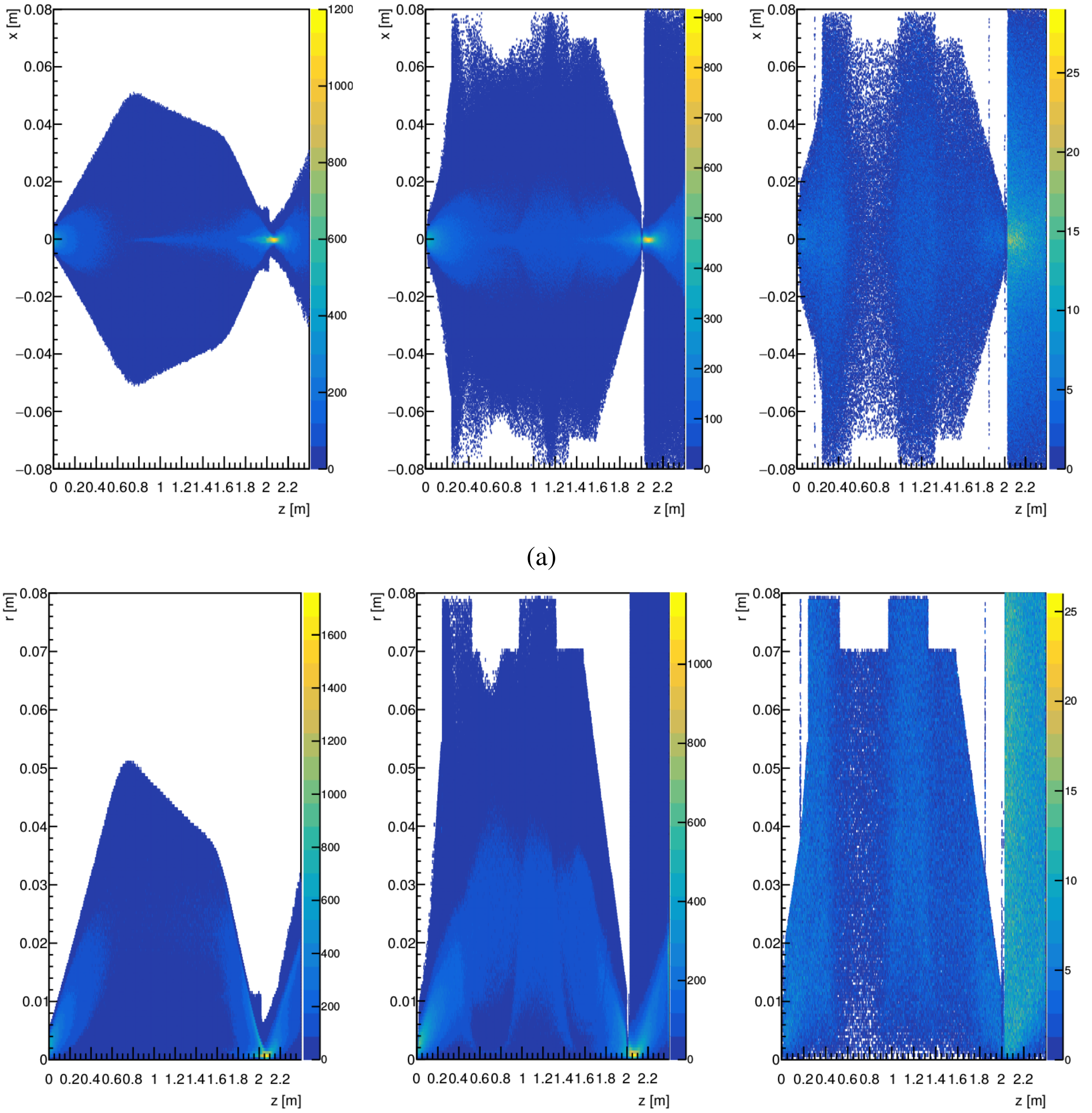

(a)

(b)

Fig. 6.12 Density plots of rz (b) and xz (a) plane. The first column shows the deuteron density, the second column shows the electrons and the third one shows the Kr.

Fig. 6.11 shows the B_z, Φ_{tot} and ρ_e, ρ_d, ρ_{Kr} along z. The first plot displays the B_z. There are electron density concentrations at the entrance and at the exit of the solenoids: these are due to the coherent v_z velocity given by the repeller fields, which can accelerate some part of the electrons up to 1 keV: the electrons are then focused and bound by the large (respect to electron energy) applied solenoid field (see Chapter 3).

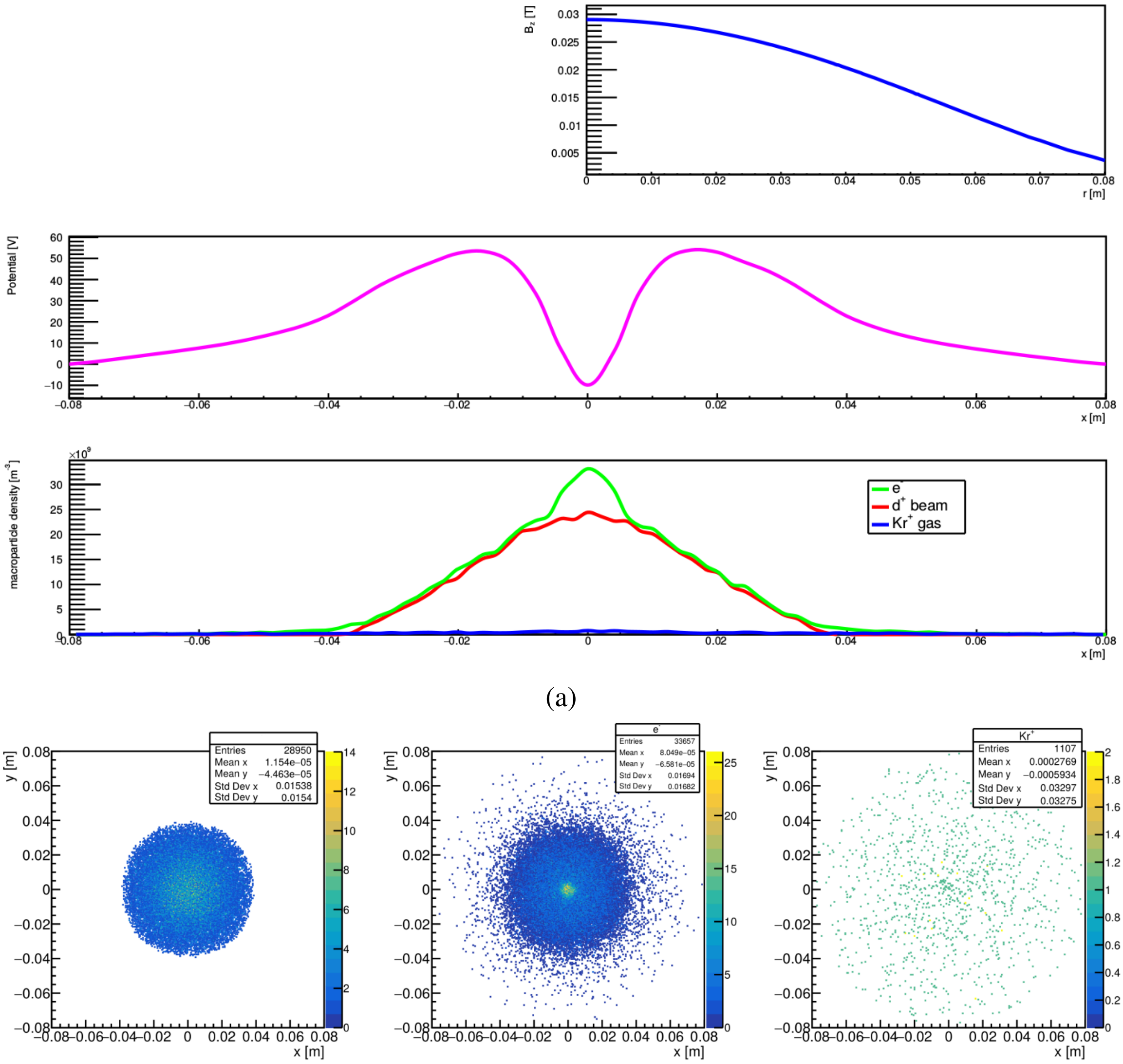

(a)

(b)

Fig. 6.13 Density plots of xy plane, charge densities and ϕ_{tot} along x at $z = 0.5$ m (just before the solenoid 1)

Moreover, the solenoid and source axial field configuration set a magnetic mirror like structure, with a given level of confinement along z. This fact facilitate the accumulation of the electrons between the magnetic peaks. The ϕ_{tot} trend along z depends also on the bore

aperture and the radius of the beam; as far as the beam approaches to the rfq injection point, the potential grows despite the cone bore aperture decreases. At the cone repeller position, ρ_e suddenly falls due to the repulsion of the repeller.
The electron density follows mainly the deuteron density but at the repeller positions and at the entrance and at the exit of the solenoids, some part of the electron population are strongly focused along axis. The Kr ions density, instead remains negligible all along the line.

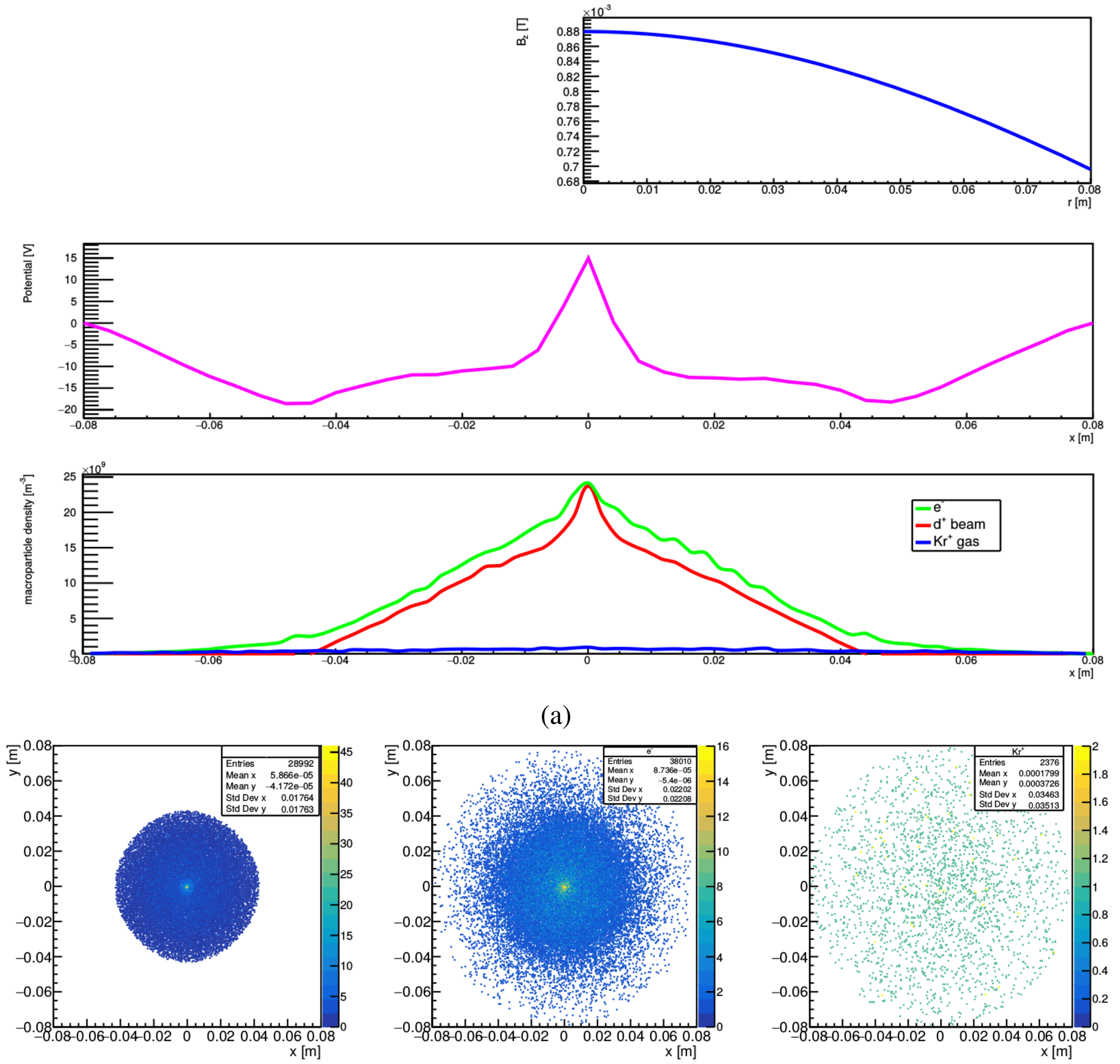

(a)

(b)

Fig. 6.14 Density plots of xy plane, charge densities and ϕ_{tot} along x at $z = 1.2$ m (between the first and the second solenoid)

The density plots presented in Fig. 6.12 shows again that at the entrance and exit of the solenoids there is a strong focusing of the electron population: this behavior suggests that the

phenomena starts with electrons with a longitudinal direction of the motion that are strongly focused by the solenoid fields; at this point, the large charge density along axis builds up nonlinear focusing fields which focuses some o the deuterons population. Therefore, part of the deuteron and electron density follows mutually these peak densities.
As far as the electrons approaches to the second repeller (which can be the source repeller or the cone repeller), the longitudinal velocity components $v_{||}$ is transformed into transverse component $v_{\perp}$: the electrons are spread out and the peak disappears.

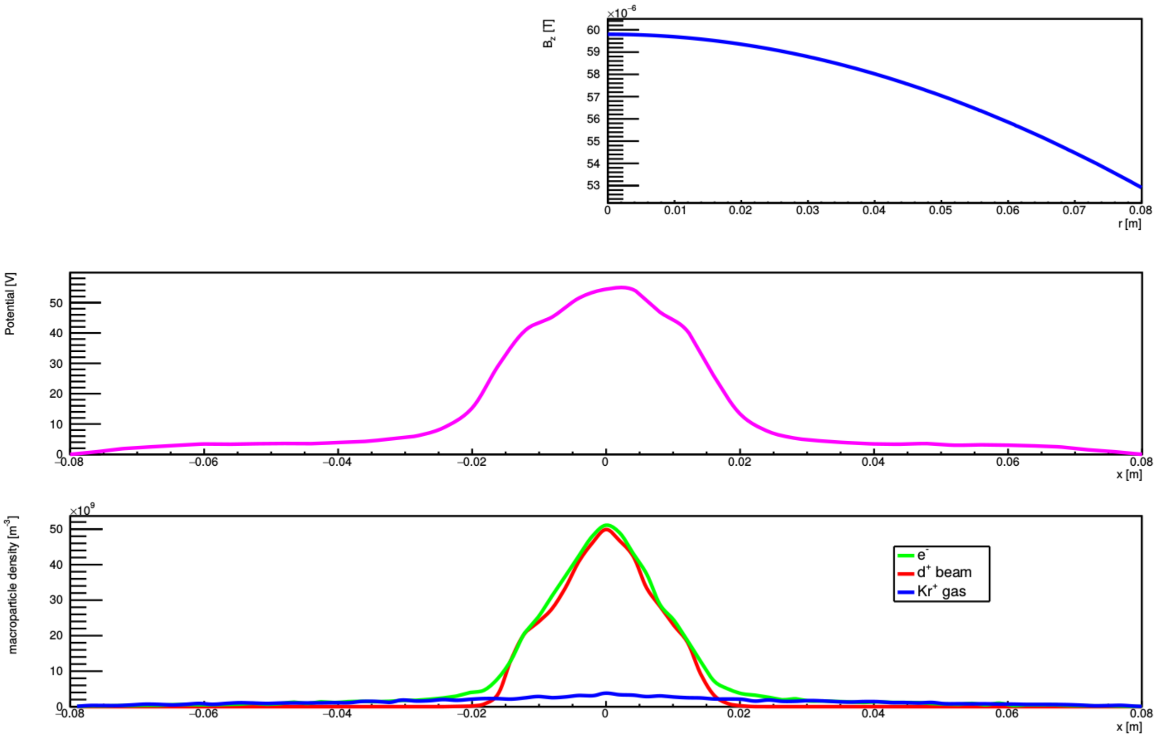

(a)

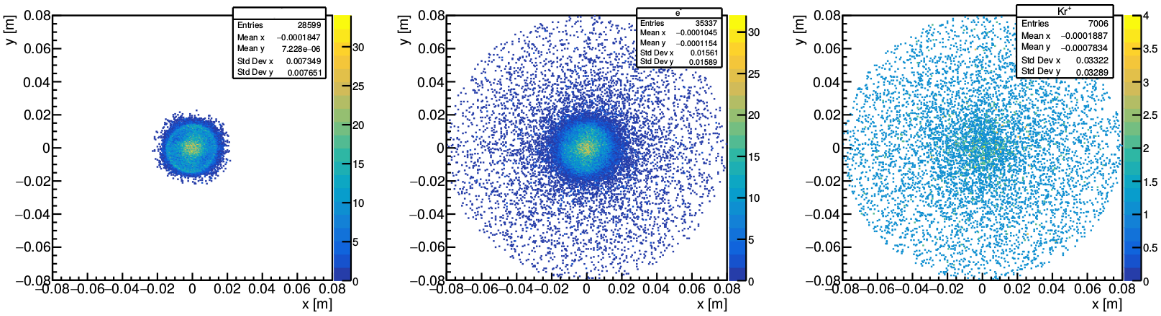

(b)

Fig. 6.15 Density plots of xy plane, charge densities and ϕ_{tot} along x at $z = 2.3$ m (between the cone and the EMU)

It is interesting to study this phenomena, looking at the transverse plane of the simulation. At $z = 0.5$ m, coordinate of first electron charge distribution bump in Fig. 6.11, the ϕ_{tot} vs z is modified by the built up of the central electron density due to the focusing field of the solenoid. The density plots show the distribution of particles in xy: the proton distribution does not yet show any central peak, while the electron distributions clearly has an increase of macroparticle density along axis (see Fig. 6.13).

At 1.2 m both the distributions present axial peaks, as an effect of the mutual attraction, as shown in Fig. 6.14. The axial electron density acted as a non linear lens to the deuterons along axis, changing the central part of their distribution. At the end of the LEBT, approaching to the repeller, the peaked distribution is depleted by the repeller field. The peak disappears both for the electrons and for the deuterons. However, any rms emittance growth due to the electron axial lens will not be canceled.

At the second diagnostic box (after the repeller) there is no more the peak in the distribution (Fig. 6.15) and the magnetic field is negligible.

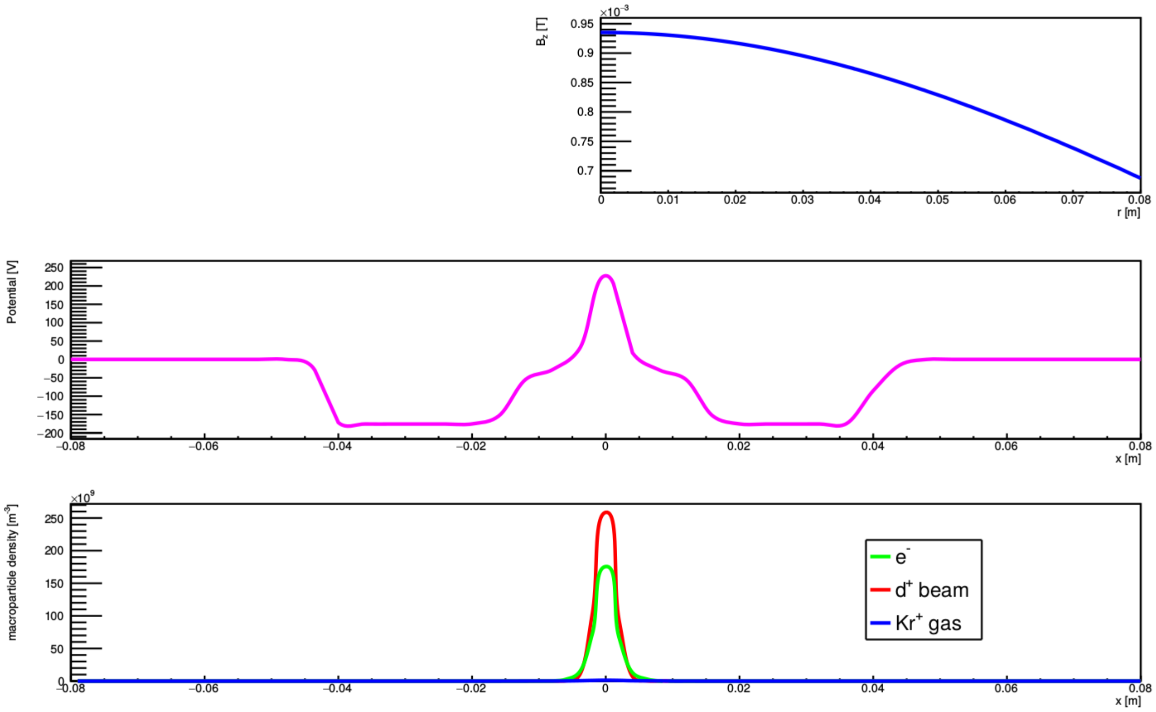

Fig. 6.16 Charge densities and ϕ_{tot} along x at $z = 2.02$ m (repeller position)

6.6.2 Secondaries vs no secondaries

The effects of secondaries generated by the collisions can be seen in the time needed to reach the steady state. The electron macro-particles number reaches the asymptote at 9 μs in case of the implementation of electron ejection from metals due to ion collisions, while in the other case at 12 μs

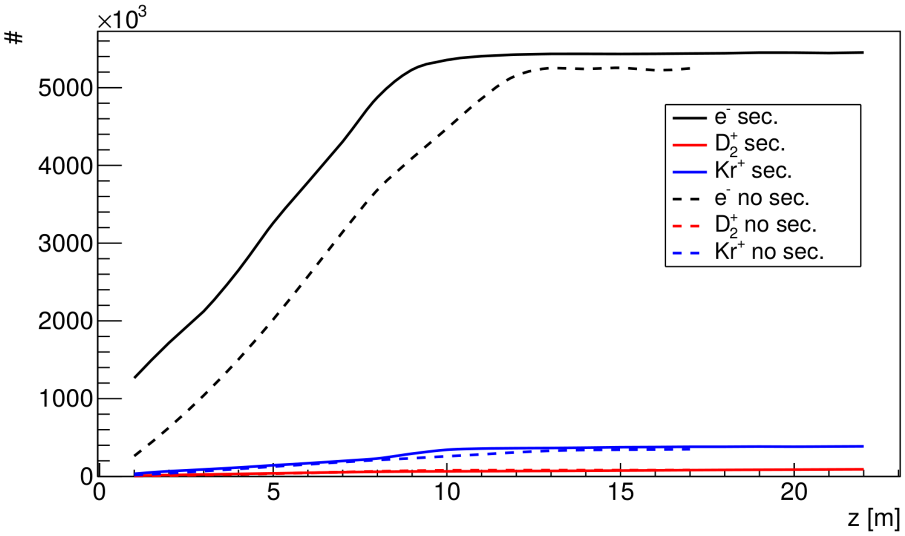

Fig. 6.17 Kr^+, D^+ and e^- species number with respect to the time of the model with secondaries and without

At the steady state, there are few sources of collisions:

- the D_2^+ contaminats produced by the source are not focused by the magnetic system such as the D^+, due the different rigidity. Therefore, the ions collide onto the Cu of the cone, generating electrons.
- when the emittancemeter is inserted for the emittance measurement, it is constantly hit by the deuterium beam. Due to the fact that the yield of backstreaming electrons is not zero, there is a constant electron supply in diagnostic box 2.
- the electron which interact with the metal boundaries can be absorbed or re-emitted with different energy depending on the primary electron momentum.

The secondary electrons modify the space charge compensation along the line. The residual self-field potential can be seen in Fig. 6.18. The Φ_{tot} of the complete model start to separate from the other when the simulation approaches the cone.
After the RFQ injection point, the difference between the two potentials persist up to the end of simulation due to the electrons generated from the emittancemeter.

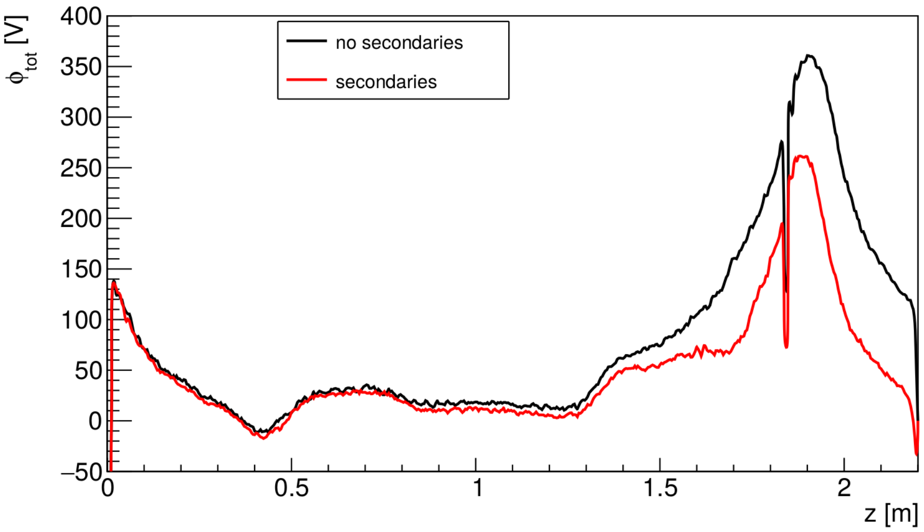

Fig. 6.18 Residual field potential along the line given by the model with and without secondary electrons. Red line is the Φ_{tot} with the electron from collisions, while the black curve show the Φ_{tot} with only the electrons coming from the residual gas

Before the cone, the secondary electrons are generated by the d_2^+ contaminant beam which hits the copper cone, while, after the cone in a region where only the self-field of the beam is present, the emittancemeter changes the neutralization, as was suggested in the previous chapter with the post analysis of the proton point.

The space charge compensation degree in the second diagnostic box can be estimated by (Eq. 2.24): 98% for the complete model, while it is 92% for the other; taking into account the region from the cone up to the emittancemeter (367 mm) the 6% difference changes substantially the beam dynamics of the beam as seen in the preliminary model of Chapter 5. Therefore its effect cannot be neglected.

6.6.3 Comparison with simulation

As it was said at the beginning of the chapter, the trace-forward process was not fully complete, but still some interesting results were obtained. Fig. 6.20 and Fig. 6.19 shows the comparison between the experimental and simulated phase space.

The point 2 simulation shows larger difference with respect to the point 3 which is in fair agreement. The phase spaces are shown in Fig. 6.20. One of the problems which led to the develop this new model was the difference found in the beams x-profile between the simulated and measured deuteron beam (see Fig. 5.34). The new model allows to follow the beam profile modifications due to the solenoid strength change with enough precision (less

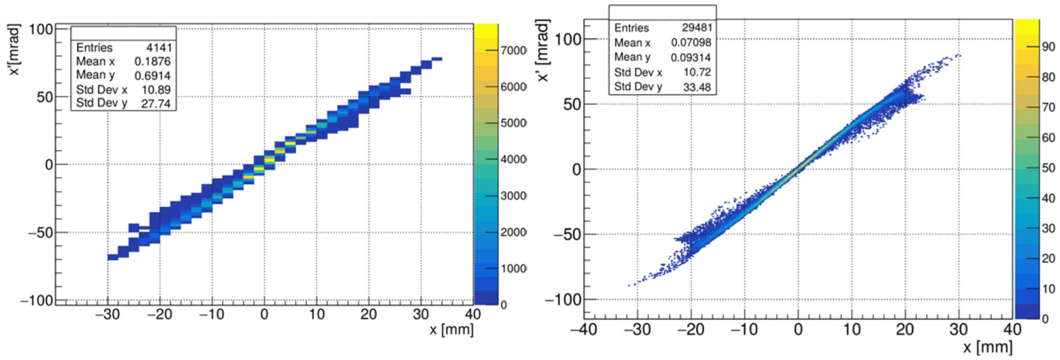

(a)

(b)

Fig. 6.19 Measured (a) and simulated (b) phase space at point 3

than 5 % difference in the rms quantities between the simulation and the experiment). The central peak, however is not in agreement.

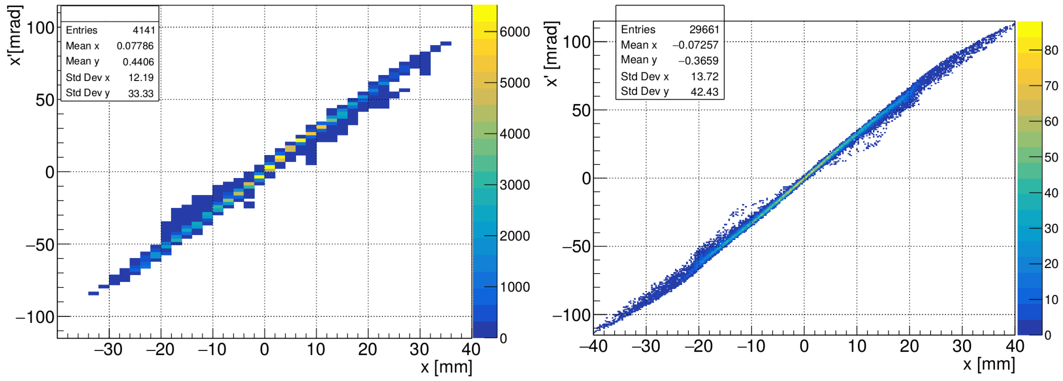

(a)

(b)

Fig. 6.20 Measured (a) and simulated (b) phase space at point 2

In conclusion, Fig. 6.22 presents the trend of the rms quantities of the deuteron beam measured at the emittancemeter: $\varepsilon_{rms,x}$,α_x, β_x.

The comparison involves the measured and simulated values with complete model (secondaries from collisions) and simplified model (with electrons belonging only to ionization of the residual gas).

The $\varepsilon_{rms,x}$ of the complete model suggests a more flat trend with respect to the simplified model; another improvement is that the β_x are closer to the experimental values with respect to the case in which backstreaming electron effect are included. The error bars in the simulation are the values oscillation at the steady state regime.

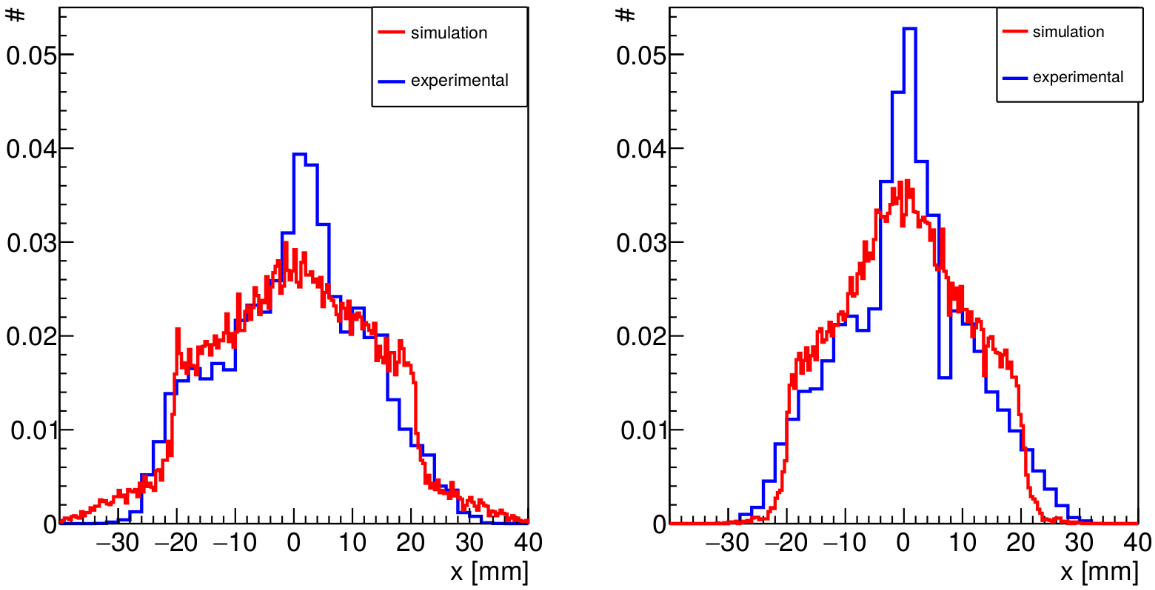

Fig. 6.21 Measured and simulated x-profile of the deuteron beam at point 2 (right plot) and 3 (left plot)

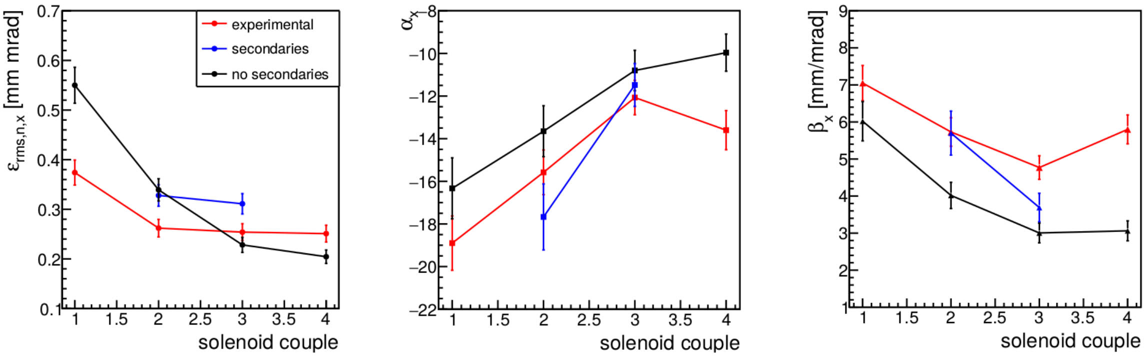

Fig. 6.22 Comparison of the measured and simulated rms quantities with respect to different solenoid couples

6.6.4 Acceleration through the RFQ

The point 2 input was transported through the RFQ in order to study the transient phenomena. The main approximation is the different residual potential (thus s.c.c.) at the RFQ injection: as it was explained before, the simulations were performed with phase A2 layout (i.e. with a diagnostic box after the LEBT cone); therefore, the electrons presence in the region of RFQ injection may not be representative of the real RFQ boundary conditions. However, this problem affects just few mm length of simulation.

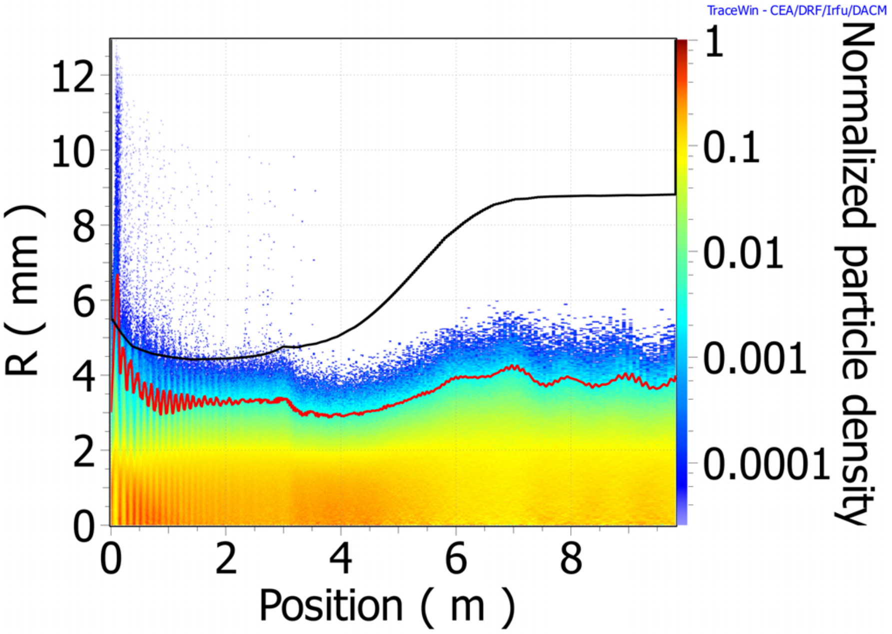

Fig. 6.23 Deuteron point 2 transport and acceleration through the RFQ, *rz* view

Another important aspect to be taken into account is that, despite point 2 has a minor mismatch, its value is quite large respect to the requirements (i.e. 42%). Thus, a lower transmission respect to the nominal one $< 90\%$ is expected. However it is worth to try to study the transient of the RFQ inner and output parameters, in order to estimate the effect of the head of the beam incoming into the RFQ. Fig. 6.23 shows the transport and acceleration of such beam into the RFQ: it is possible to notice the mismatch effect which couples with the non-linear focusing strength in the first part of the linac; major losses occur in this spatial interval. The perturbation of the system can be seen from the emittance trends along the accelerator Fig. 6.24

Up to three meters, there is the generation of longitudinal emittance and, at the same time, fast and coherent oscillations of the transverse emittances (blue and red curves) caused by the mismatch.

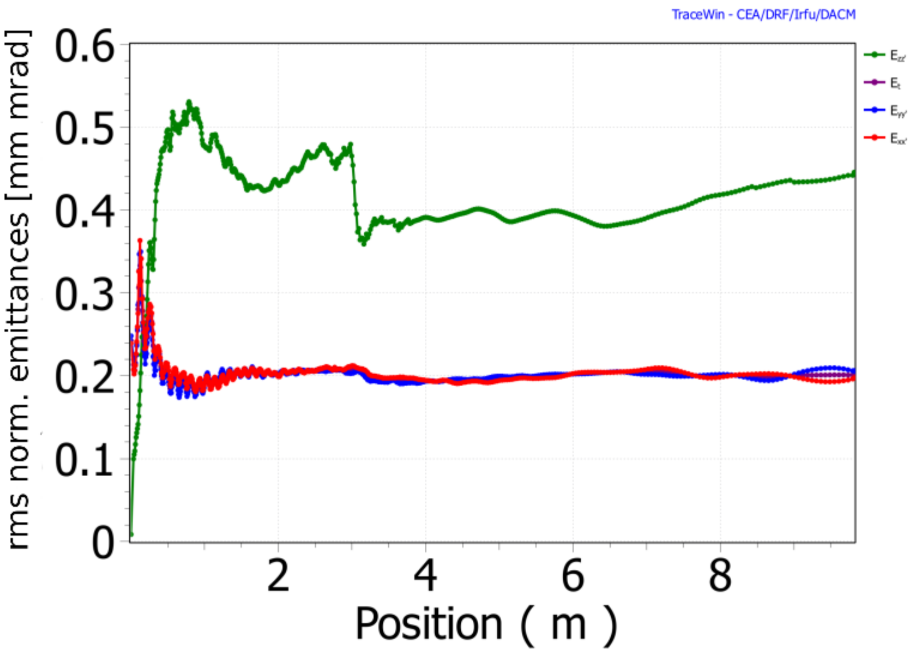

Fig. 6.24 Deuteron point 2 transport and acceleration through the RFQ, longitudinal and transverse emittances

After the gentle buncher, the beam gets to an equilibrium state, with few oscillations. The drop in the green curve is due to the limits imposed by TOUTATIS on the longitudinal emittance at the accelerating section. All the above considerations can be summarized looking at the power deposition along the RFQ in Fig. 6.25.

Table 6.3 Losses and watts deposited on the RFQ with respect ot various input distribution with the same Twiss parameters

Dist. type	Halo parameter	losses [%]	kW
q.s. Waterbag	0.4	15.7	2.9
Gaussian	0.8	16.6	3.0
from WARP	3.3	18.0	2.9

The main losses are concentrated before the 3 m, which corresponds to the end of the gentle buncher section. The integrated power deposited in case of CW beam is 2.9 kW.

Normally the RFQ-designer uses "standard" distributions in order to predict the RFQ under study, such as the quasistatic waterbag and gaussian. It is worth to compare the predicted losses of these type of distributions with the same Twiss parameters of point 2, and the relative estimated real distribution. Table 6.3 shows the transmission, the total kW lost into the RFQ and the Halo parameter relative to each distribution: truncated gaussian at 3σ, quasistatic waterbag and simulated one.

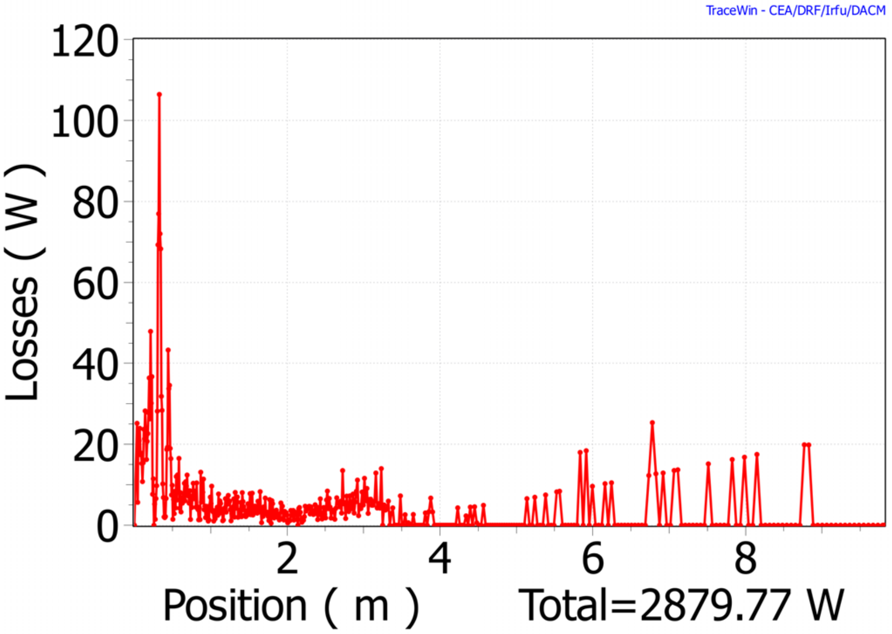

Fig. 6.25 Power deposition along the RFQ due to the transport and acceleration of point 2. The power loss are collected at the end of each RFQ cell

It is possible to see that the approximation holds quite good for the W lost into the RFQ and the losses. However, the estimates with the standard distributions result optimistic as far as the losses are concerned of 2.3%. Therefore, for a fine estimate of the transmission it is necessary to study the RFQ acceleration and transport with the realistic distribution. The last but not the least aspect refers to the transient transmission and parameters change due to the build up of space charge compensation. The trend of Twiss, emittance and transmission through the cone respect to the time at the RFQ injection point was already studied. Now the question is: how does the RFQ behave to the changing input beam in time? How does the output Twiss (which will affect the MEBT losses) ?

In order to do so, the input distributions displayed in Fig. 6.9 were injected into the RFQ and their parameters studied. It would have been meaningless trying to inject the distribution before 9 μs due to the lower transmission through the cone itself which would bias the study. The results are presented in Fig. 6.26

With the level of background gas of the simulation, the steady state is reached in $7us$. It is possible to notice a fast change of the parameters in 2 μs. After that the parameters reaches a stable points in the remaining 5 μs. Scaling the time with the real gas pressure (factor

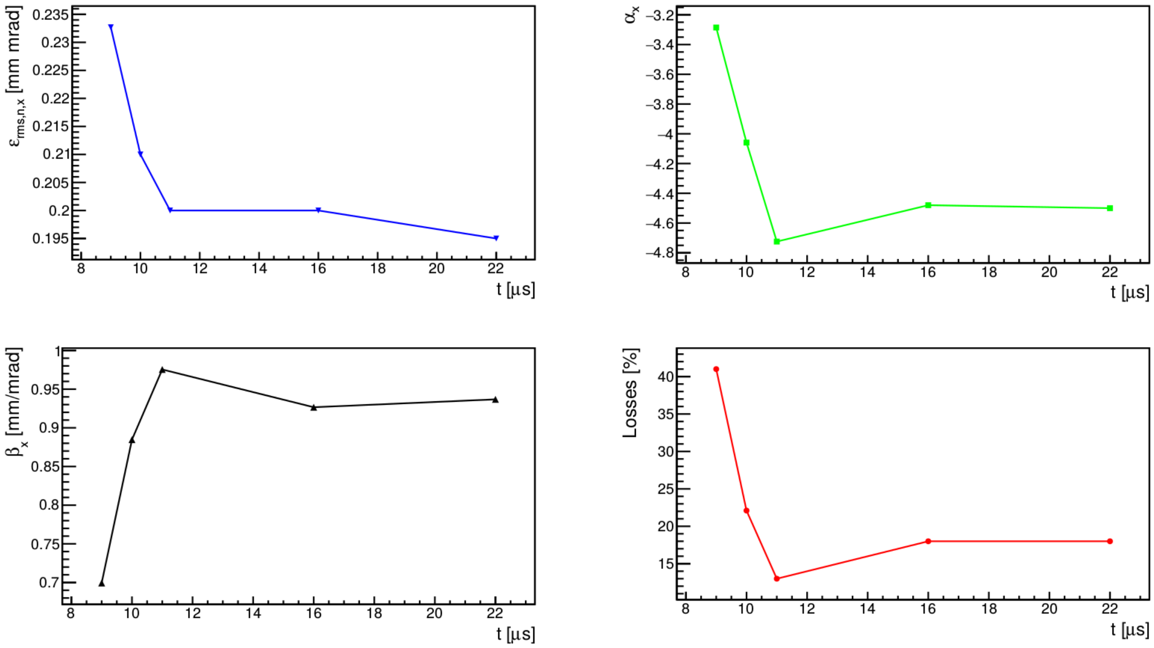

Fig. 6.26 Transmission, trends of transmission, and output RFQ Twiss parameters and emittances respect to time

two less that what was set in simulation), the transient time results 28 μs. Gathering all the simulation time needed for steady state, the first 58 μs of the incoming beam into the RFQ will be useless for characterizing the machine, since up to 30 μs the beam is lost mainly on the injection cone. After 30 μs, the beam has a larger transmission through the cone: however it takes other 28 μs before the steady state is reached and the Twiss are stabilized.

6.7 Extraction column simulation and phase A3 result comparison

Despite the general agreement with the experimental data, the simulations do not reproduce the measured central peak of the x-projection. This may be due to the approximated input condition (parabolic in this thesis work) at the LEBT of the distribution. In order to study the input distribution generated by the extraction source, an extensive measurement/simulation campaign was performed in order to characterized the extraction. The following sections present the studies done about this topic.

6.7.1 Extraction column preliminary simulations

As shown in Chapter 3, the extracted beam behavior is influenced by the multi-species extension of the Child-Langmuir formula 3.11. One of the major problem encounter during the commissioning was the lower proton fraction with respect to the deuteron beam which decreases the beam quality at the output. This can limit the extractable current that can be produce with protons in scaling regime with the deuteron case.
Measurements show that this issue decreases with smaller diameters hole with respect to nominal $r = 6$ mm. Therefore, it is necessary to adjust the extraction system in order to improve the performance in case of proton beam extraction. Moreover, it is important to limit as much as possible the modifications of the extraction system in order to reduce the time for switching between the proton and deuteron electrode configurations, allowing also to scale directly the voltages of the extraction electrodes from proton to deuteron case.
In order to meet all the requirements a study for a new plasma electrodes was performed. The objective was to reproduce the deuteron working point performances in terms of emittance and Twiss via the scaling law. The deuteron point taken into account consists in $I_{\text{ext}} = 150$ mA of deuteron beam, with a current density of $J_{\text{D}} = 132.6$ mA/cm^2 (6 mm beam radius and 20 kV potential difference between the PE and the intermediate). Considering 60% H^+, 35% H_2^+ and 5% H_3^+, reduced diameter of PE hole of 10 mm, the maximum extracted current (from Eq. 3.11) results 50 mA of total extracted current. The more the proton beam ratio grows, the more H^+ current the extraction can sustain without losing the beam quality.
During the study it was observed that the five electrode system foresees a structure with two minima, linked with the two difference electric field magnitude between the two gaps.
The magnitude is indeed controlled by the intermediate electrode voltage, as shown in Fig.6.27 for a 100 mA total extracted beam. As it is possible to see, there are two relative minimum regions for each electric field configuration in the two gaps; in particular, it is

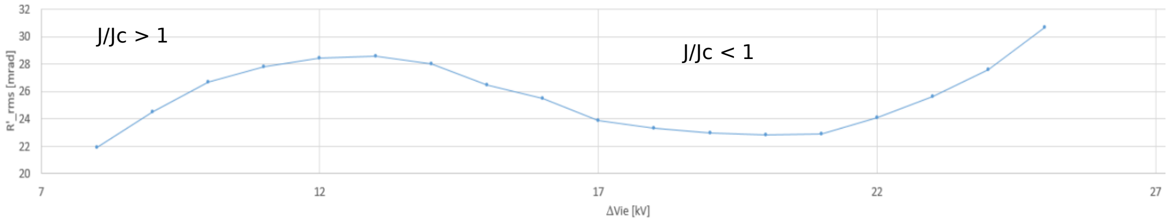

Fig. 6.27 Trend of R' at 19.6 mm from the PE hole for a 100 mA total deuteron beam. The two region for the plasma meniscus (convex $J/J_c > 1$ and concave $J/J_c < 1$) are shown

interesting to study the low intermediate electrode voltage interval, where, despite the convex shape of the plasma meniscus, the second gap lens effect is so strong that it focuses the beam nevertheless.

The deuterium working point that was analyzed in the previous section refers to a similar zone: the intermediate electron voltage was set to 20 kV potential difference. In order to see if the analytic formula (Eq. 3.11) works and to validate the study done for the new proton electron design, the deuterium point R, R' and emittance was compared via AXCEL simulations with the guessed scaled proton beam. The results are presented in Table 6.4.

Table 6.4 R', R and $\varepsilon_{rms,r}$ for the proton and deuteron extraction columns.

Type	R' [mrad]	R [mm]	$\varepsilon_{rms,r}$
PE proton	27.8	7.2	9.0
PE deuteron	29.2	7.7	8.7

The scaling works well within 10% and therefore it can be used during commissioning in order to set the machine when switching from proton to deuteron beam. The final extraction hole diameter was chosen to be 4.5 mm in order to still improve the proton fraction. Since simulations show that smaller diameter hole than 4.5 mm decreases the extraction optics quality, due to the too large difference between the PE aperture and the rest of electrodes, it was decided not to reduce it furthermore.

6.7.2 Interpretation of the experimental measurements of phase A3 with simulations

In order to test the simulation models of the extraction system, the LEBT was removed and the diagnostic box was placed in front of the the extraction column. For that campaign it was also possible to measure the beam profile in the middle of the diagnostic box.

The distance between the plasma electrode and the emittancemeter was 776.5 mm. The beam analyzed has the same characteristics of the deuteron point studied for the trace-forward in the previous section (phase A2).

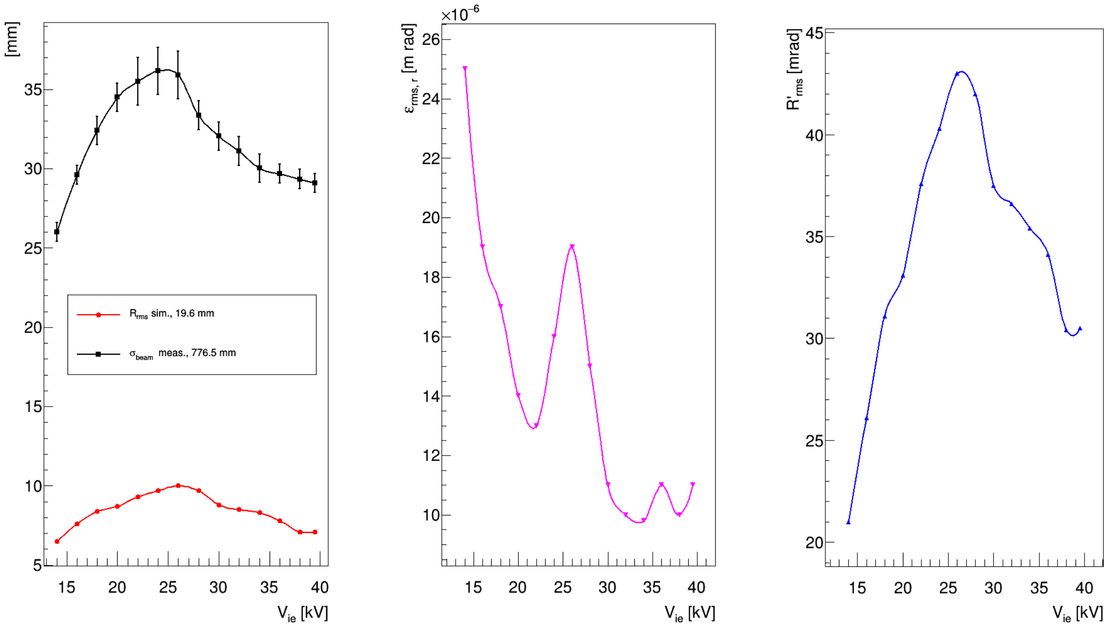

Fig. 6.28 The first plot shows the measured σ_{beam} and simulated R_{rms} at 776.5 mm and 19.6 mm from PE respectively. The other two plots present the simulated $\varepsilon_{rms,r}$ and the divergence at 19.6 mm

In particular, the experimental trend of the σ_{beam} at (776.5 mm) the beam profile fitted with a Gaussian was compared, with respect to different intermediate electrode voltages and the r_{rms} at 19.6 mm given by AXCEL simulations. If the model simulates correctly the process, then the minimum and the maximum coordinates should correspond.

If this condition is satisfied, it is possible to estimate the trend of other parameters, as shown in 6.28. The minimum and the maximum coordinates are well in agreement despite all the approximations made by the code. Moreover, the two minimum structure was confirmed. It predicts the maximum emittance and divergence at $25-26$ kV. This is validated by the measurement shown in the first plot at 776.5 mm, which shows the larger beam dimension at the same intermediate electrode value.

The double minimum structure can be clearly seen looking at the simulated beam transport and trajectories in Fig. 6.29 (which refers to the set of measurement presented in Fig. 6.28): the plot (a), (c) and (e) display the rz trajectory of the multiple-species beam, while (b), (d) and (f) are the transverse phase space at the end of the simulation.

For the regime $J/J_c > 1$ the beam drifts in the first gap with an energy of 20 keV. As far as it approaches to the second gap, it receives a strong focusing kick which squeezes the beam envelope. The effect of the spherical aberration gained at the edge of the intermediate electrode and space charge emittance growth can be seen in plot (b) and in the value of the rms emittance. But still this configuration behaves in simulation and in the experiment as the lowest in divergence.

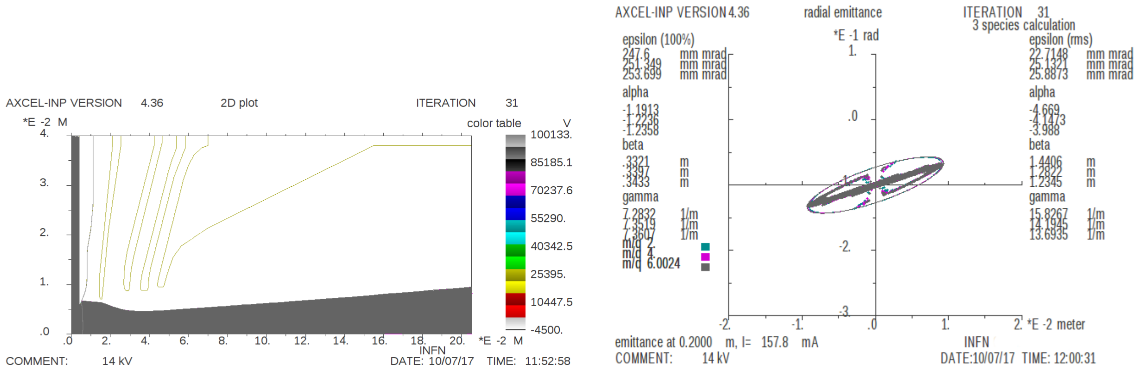

(a) $\Delta V_{ie} = 14$ kV (b)

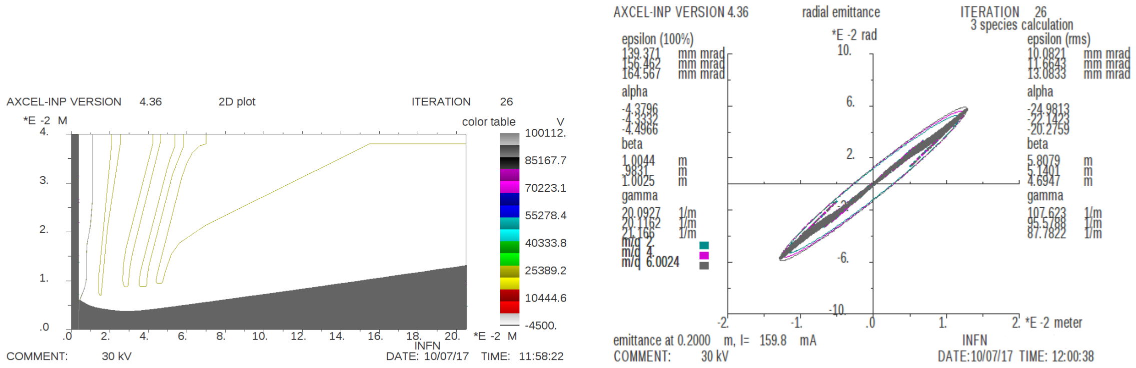

(c) $\Delta V_{ie} = 30$ kV (d)

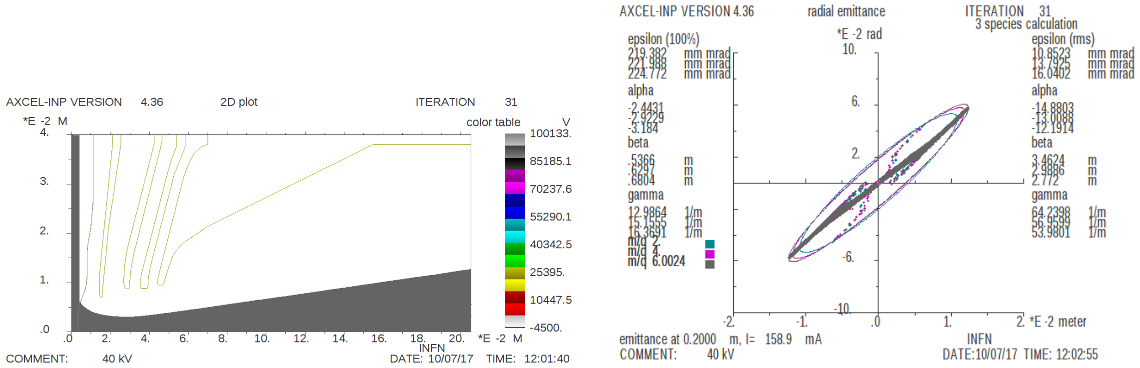

(e) $\Delta V_{ie} = 40$ kV (f)

Fig. 6.29 Simulated extraction system behavior with respect to measurements of A3 phase. The beam behavior is shown for different first gap voltage.

The qualitative insight given by these simulations is a very good result and helps to guide the commissioning. The non-linearities obtained from the source extraction when the optics is similarly as Fig. 6.29 plot a) and b) (due to the large dimension of the beam respect to the electrode) will be kept by the beam for any solenoids field strength. This contributes to the plateau in the emittance trend with respect to the solenoid values seen in Fig. 6.1 after point 1. In order to compare quantitatively the simulations and the measurements, a different approach is needed. The extraction system was implemented up to the emittancemeter in the WARP code. Constant current extraction of 155 mA deuteron and di-deuteron was injected from fixed surface with the correct plasma meniscus radius (taken from AXCEL); the same gas level of the previous WARP simulation (in the previous section) was ensured and the emittancemeter was modeled as a cylinder at the end of simulation. The proper SEY for tungsten was used. The electrode of the source was set as it follows: $V_{ie} = 19.5$ mA, the electron repeller was set at -4.1 kV. The cone aperture was implemented up to the diagnostic chamber, where the beam pipe radius increases rapidly. As for the previous section, in order to gain simulation speed, the Neumann condition was set at the larger radial position and the gas pressure was doubled. The fringe field from the source coils was also included.

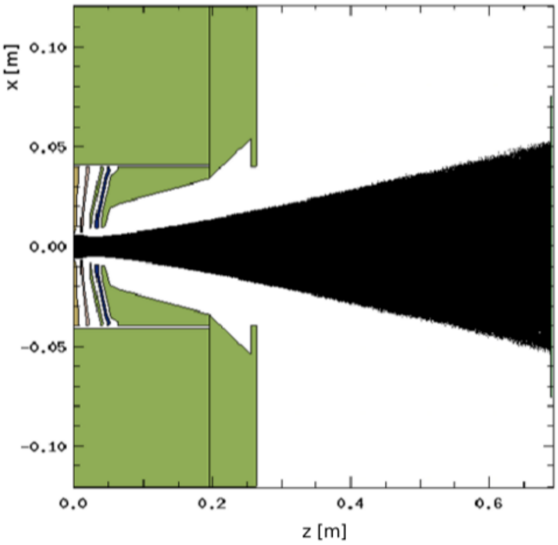

Fig. 6.30 WARP model for phase A3 simulation, xz deuteron beam is shown

It is important to say that these simulation were performed before the A3 phase measurement campaign: the total distance in the simulation is 700 mm; therefore it was necessary to transport the beam phase space with Tracewin from the end of WARP simulation of further 76 mm. This transfer was performed importing the space charge compensation map from WARP up to the final distance (76 mm). The difference between the Tracewin value and

WARP was taken as the error of simulation. Fig. 6.31 present the result of the WARP simulation at the end of 700 mm.

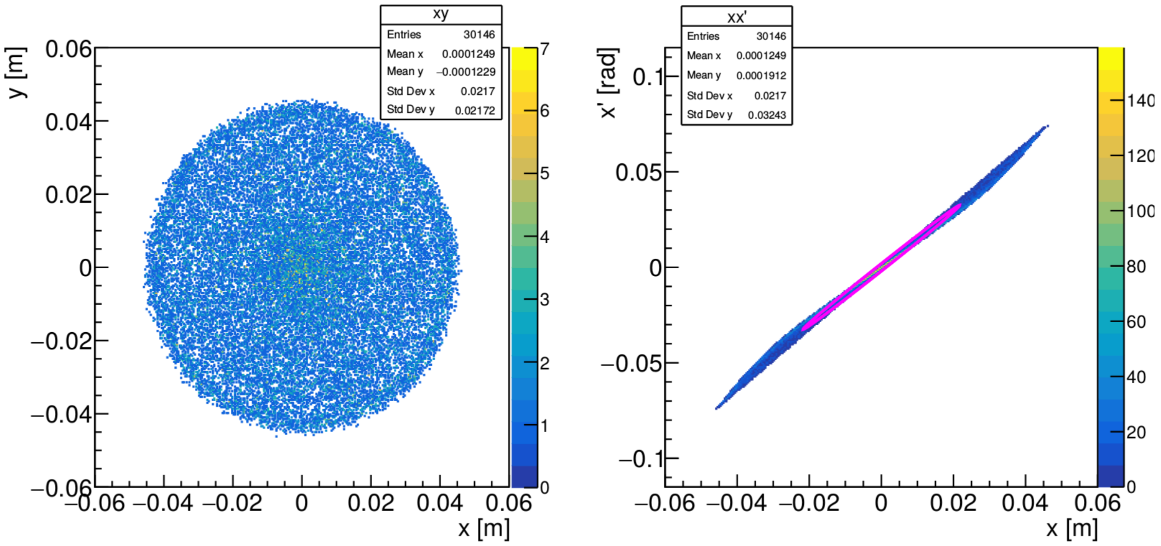

Fig. 6.31 Phase A3 phase spaces for 19.5 kV ΔV_{ie}. The resulted emittance is 0.430 mm mrad normalized rms x

These values were compared with the experimental values obtained for the case of Kr injection. The Table 6.5 below shows the results. Apart from the σ_{beam}, all the other values are in very good agreement. The interesting point of this measurement concerns the large value of the emittance obtained (0.44 mm mrad) compared to what was obtained in phase A2 (see previous section) and expected from AXCEL simulations.

Table 6.5 WARP simulation and measurements

Value	measurement	simulation
σ_{beam}	39.2 ±0.5	22.3 ±4.4
$\varepsilon_{rms,n,x}$	0.44 ±0.03	0.43 ±0.03
α_x	-13.86 ±1.39	-16.31 ±2.00
β_x	14.90 ±1.49	10.93 ±2.61

It is worth to remember that phase A3 system is completely different in terms of boundaries condition to phase A2:

- the beam pipe radius rapidly increases due to the closer diagnostic box.
- there is no solenoid longitudinal field, which creates a not very efficient magnetic bottle with the fringe field of the source coils, but still it has a longitudinal confinement.

- the beam expands without control as well as the electrons are not focused along axis

All the above conditions reflects on the residual self-filed potential (i.e. on the space charge compensation process) which is expected to be substantially larger than the phase A2 case. Fig. 6.32 enforces this explanation: it shows the along on-axis potential of phase A3 and A2. It is possible to see the large bump in the space charge residual potential in the case of phase A3.

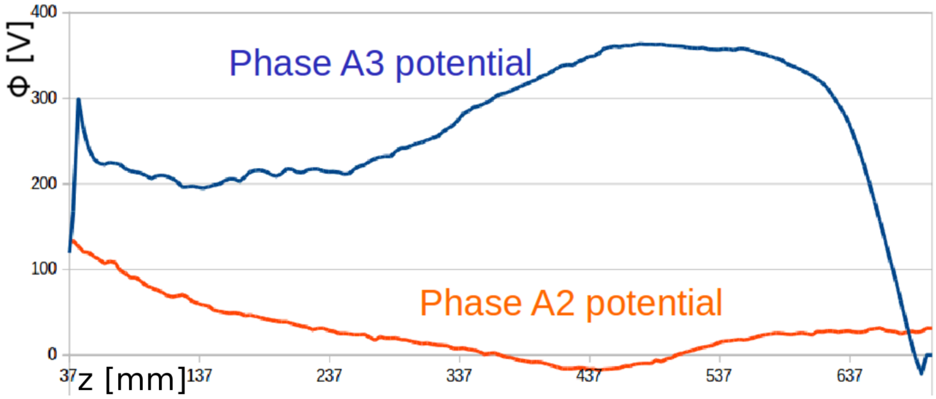

Fig. 6.32 ϕ_{tot} of phase A2 and phase A3 on the first 700 mm

Some words of caution are needed: the space charge bumps depend on the transverse boundary conditions of diagnostic chamber. If metallic boundary condition are used, instead of Neumann, the neutralization degree increases up to completely deplete the space charge potential; in that case the resulted value would have been 0.1 mm mrad rms normalized x (as expected from AXCEL 500 mm before). Thus the sensibility is very high.

The other point refers to the input distribution. As it was explained on the previous section, the input condition for the simulation of phase A2 was a parabolic spatial distribution. While, in this case, the distribution is determined by the extraction system and the source coil magnetic fringe field.

Do to the fact that the s.c.c. depends on the distributions, differences are expected. However in this case, the differences are so huge and the potential along the line behaves so differently that the distribution itself cannot explain all the differences.

6.8 Conclusions and limitation of the model

The self-consistent simulations allow deep insight of the ongoing physics behind the s.c.c. phenomena. The trace-forward and the extraction system model were able to explain a large amount of phenomena seen during the commissioning. The future step will require to unify the two steps in a stand-alone simulation with the extraction system and the LEBT implemented at the same time.

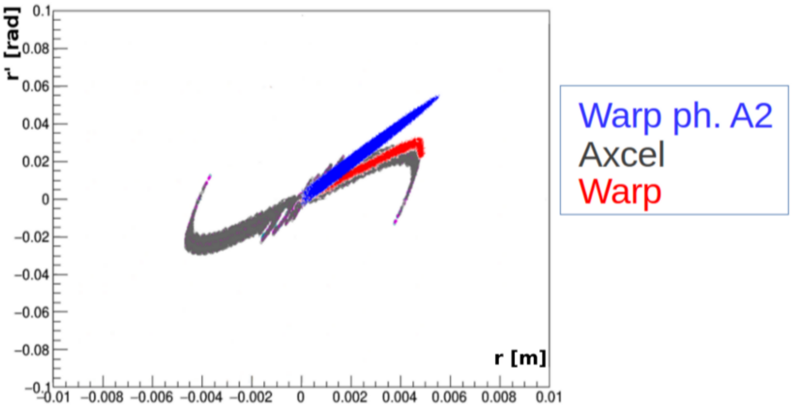

Fig. 6.33 Input distributions obtained with AXCEL, WARP and WARP trace-forward are shown.

As far as the limitation of the model is concerned, the major problem arises for artificial electron heating which cause simulation instabilities. In order to decrease the phenomena, many parameters need to be controlled at the same time, in order to check the steady state behavior. Luckily, the experiment measurements help to identify the errors, but at the price of lower self-consistency degree. Up to now, the only solution to reduce this noise is to increase the number of macroparticles. Again this means that a more powerful machine needs to be used for such kind of simulations.

Chapter 7

Beam dynamics study of the CW RFQ line

7.1 Introduction

The original plan to study the CW steady state of the RFQ foresaw the installation of the SRF cavities and the complete line of the IFMIF/EVEDA facility. However, it is worth to study the possibility to characterize the CW state of RFQ, LEBT, MEBT and HEBT before installing the SRF. The first preliminary study of this solution was presented in an internal report [50] and foresees the substitution of the cryostat with a simple drift see Fig. 7.1.

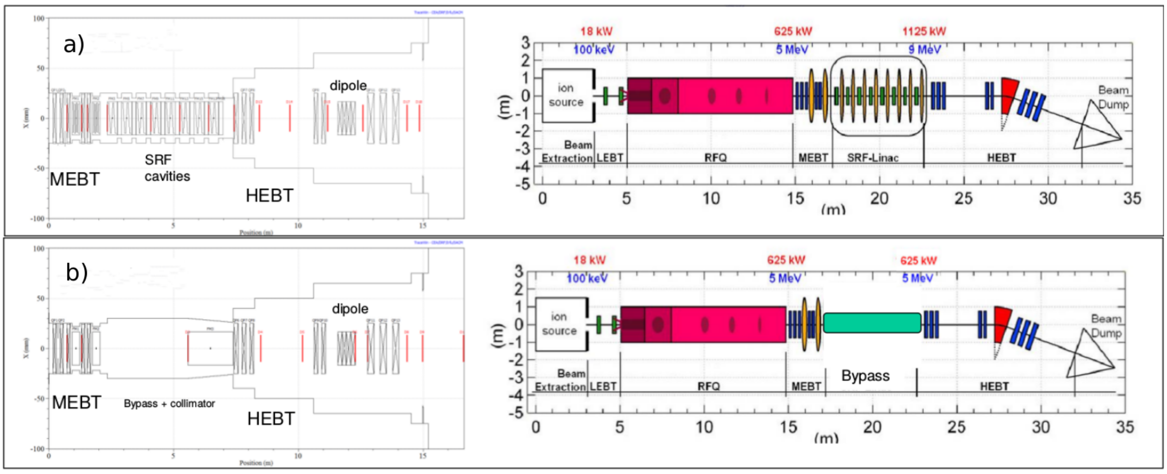

Fig. 7.1 Comparison between the LIPAc with the SRF cavities (a) and with bypass (b). The plots on the left show the Tracewin simulated layout from the RFQ to LPBD, while plots on the right present the sketch of the LIPAc accelerator.

This solution presents spread losses along the accelerators, located in MEBT section and on the first HEBT triplet. For such reason, further studies on different solutions are needed. The result was reported on a technical note [51] which contains several proposals to be analyzed from the beam dynamics point of view. In this chapter the beam dynamics analysis of some of these solutions is presented.

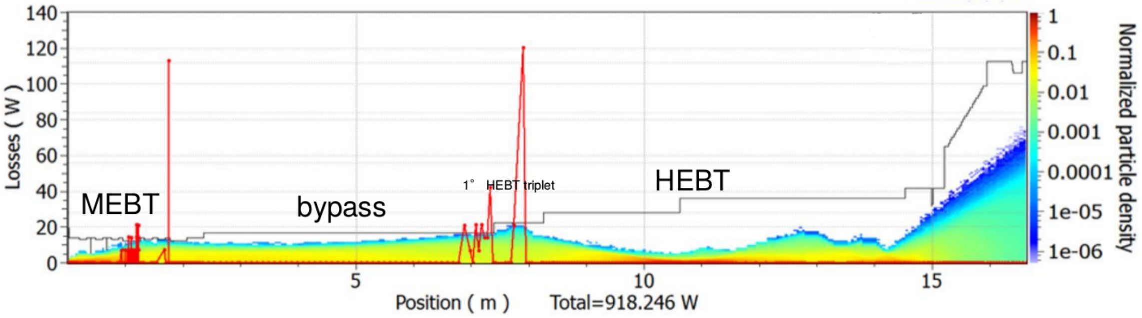

Fig. 7.2 *rz* density plot of the first BD study of the baypass. The losses in W can be seen on the plot as well ass the optic elements position.

7.2 BD studies

The note proposes several ways to bypass the SRF cavities in order to test the CW operation of the RFQ. It was decided to focus on those ones which leave the HPBD and all the MEBT and HEBT quadruples in their position, removing the SRF.

The input beam is taken after the RFQ and consists of 541469 macroparticles, which include the not accelerated particles. The beam represented is 5 MeV D^+, with 125 mA current CW for a total power of 0.625 MW. The input phase space is shown in Fig. 7.3.

The generalized perveance is mainly reduced by the acceleration ($Q = 1.0 \times 10^{-5}$), but the beam is still subjected to halo formations which may induced by particle loss.

Moreover, compared to the nominal line design (with the SRF cavities), this perveance is maintained all along the transfer line and it will not be reduced by further acceleration (a factor 2.3 more than nominal HEBT beam).

As a matter of fact, the entire beam line after the RFQ becomes 16 m MEBT. The last challenge refers to the specific beam that needs to be delivered onto the power beam dump: the requirements are specified in reference [52]. As far as the optics elements is concerned, hard edge models was used. The buncher of the MEBT were switched off.

The not accelerated particles can be seen in the longitudinal phase space: the distribution of not accelerated particles is mainly concentrated at 100 keV, while there are few particles at

4 – 3 MeV. The losses of this last group are not expected at the beginning of the MEBT line, but after the dipole of the HEBT.

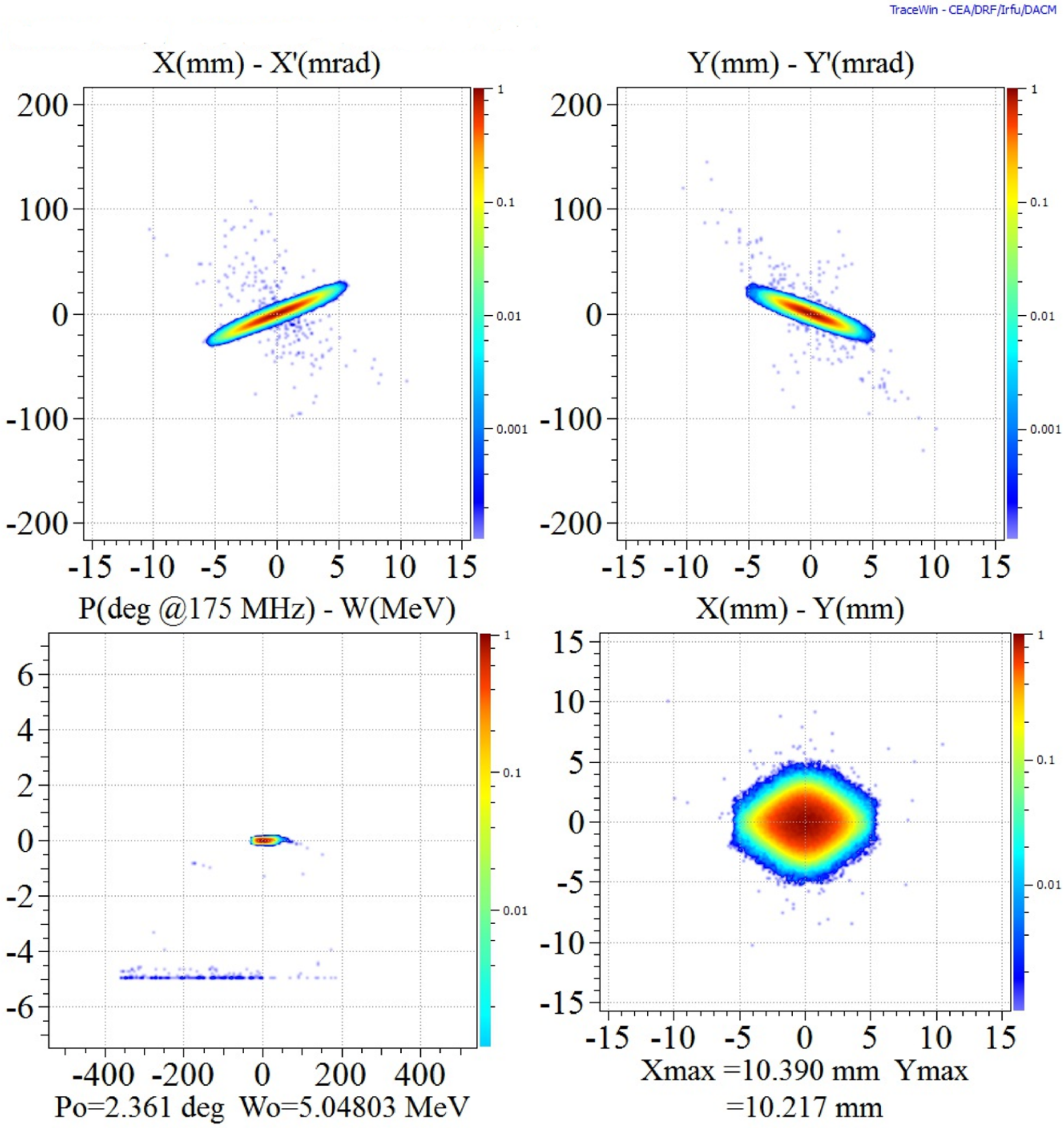

Fig. 7.3 Phase spaces at the output of the RFQ of 125 mA 5 MeV deuterium beam. The upper planes show the transverse phase spaces xx' and yy', while the lower ones present the longitudinal phase space and the spatial phase space.

7.2.1 Cooled drift

The first analysis refers to a drift section in place of the SRF cryostat. On the contrary of the preliminary study (Fig. 7.2) the objective was to constrain all the possible losses on the bypass drift tube and on the predefined scrapers, shown in Fig. 7.4.

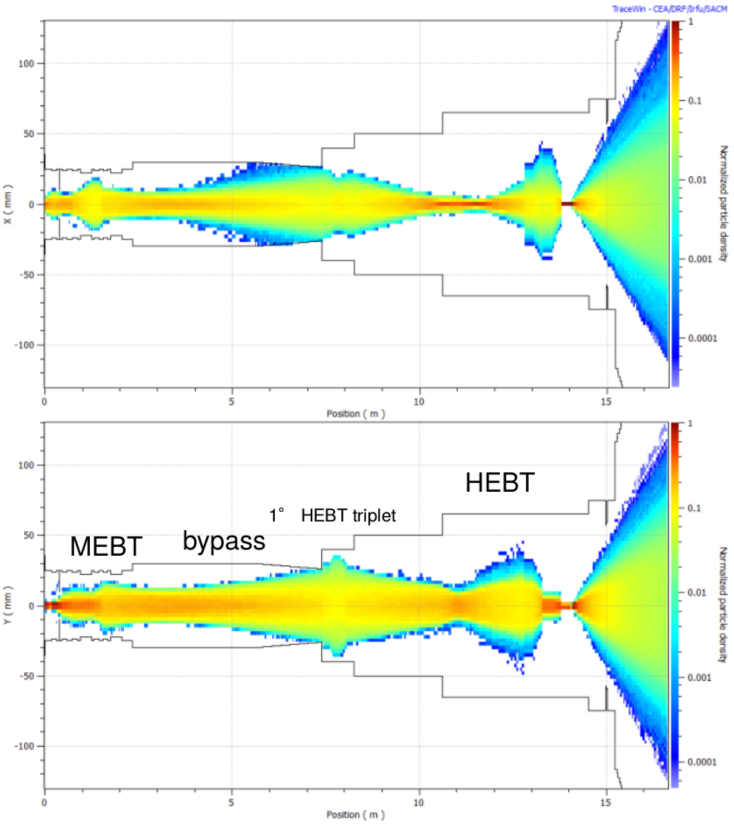

Fig. 7.4 *xz* and *yz* particle density plots of the BD solution with scraper at end thse dirft section.

At the end of the bypass a cone scraper was put in order eliminate the halo formation which is enhanced at the parallel transport in the drift. The losses resulting from the nominal dynamics are of 11.8 kW mainly located on the bypass cone. The loss level is very similar to what the LEBT beam stop and FC needs to sustain. Therefore, the cone needs to be equipped with a cooling system. There are no other losses located on the not-cooled section.

Error study

In order to foresee the possible losses which can occur in such system, a Montecarlo error study was performed. Each quadrupole and dipole are subjected to uniform distributed independent errors on position, angle and gradient, reported in table 7.1.

Table 7.1 Errors applied for the cooled drift study

Error type	Value [±]
RFQ output displacement	±0.1 mm in x, y
Quad. traverse displacement	±0.1 mm in x, y
Quad. tilt x, y, z	0.0573^o
Quad. gradient	0.1%
Dipole traverse displacement	±3 mm in x, y
Dipole tilt in x, y, z	0.6^o
Dipole gradient	0.1%

10000 independent configuration of linac were tested. The results are shown in Fig. 7.5. The maximum beam power loss results 26 kW on the bypass scraper. The drawback of this solution, beside that the scraper needs to be cooled, is that the 1 W/m criteria is not respected. However, this particular configuration is indeed temporarily and the drift tube needs to be removed after the CW test of the RFQ.

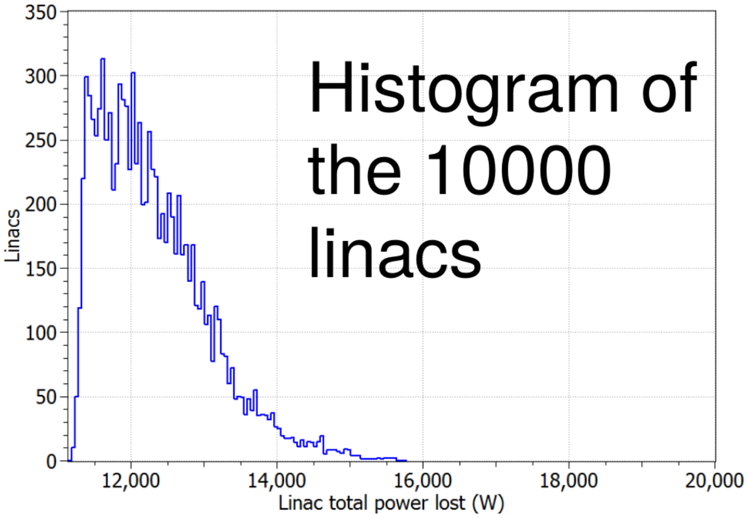

Fig. 7.5 Total power lost occurrence over 10^4 runs

7.2.2 Transfer line

The second solution studied adds two doublets in the bypass section. The main objective is to match the MEBT period to the HEBT focusing period (which is longer respect the MEBT period, due to the higher beam energy expected).
The doublets are based on the ALPI Linac high energy doublets; the characteristics are listed in table 7.2.

Table 7.2 Bypass doublets characteristics

Parameters	Value
Pole radius	50 mm
Space between quad.	150 mm
Quad. length	300 mm
Gradient	10 T/m

The nominal losses of the line are due only to the not accelerated particles. They are located on the initial scraper and after the dipole. The total losses are reduced down to 13 W (which makes it compliant with the 1 W/m criteria). The Fig. 7.6 shows the power deposited along the line. There is no loss of 5 MeV particles.

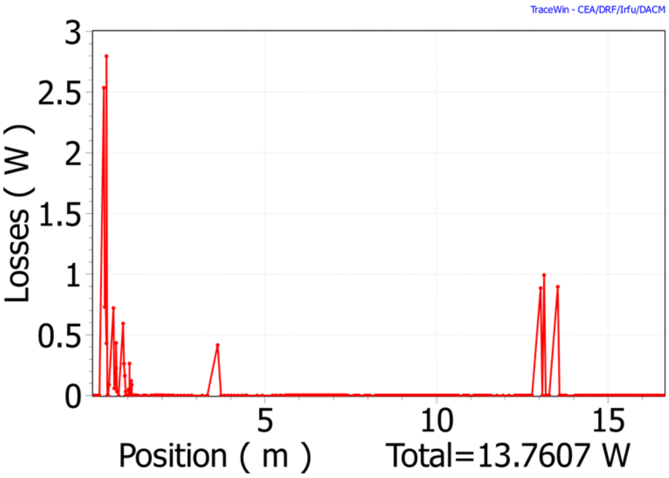

Fig. 7.6 Power lost along the bypass line with doublets.

The envelope model was used in order to perform the required matching and allows to control the dispersion after the first dipole. At the LPBD, the $D_x = 0$.
The macroparticles density plots are shown in Fig. 7.9. The plots show the xz and xy macroparticle densities along the whole line up to the power beam dump. The red line shows the envelope which encloses 99% of particles.
The halo was careful controlled and reduced down to 2 along all the line.

Error study

In order to study the sensibility of the transfer line with respect to the errors such as misalignment and gradient, a similar Montecarlo error study for the cooled drift case was performed.

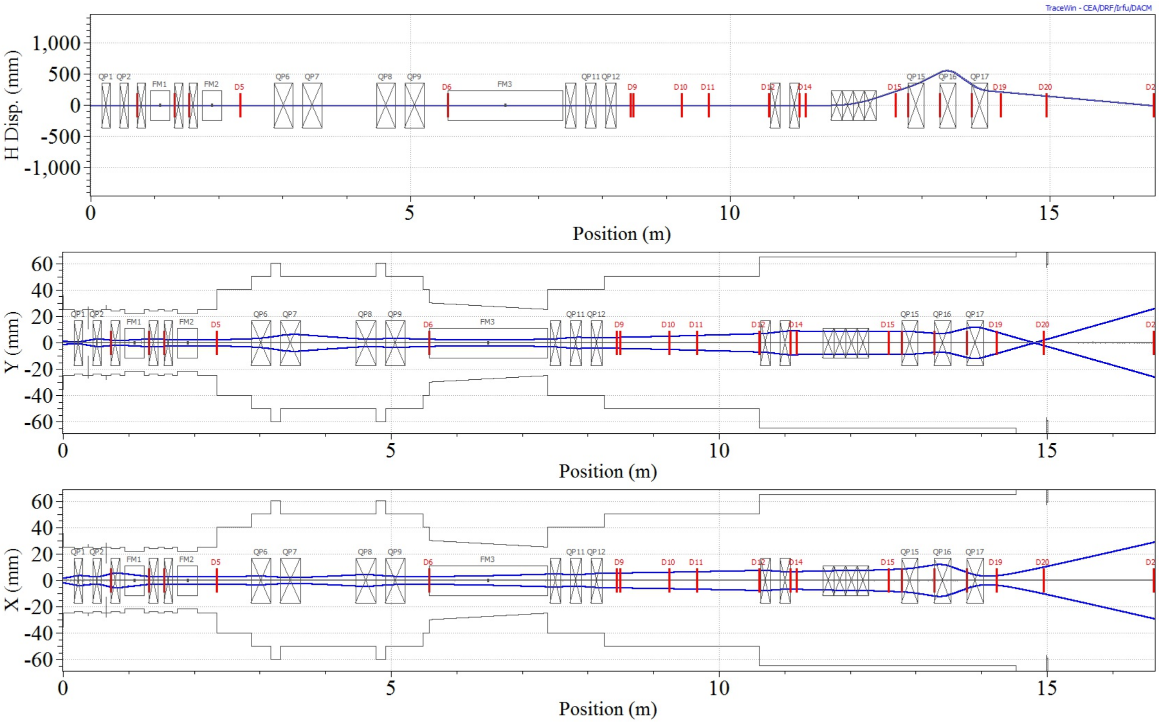

Fig. 7.7 Rms dimensions of the envelope model of the bypass line. The first plot shows the D_x (dispersion function), the other two plots shows the x and y

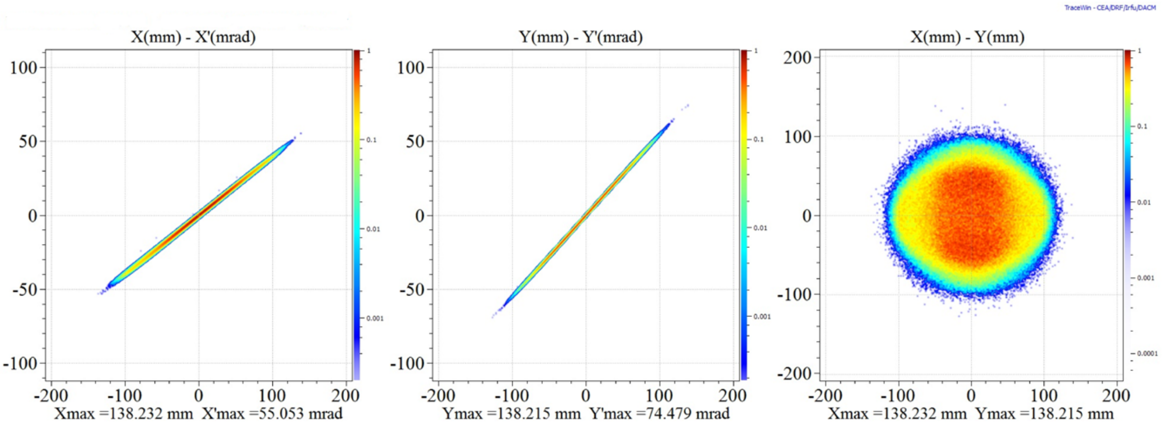

Fig. 7.8 Phase spaces at the power beam dump position. The x and y distributions are not the same due to the different halo generated along the line.

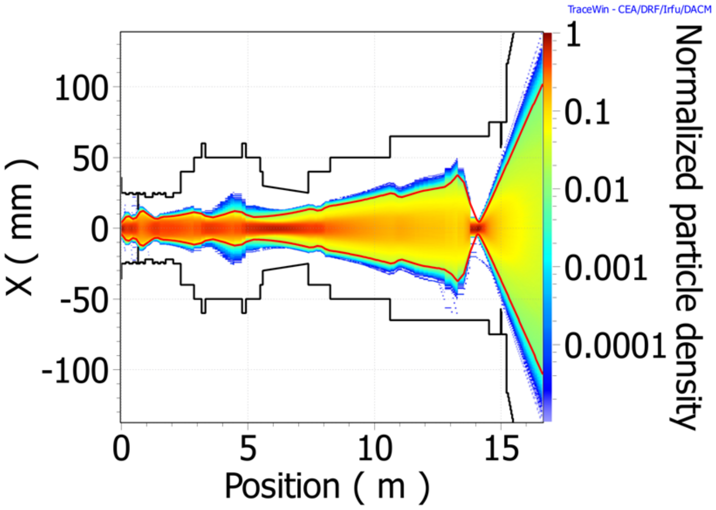

(a)

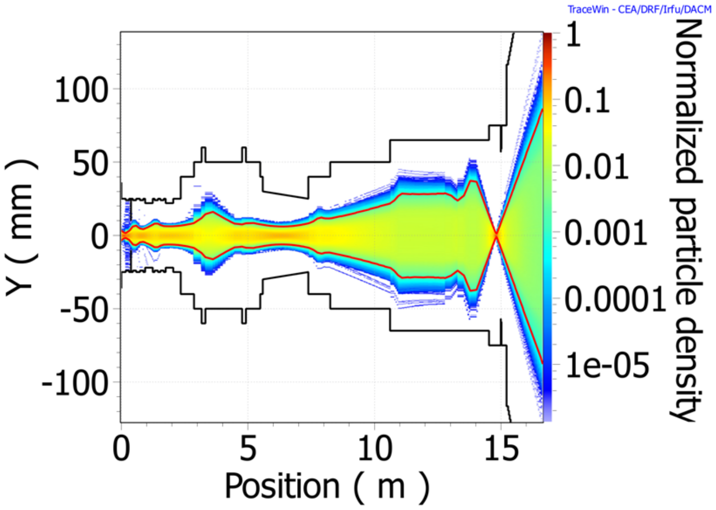

(b)

Fig. 7.9 Density plots of *xz* and *yz* planes. The red line indicates the envelope which encloses the 99% particles.

In this design, the errors specified in reference [53] were applied. Steering procedure was applied in order to reduce the possible losses along the line.

Table 7.3 reports the errors applied to each element, uniformly distributed. At each beam position monitor (BPM) an error was associated, in such a way to introduce the correct level of uncertainty in the steering procedure

Table 7.3 Errors applied on for the transfer line study

Error type	Values
RFQ output displacement	± 0.1 mm in x, y
Quad. traverse displacement	± 0.2 mm in x, y
Quad. tilt (MEBT) x, y, z	0.57^o and 0.17^o in z
Quad. tilt (HEBT) x, y, z	0.9^o and 0.3^o in z
Quad. gradient	0.1%
Dipole traverse displacement	± 1 mm in x, y
Dipole tilt in x, y, z	0.6^o
Dipole gradient	0.1%
BPMs accuracy	± 0.1 mm

In order to distinguish between accelerated (subjected to the 1 W/m criteria) and not accelerated particles, these results were divided with respect the energy spread given by $E_d - E_s$, where E_d is the beam particle energy and E_s is the synchronous particle energy (5 MeV).

The first study considers all the particles in the range [-0.7 MeV+ E_s, 0.7 MeV+E_s], which are tagged as accelerated particles. For such range, no losses were seen over 10^{-4} runs.

The second study considers all the particles in the range [-1 MeV+ E_s, 1 MeV+E_s], thus including the first tail in the longitudinal phase space shown in Fig. 7.3. For such range, only 1 W was lost after the dipole in the subsequent HEBT triplet, in the 99.99% of the cases. The 4 MeV particles are transported up to the dipole: at that position, the dispersion is generated and added to the chromatic effect of the consecutive triplet, causing the losses. This phenomena can be seen in the accumulated densities (i.e. the normalized sum above 10000 cases of all the densities): in the bend plane (x) the symmetry is broken due to the 4 MeV (lower energy particles) which can pass or not after the triplet.

7.3 Conclusions and outlook

Two solutions were studied:

1. Cooled drift: the choice is to concentrate the losses in a specific location of the line (the temporary bypass drift, which will be removed). In such a way, the nominal losses

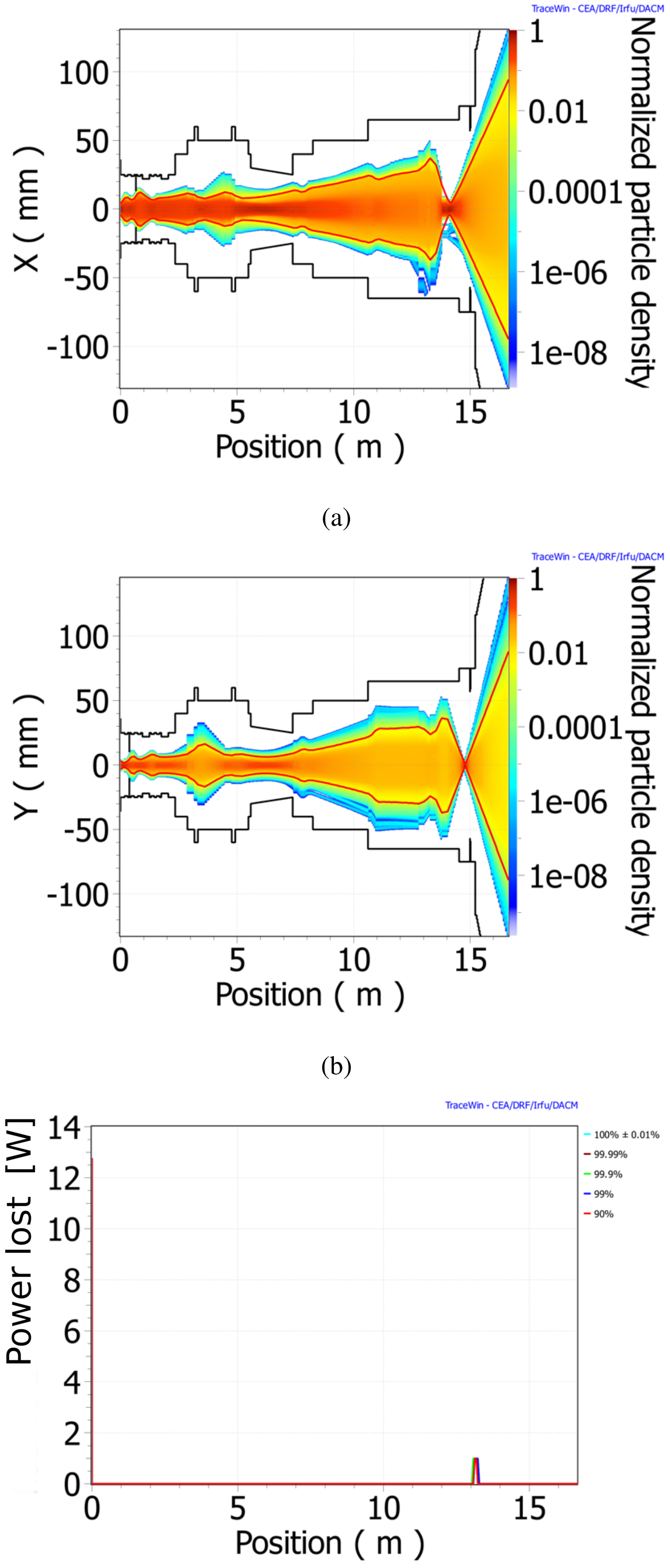

(a)

(b)

(c)

Fig. 7.10 Accumulated density plots of xz, yz planes and power lost occurrence. The initial peak in the power lost is due to the energy limit acceptance set to [-1 MeV+ E_s, 1 MeV+E_s]

are in average with the errors of the order of the 12 kW on the collimator, while for the 90% of the cases is located below 26 kW. A specific cooling circuit needs to be implemented.

2. Transfer line: the total power loss decreases of 3 order of magnitude (i.e. 13 W). This can be easily understood with the better matching between the MEBT and HEBT focusing period. Existing quadrupoles were used for this solution, which were successfully used and tested for the ALPI linac. The solution foresees some space between the quadrupoles, which may be used for additional diagnostic and testing.

As far as the error study is concerned, there is no particle loss for the range [-0.7 MeV+ E_s, 0.7 MeV+E_s]. While in the 99.99% for particles of energy [-1 MeV + E_s, 1 MeV +E_s] the losses are within 1 W/m, located in the last triplet.

Chapter 8

Conclusions

In this thesis several important results and model developments were obtained. The most important are summarized in the following list:

- A scaling law for the extraction system for the proton and contaminant beam (Eq. 3.11) commissioning is proposed and verified via AXCEL-INP simulations (table 6.4). The AXCEL-INP simulation proved to be valuable in describing the extraction behavior in agreement with the simulation.
- A modification of the SCUBEEx method is proposed and integrated in the procedure for the experimental emittance estimation in case of ghost contamination. The procedure was checked with the blind test and double-checked with other methods. This method was then used in order to estimate the results of emittance measurements shown in this thesis.
- The Tracewin software was used to implement the trace-forward method with static neutralization approximation. The trace forward method was modified in such a way to use the experimental data, making it self-consistent.
- The preliminary model, despite its qualitative aim, was in good agreement with LEBT measured transmission with respect to the solenoids (Fig. 5.11). The preliminary model showed the strong dependency of the rms values (emittance and Twiss parameter) and of the transmission with respect to the LEBT solenoids, input beam Twiss and neutralization factors. The beam parameters at the LEBT output resulted to follow specific trends in the solenoids plane: therefore, the commissioning of the injector was organized accordingly, characterizing more carefully the zone of interest for injecting into the RFQ (i.e. upper left quadrant of the solenoid plane), Fig. 5.13 and Fig. 6.1.

- The preliminary model was refined in order to predict the rms quantities of the measurements. The results were in very good agreement with the experimental data (Fig. 5.20 and 5.19) despite all the approximations done. Quite relevant is the agreement between the simulated profile and the experimental data. This model proved also to be a valuable instrument on site for guiding the commissioning in real time. The model suggests the influence of the EMU on the space charge compensation process, via the secondary electron emissions from the tungsten due to proton beam collisions. The model allows also to see complex structures of the beam phase space at RFQ injection. The refined model confirmed the trend of emittance growth and mismatch with respect to the solenoid values found with the preliminary model.

- The model was then used in order to identify the RFQ matching zone (Fig. 5.33) and to test the RFQ behavior with respect to different LEBT settings: a very low dependency of the rms values with respect to the LEBT solenoid values was found (Fig. 5.26) in the matching zone. On the contrary, the transmission may vary more than 30% (Fig. 5.25).

- For the larger perveance of the deuteron beam another software was used in order to predict and explain the measurements. The WARP software was used for such purpose in order to test the trace-forward method in case of dynamic neutralization. Due to the long runs, the procedure was not fully completed, but it allows a preliminary agreement between the simulations and the measurements (Fig. 6.21 and 6.22)

- The effect of the secondary electrons generated from metal was confirmed on the space charge compensation process (Fig. 6.17). Moreover, the model supplies deep insight of the complex trend of the self-field potential at the steady state: the magnetic fields, the changes in the beam pipe aperture and the negatively biased electrodes at the entrance of the LEBT and at the exit of the RFQ were found to redistribute the secondary plasma and change the neutralization trends. When the macroparticle densities at the steady state were studied, the repeller results, from the simulation, to cause an axial non-linear electrons lens which partially modify the deuteron distribution (Fig. 6.12). Despite all the non linear phenomena involved, a preliminary agreement with the rms-emittance measurements was obtained (Fig. 6.22 and 6.21). The model allows also to follow the effect of the space-charge waves on the re-distribution of the particles at the RFQ injection, making possible to follow the transient phenomena in the RFQ behavior. An estimate of the time needed for a steady state operation was made and the beam parameter variations with respect to the transient time were calculated (Fig. 6.9) and (Fig. 6.26)

- The WARP software was also used in order to simulate the extraction column beam dynamics. Excellent agreement was achieved (Fig. 6.5) with the phase A3 measurements, in particular by estimating the emittance growth.

- The AXCEL software was used on site in order to foresee and check the experimental measurement performed during phase A3. A good qualitative trend was found (Fig. 6.28). The results also confirm the correct approach of the formula proposed for scaling the a multi-species beam (Eq. 3.11) which were tested before with simulations; the study of the modifications for a new plasma electrode (performed during the thesis work) which will be used for proton beam extraction, was enforced by the good agreement between the AXCEL simulations and the measurements.

- Two solutions were studied for the modification of the LIPAc line, in order to test the CW operation of the RFQ. The main identified problem belongs to the different focusing periods between MEBT and HEBT which couples with the collective effects of the beam. A solution was design and proposed, in order to overcome these difficulties (Fig. 7.9), implementing two doublets in the bypass drift. The solution stability and response was tested via Monte Carlo method and involves 10000 configurations with realistic errors. There are no loss of the accelerated particles and the overall losses for the nominal solution is 13 W (Fig. 7.6), only due to the not accelerated particles. This proposal was preliminary accepted and it will be submitted to the project management for approval.

References

[1] "ITER website," 2017. ITER website. https://www.iter.org/.

[2] M. R. Gilbert, S. L. Dudarev, D. Nguyen-Manh, S. Zheng, L. W. Packer, and J. C. Sublet, "Neutron-induced dpa, transmutations, gas production, and helium embrittlement of fusion materials," *J. Nucl. Mat.*, vol. 442, pp. S755–S760, 2013.

[3] "IFMIF website," 2017. IFMIF/EVEDA. http://www.ifmif.org.

[4] S. J. Zinkle and A. Moslang, "Evaluation of irrdiation facility options for fusion materials research and developement," *Fusion Engineering and Design*, vol. 88, no. 6-8, pp. 472–482, 2013.

[5] H. Vernon Smith Jr, J. D. Schneider, and R. Sheffield, "Low-energy demostration accelerator (LEDA) test results and plans," in *Proc. of PAC 2001*, pp. 3297–3298, IEEE, 2001.

[6] M. Reiser, *Theory and Design of Charged Particle Beams*. WILEY-VCH.

[7] S. M. Lund, J. J. Barnard, and D. Winklehner, "Beam physics with intense space charge." US Particle Accelerator School 2015. Old Dominion University.

[8] C. K. Allen and T. P. Wangler, "Beam halo definitions based upon moments of the particle distribution," *Phys. Rev. ST Accel. Beams*, vol. 5, p. 124202, 2002.

[9] T. P. Wangler, *RF Linear Accelerators*. WILEY-VCH.

[10] J. D. Callen, *Funfamentals of Plasma Physics*. University of Wisconsin, Madison.

[11] F. J. Sacherer, "RMS envelope equations with space charge," *IEEE Transactions on Nuclear Science*, vol. 18, no. 3, pp. 1105–1107, 1971.

[12] M. E. Rudd, Y.-K. Kim, D. H. Madison, and J. W. Gallagher, "Electron production in proton collisions: Total cross sections," *Reviews of Modern Physics*, vol. 57, pp. 213–218, 1985.

[13] R. A. Baragiola, E. V. Alonso, and A. O. Florio, "Electron emission from clean metal surfaces induced by low-energy light ions," *Phys. Rev. Lett. B*, vol. 19, pp. 121–129, 1979.

[14] "Tracewin website," 2017. CEA. http://irfu.cea.fr/Sacm/logiciels/index3.php.

[15] R. Duperrier, “TOUTATIS: A radio frequency quadrupole code,” *Phys. Rev. ST Accel. Beams*, vol. 3, p. 124201, 2000.

[16] P. Spädke. 99, 65025 Wiesbaden, Germany.

[17] A. Friedman, R. H. Cohen, D. P. Grote, S. M. Lund, W. Sharp, J.-L. Vay, I. Haberand, and R. A. Kishek, “Computational methods in the WARP code framework for kinetic simulations of particle beams and plasmas,” *IEEE Trans. Plasma Sci.*, vol. 42, p. 1321, 2014.

[18] S. M. Lund, J.-L. Vay, R. Lehe, and D. Winklehner, “Self-consistent simulation of beam and plasma systems.” US Particle Accelerator School 2016. Colorado State University.

[19] S. Cousineau, “High power proton facilties: operational experience, challenges and the future,” in *Proc. of IPAC 2015*, pp. 4102–4106, JACOW, 2015.

[20] R. Gobin *et al.*, “Final design of the IFMIF injector at CEA/Saclay,” in *Proc. of IPAC 2013*, pp. 3758–3760, JACOW, 2013.

[21] N. Chauvin *et al.*, “Final design of the IFMIF-EVEDA low energy beam transport line,” in *Proc. of PAC 2009*, pp. 1–3, JACOW, 2009.

[22] A. Pisent *et al.*, “IFMIF-EVEDA RFQ design,” in *Proc. of EPAC 2008*, pp. 3542–3544, JACOW, 2008.

[23] M. Comunian *et al.*, “Beam dynamics redesign of IFMIF-EVEDA RFQ for a larger input beam acceptance,” in *Proc. of IPAC 2011*, pp. 670–672, JACOW, 2011.

[24] I. Podadera *et al.*, “The medium energy beam transport line (MEBT) of IFMIF/EVEDA LIPAc,” in *Proc. of IPAC 2011*, pp. 2628–2630, IPAC’11-EPS-AG, 2011.

[25] H. Dzitko *et al.*, “Design and manufacturing status of the IFMIF-LIPAc SRF Linac,” in *Proc. of IPAC 2015*, pp. 3686–3688, JACOW, 2015.

[26] R. DArcy, M. Alvarez, J. Gaynier, L. Prost, V. Scarpine, and A. Shemyakin, “Characterisation of the PXIE Allison-type emittance scanner,” *Nuclear Instruments and Methods in Physics Research Section A: Accelerators, Spectrometers, Detectors and Associated Equipment*, vol. 815.

[27] B. Bolzon *et al.*, “Intermediate commissioning results of the required 140 ma/100 kev CW D+ ECR injector of LIPAc IFMIF’s prototype.,” in *Proc. of ECRIS 2016*, To be published.

[28] C. Ullmann, A. Adonin, R. Berezov, N. Chauvin, O. Delferrière, J. Fils, R. Hollinger, O. Kester, F. Senée, and O. Tuske, “Investigation of ion beam space charge compensation with a 4-grid analyzer,” *Review of Scientific Instruments*, vol. 87, p. 02B938, 2016.

[29] P. Nghiem, M. Valette, N. Chauvin, and M. Comunian, “LIPAc detailed beam commissioning plan,” technical note, LIPAc EU-HT, 2012.

[30] J. Esposito, “The IFMIF-EVEDA low power beam dump (LPBD) design for LIPAc commissioning tests,” *LNL Annual Report 2014*, 2014.

[31] I. Podadera *et al.*, “A diagnostic plate for the IFMIF-EVEDA accelerator,” in *Proc. of EPAC 2008*, pp. 1248–1250, EPAC’08-EPS-AG, 2008.

[32] M. P. Stockly, “Measuring and analyzing the transverse emittance of charged particle beams,” *Beam Instrumentation Workshop 2006: Twelfth Workshop*, pp. 25–62, 2006.

[33] M. P. Stockli and R. Keller, “Self-consistent, unbiased exclusion methods of emittance analysis,” in *Proc. of PAC 2003*, pp. 527–529, IEEE, 2003.

[34] “ROOT website,” 2017. CERN. https://root.cern.ch/.

[35] B. Bolzon *et al.*, “Beam diagnostics of the LIPACc injector with a focus on the algorithm developed for emittance data analysis of high background including species fraction calculation,” in *Proc. of IBIC 2015*, pp. 313–317, JACOW, 2015.

[36] I. Hofmann and O. Boine-Frankenheim, “Grid dependent noise and entropy growth in anisotropic 3d particle-in-cell simulation of high intensity beams,” *Phys. Rev. ST Accel. Beams*, vol. 17, p. 124201, 2014.

[37] N. Chauvin *et al.*, “Source and injector design for intense light ion beams including space charge neutralisation,” in *Proc. of LINAC 2010*, pp. 740–744, JACOW, 2010.

[38] N. Chauvin, O. Delferriére, R. Duperrier, R. Gobin, P. A. P. Nghiem, and D. Uriot, “Transport of intense ion beams and space charge compenstation issues in low energy beam lines,” *Review of Scientific Instruments*, vol. 83, no. 2, p. 02B320, 2012.

[39] A. Palmieri *et al.*, “Tuning the IFMIF 5 MeV RFQ accelerator,” in *Proc. of LINAC 2016*, pp. 969–971, JACOW, 2016.

[40] E. Fagotti, *Beam Dynamics of the SPES Driver*. Phd thesis, Università degli Studi di Milano, 2005.

[41] M. E. Rudd, R. D. DuBois, L. Toburen, C. Ratcliff, and T. V. Goffe, “Cross section for ionization of gases by 5-4000 kev protons and for electron capture by 5-150 keV protons,” *Phys. Rev. Lett. A*, vol. 28, pp. 3244–3254, 1983.

[42] M. E. Rudd, “User-friendly model for the energy distribution of electrons from proton or electron collisions,” *Nuclear Tracks and Radiation Measurements*, vol. 16, pp. 965–994, 1989.

[43] Y.-K. Kim and M. E. Rudd, “Binary-encounter-dipole model for electron-impact inization,” *Phys. Rev. Lett. A*, vol. 50, pp. 3954–3966, 1994.

[44] P. Stol, M. Furman, J.-L. Vay, A. W. Molvik, and R. H. Cohen, “Numerical simulation of the geneeration of secondary electrons in the High Current Experiment,” *Phys. Rev. ST Accel. Beams*, vol. 6, p. 054701, 2003.

[45] “SRIM website,” 2013. SRIM. http://www.srim.org.

[46] M. A. Furman and M. T. F. Pivi, “Probabilistic model for the simulation of secondary electron emission,” *Phys. Rev. ST Accel. Beams*, vol. 5, p. 124404, 2002.

[47] R. W. Hockney and J. W. Eastwood, *Computer Ssimulation using particles*. Taylor & Francis.

[48] D. Noll *et al.*, "Simulation of space-charge compensation of a low-energy proton beam in a drift section," in *Proc. of HB 2016*, pp. 458–462, JACOW, 2016.

[49] R. Hollinger *et al.*, "High current proton beam investigations at the SILHI-LEBT at CEA/Saclay," in *Proc. of LINAC 2006*, pp. 232–236, JACOW, 2006.

[50] A. Pisent, M. Comunian, A. Facco, P. P. Nighem, A. Mosnier, and S. Ibarra, "Proposal for RFQ commissioning." Mail chat on 10 Jun 2010.

[51] P. Cara *et al.*, "Validation of the RFQ design in steady state," technical note, LIPAc EU-HT, 2017.

[52] F. Arranz *et al.*, "LIPAc HEBT line and beam dump engineering design report," technical note, LIPAc EU-HT, 2012.

[53] N. Chauvin *et al.*, "Start-to-end beam dynamics simulations for the prototype accelerator of the IFMIF/EVEDA project," in *Proc. of IPAC 2011*, pp. 655–657, JACOW, 2009.